universität wien

MASTERARBEIT / MASTER'S THESIS

Titel der Masterarbeit / Title of the Master's Thesis

„Analysis of the spatio-temporal development of snow surface wetness in a high alpine area using terrestrial laser scanning reflectivity“

verfasst von / submitted by

Katharina Maria Knöbl

angestrebter akademischer Grad / in partial fulfilment of the requirements for the degree of

Master of Science (MSc)

Wien, 2018 / Vienna 2018

Studienkennzahl lt. Studienblatt / degree programme code as it appears on the student record sheet:	A 066 299
Studienrichtung lt. Studienblatt / degree programme as it appears on the student record sheet:	Interdisziplinäres Masterstudium Environmental Sciences
Betreut von / Supervisor:	Dr. Martin Mergili

Acknowledgements

I would like to thank alpS for initiating the project, and I am very grateful to the support of Dipl. Geog. Paul Schattan and Dr. Christine Fey who introduced me to terrestrial laser scanning, were part of all the field campaigns and generously supportive whenever needed. I also want to thank Dr. Martin Mergili for his very motivating and constructive feedback and the University of Vienna for their financial support (instrument insurance and dozens of train rides between Innsbruck and Vienna).

I greatly appreciate the opportunity provided by Matthias Huttenlau for letting me be part of the HoPI research group at alpS. Furthermore, I want to thank TIWAG and University of Vienna for providing the TLS; BFW for providing the Denoth meter; Volker Wichmann and LASERDATA for the LIS PRO 3D tools; Klaus Schneeberger, Elena Stoll and Anna Tilg for their support in the field.

Last, but not least, I want to thank my parents, friends and classmates for their unconditional motivation, trust and believe!

Thank you, I learned so much!

Abstract

As the snow packs in mountainous regions are subject to constant change the accurate assessment of snow properties is important, but challenging. One indicator that provides information about the state of snow melting is the liquid water content (LWC). Even though LWC is an important indicator for wet snow metamorphism and snow pack stability, it remains a challenge to measure LWC over large areas with current methods. The major aim of this study is to build a basis for more efficient and accurate snow wetness analysis using terrestrial laser scanning (TLS) reflectivity.

For this purpose the TLS snow surface reflectivity was explored and compared to conventional measurements with a dielectric device (Denoth meter). TLS is an active remote sensing technology capable of providing accurate, high spatial resolution data even in mountainous terrain and on snow surfaces. The reflected laser signal provides information of the surface geometry and reflectivity properties. The combination of 3D locational data with TLS snow reflectivity on a hyper-temporal scale provides a tool for non-destructive LWC measurement and change detection on avalanche prone slopes and over large areas.

Fieldwork consisted of concurrent TLS acquisitions (RIEGL VZ-4000 operating at a wavelength of λ 1550 nm and VZ-6000 operating at NIR λ 1064 nm) and in situ snow sampling at ten locations along an east west transect at Lake Weisssee within the Kaunertal Glacier Ski Resort, Austria (2500 m a.s.l.). The Denoth meter was used for LWC measurements. It was scanned at least two times a day and the field campaigns were coordinated with Sentinel-1A/B satellite overflights.

It was found that TLS reflectivity data could be used to map wet snow areas based on the different spectral reflectance. Wet snow has a lower TLS reflectivity at NIR wavelengths than dry snow. In situ LWC samples measured with the Denoth meter correlate well with TLS reflectivity. Reflectivity at the snow surface decreases diurnally and seasonally from March to May because of increasing LWC. Furthermore, results show that the TLS operating at λ 1550 nm is capable to record moderately wet snow surfaces. Thus, this TLS provides a wide range of application options to practitioners for avalanche defence and hydrological purposes because its operating wavelength is eye safe. The findings are of significance for snow hydrological applications to monitor alpine water resources, avalanche terrain, melt water run-off for flood forecasting, to validate snowpack dynamics of hydrological models and for hydropower management.

Zusammenfassung

Die Schneedecken in den Gebirgen verändern sich kontinuierlich, was es besonders schwierig macht ihren genauen Zustand und ihr Zusammensetzung zu bestimmen. Ein Indikator zur Bestimmung des Schmelzzustandes von Schnee ist der liquid water content (LWC). Obwohl der LWC ein wichtiger Indikator für die Nassschneemetamorphose und die Stabilität der Schneedecke ist, ist es mit den aktuellen Methoden nach wie vor eine Herausforderung, den LWC über große Flächen zu bestimmen. Ziel dieser Studie ist es, eine effizientere und genauere Schnee-Nässe-Analyse unter Verwendung des Terrestrischen Laserscan (TLS) Reflektivitäts Signals zu schaffen.

Zu diesem Zweck wurde die TLS Reflektivität der Schneeoberfläche untersucht und mit konventionellen Messungen mit einem dielektrischen Gerät (Denoth Meter) verglichen. TLS ist eine aktive Fernerkundungstechnologie, die selbst in gebirgigem Gelände und auf Schneeoberflächen genaue Daten mit hoher räumlicher Auflösung liefert. Das reflektierte Lasersignal liefert Informationen über die Oberflächengeometrie und die Reflexionseigenschaften. Die Kombination von 3D-Ortsdaten mit der TLS Reflektivität der Schneeoberfläche auf einer hyper-temporalen Skala bietet eine Methode zur LWC Bestimmung ohne dabei die Schneedecke zu zerstören und sich auf lawinengefährdete Hänge zu begeben. Außerdem können Veränderungen erfasst werden und der Einsatz ist über große Gebiete möglich.

Die Feldforschung bestand aus simultanen TLS-Aufnahmen (RIEGL VZ-4000 bei einer Wellenlänge von λ 1550 nm und VZ-6000 bei NIR λ 1064 nm) und in-situ Schneeproben an zehn Standorten entlang eines Ost-West Transekts am Weißsee im Kaunertaler Gletscherskigebiet in Österreich (2500 m). Das Denoth Messgerät wurde für in situ LWC Messungen verwendet. Es wurde mindestens zweimal am Tag gescannt und die Feldkampagnen wurden mit Sentinel-1A / B Satellitenüberflügen koordiniert.

Ergebnisse zeigten, dass TLS Reflektivität verwendet werden kann, um Nassschneegebiete, basierend auf dem unterschiedlichen spektralen Reflexionsvermögen, zu kartieren. Nasser Schnee hat eine niedrigere TLS Reflektivität bei NIR Wellenlängen, als trockener Schnee. In situ LWC Proben, die mit dem Denoth Messgerät gemessen wurden, und TLS Reflektivität korrelieren gut. Die Reflektivität an der Schneeoberfläche nimmt, aufgrund von zunehmendem LWC, von März bis Mai täglich und saisonal ab. Außerdem zeigen die Ergebnisse, dass der TLS, mit einer Wellenlänge von λ 1550 nm, in der Lage ist, mäßig nasse Schneeoberflächen aufzunehmen. Somit bietet dieser TLS eine breite Palette an Anwendungsmöglichkeiten im angewandten Bereich, wie z.B. für Entschärfungsmaßnahmen auf Lawinenhängen und für hydrologische Zwecke, da seine Wellenlänge augensicher ist.

Die Erkenntnisse sind für schneehydrologische Anwendungen zur Überwachung alpiner Wasserressourcen und des Schmelzwasserabflusses für Hochwasservorhersagen, zur Validierung der Schneedeckendynamik von hydrologischen Modellen und für das Wasserkraftmanagement von Bedeutung.

Table of Contents

Acknowledgements iii
Abstract v
Zusammenfassung vii
Table of Contents ix
List of Figures xi
List of Tables xiv
Abbreviations xv

1 INTRODUCTION 1
1.1 Aim and research objectives 3
1.2 LiDAR technology 4
1.2.1 Laser light 5
1.2.2 Measurement principle 6
1.2.3 Incident angle 7
1.2.4 Laser backscatter 7
1.2.5 Automated signal correction 8
1.3 Recent developments in TLS technology 10
1.3.1 Online waveform processing 10
1.3.2 TLS in five dimensions 11
1.4 Snow properties 13
1.4.1 Forms of snow crystals 14
1.4.2 Snowpack types 15
1.4.3 Wet snow metamorphism 16
1.4.4 Characterization of the snowpack 16
1.4.5 Spectral reflectance of snow 22

2 RESEARCH AREA 25

3 METHODS 29
3.1 Fieldwork 30
3.1.1 In situ snow sampling 31
3.1.2 Terrestrial Laser scanning 35
3.2 Processing of TLS data 39
3.2.1 Geo-referencing and registration 40
3.2.2 Geospatial analysis 42
3.3 LWC and TLS reflectivity 46

4 RESULTS 47

4.1 In situ snow samples 47
4.2 TLS reflectivity 53
4.2.1 Seasonal development of TLS reflectivity 53
4.2.2 Diurnal development of TLS reflectivity 57
4.2.3 TLS reflectivity at differing scanning wavelengths 58
4.3 Liquid water content derived from TLS reflectivity 59
4.3.1 Seasonal development of LWC distribution 59
4.3.2 Diurnal development of LWC distribution 63
5 DISCUSSION 67
5.1 TLS reflectivity and LWC 67
5.2 Scanning wavelength 68
5.3 LWC from in situ snow sampling 69
5.4 Transferability of the method 70
5.5 Limitations 70
5.5.1 Laser beam divergence, range and pulse repetition rate 70
5.5.2 Scanning geometry and incident angle 71
5.5.3 Environmental conditions 72
5.5.4 Registration errors 73
5.5.5 Systematic errors 73
5.5.6 Methodological errors 73
6 CONCLUSION AND OUTLOOK 75
7 REFERENCES 77
8 APPENDIX 87

List of Figures

Fig. 1: Terrestrial laser scanner mounted to a tripod and connected to a battery. On top of the TLS an infrared camera is attached (Personal photograph). 5
Fig. 2: Roundtrip time-of-flight (TOF) measuring principle of a LiDAR instrument (adapted from Prokop, 2008)..... 6
Fig. 3: Online waveform processing and echo digitization of a TLS (after Pfennigbauer et al., 2010). 10
Fig. 4: Five dimensions of LIDAR data: geometric x,y,z coordinates, time (t) dimension and laser return intensity (LRI) in the emitted wavelength (after Eitel et al., 2016)..... 11
Fig. 5: Number of publications with the keywords “LiDAR”, “LiDAR and multi-temporal”, “LiDAR and hyper-temporal”, “LiDAR and intensity”, and “LiDAR and multi-wavelength” searched in the Web of Science database (results of January 2016) (after Eitel et al., 2016). 12
Fig. 6: Common snow crystal forms (after Doesken and Judson, 1997). 14
Fig. 7: Spectral reflectance of snow for varying grain sizes as calculated using the DISORT model (Stamnes et al., 1988). The curves represent the spectra of different snow grain radii ranging from 50 μm to 1000 μm (adapted from Nolin and Dozier, 2000). 23
Fig. 8: Research area Lake Weisssee in the Kaunertal, Austria. Scan Positions 1 and 2 are marked on the Kaunertaler Glacier Road. The area of in situ snow sampling is indicated in blue. Data source: Land Tirol, 2017. 26
Fig. 9: Slope exposition at the research area Lake Weisssee. 27
Fig. 10: Elevation profile from the TLS scan position 1 to the skiing lift in the research area at Lake Weisssee (after Land Tirol, 2017..... 27
Fig. 11: Workflow for snow wetness analysis from in situ snow samples and terrestrial laser scanning (TLS) reflectivity. 29
Fig. 12: In situ snow sampling transect viewed from scan position 1 (Personal photograph). 31
Fig. 13: Snow density measurement with a cylinder (Personal photograph). 32
Fig. 14: Denoth senor inserted into the snow surface layer (Personal photograph). 33
Fig. 15: Terrestrial laser scanner RIEGL VZ-6000 with a thermal camera mounted on top (Personal photograph)..... 35
Fig. 16: Extended Nominal Ocular Hazard Distance (ENOHD) zones for 30, 150 and 300kHz scans with the TLS VZ-6000 (after Land Tirol, 2017)..... 36
Fig. 17: Workflow for registration and geo-referencing in RiSCAN Pro. 39
Fig. 18: Workflow for snow depth extraction in SAGA GIS. 43

Fig. 19: Workflow for the extraction of TLS reflectivity and profiles in SAGA GIS and LIS Pro 3D. 45
Fig. 20: Workflow for the rasterization of exposition and slope in SAGA GIS. 45
Fig. 21: Snow surface with wind rippel on March 13, 2017 (Personal photograph). 50
Fig. 22: In situ measured LWC at the ten target locations along the transect at Lake Weisssee. The samples were taken in the mornings and afternoons of March, April and May 51
Fig. 23: Snow surface grain structure in the afternoon of May 17, 2017 (Personal photograph). 52
Fig. 24: TLS VZ-4000 snow surface reflectivity in the afternoon of March 13, 2017. Scanned from scan position 1 (distance: 150 - 300 m) to the research site Lake Weisssee. 54
Fig. 25: TLS VZ-4000 snow surface reflectivity in the afternoon of April 10, 2017. Scanned from scan position 1 (distance: 150 - 300 m) to the research site Lake Weisssee. 55
Fig. 26: TLS VZ-4000 snow surface reflectivity in the afternoon of May 17, 2017. Scanned from scan position 1 (distance: 150 - 300 m) to the research site Lake Weisssee. 56
Fig. 27: Diurnal development of TLS snow surface reflectivity at the research site Lake Weisssee on April 10, 2017 57
Fig. 28: Comparison of TLS VZ-4000 (right) and TLS VZ-6000 (left) snow surface reflectivity in the morning of May 17, 2017 at Lake Weisssee. 58
Fig. 29: Linear regression of in situ measured LWC and TLS VZ-4000 reflectivity at the research site Lake Weisssee. Blue: topographically corrected reflectivity; red: reflectivity before correction. 59
Fig. 30: Derived LWC distribution in the afternoon of March 13, 2017. Data classified based on the linear regression of in situ LWC and TLS reflectivity and categorized into four classes (dry, moist, wet, very wet) according to the International Classification of Seasonal Snow on the Ground (Fierz et al., 2009). 60
Fig. 31: Derived LWC distribution in the afternoon of April 10, 2017. Data classified based on the linear regression of in situ LWC and TLS reflectivity and categorized into four classes (dry, moist, wet, very wet) according to the International Classification of Seasonal Snow on the Ground (Fierz et al., 2009). 61
Fig. 32: Derived LWC distribution in the afternoon of May 17, 2017. Data classified based on the linear regression of in situ LWC and TLS reflectivity and categorized into four classes (dry, moist, wet, very wet) according to the International Classification of Seasonal Snow on the Ground (Fierz et al., 2009). 62
Fig. 33: Diurnal comparison of the liquid water content (LWC) distribution at the snow surface at the research site Lake Weisssee on March 13, 2017. Data classified based on the

linear regression of in situ LWC and TLS reflectivity. Blue circles indicate the locations of in situ LWC measurements, category 1 (dry) and 2 (moist). 63
Fig. 34: Diurnal comparison of the liquid water content (LWC) distribution at the snow surface at the research site Lake Weisssee on April 10, 2017. Data classified based on the linear regression of in situ LWC and TLS reflectivity. Yellow and red circles indicate the locations of in situ LWC measurements, category 3 (wet) and 4 (very wet). 64
Fig. 35: Diurnal comparison of the liquid water content (LWC) distribution at the snow surface at the research site Lake Weisssee on May 17, 2017. Data classified based on the linear regression of in situ LWC and TLS reflectivity. Yellow and red circles indicate the locations of in situ LWC measurements, category 3 (wet) and 4 (very wet). 65
Fig. 36: Research area Lake Weisssee in the afternoon of May 17, 2017 (Personal photograph). 65
Fig. 37: (a) Vertical error induced by horizontal inaccuracy (after Hodgson and Bresnahan, 2004). (b) 'Time walk' vertical error induced by laser beam divergence over inclined terrain; α = slope angle, γ = laser beam divergence, ΔZmax = maximum elevation error, Δx,y,max = maximum horizontal error (after Baltsavias, 1999). 72

List of Tables

Table 1 Snowpack types on the ground (adapted from National Snow and Ice Data Center, 2018). 15
Table 2: Primary physical characteristics of snow defined by the International Classification for Seasonal Snow on the Ground (according to Fierz et al., 2009). 17
Table 3: Grain shape classification for melt forms of snow according to the International Classification of Seasonal Snow on the Ground (adapted from Fierz et al., 2009). 18
Table 4: Symbols for snow water equivalent measurements (adapted from Fierz et al., 2009). 20
Table 5: Snow categories based on the liquid water content (θ / LWC) after the International Classification of Seasonal Snow on the Ground (adapted from Fierz et al., 2009). 21
Table 6: Field campaigns at Lake Weisssee consisting of TLS acquisitions at scan position (SP) 1 and 2 during Sentinel 1 overflights and in situ snow sampling including LWC, hand test, snow depth and picture documentation. 30
Table 7: Instrument specifications of RIEGL VZ-4000 and 6000 at the laser pulse repetition rates (PRR) of 150 kHz (VZ-4000) and 300 kHz (VZ-6000) as used within this project (adapted from RIEGL, 2017ab). 37
Table 8: Instrument inputs of weather conditions and measurement frequency at the specific scanning campaigns 38
Table 9: Snow wetness categories after the International Classification of Seasonal Snow on the Ground (Fierz et al., 2009). 46
Table 10: In situ snow samples at the transect at Lake Weisssee. 47

Abbreviations

ALS	Airborne Laser Scanning
CCN	Cloud Condensation Nuclei
DEM	Digital Elevation Model
DoD	Digital Elevation Models of Difference
GIS	Geographic Information System
GPS	Geographic Positioning System
ICP	Iterative Closest Point
LiDAR	Light Detection and Ranging
LRI	Laser Return Intensity
LWC	Liquid Water Content
MSA	Multiple Station Adjustment
MTA	Multiple Time Around
PRCS	Project Coordinate System
SAGA	System for Automated Geoscientific Analyses
SD	Snow Depth
SP	Scan Position
TLS	Terrestrial Laser Scanning
SWE	Snow Water Equivalent

1 INTRODUCTION

The Earth is an interconnected and interrelated system with constant energy and element fluxes among and within the different spheres (atmosphere, hydrosphere, lithosphere and ecosphere). The processes forming this very complex system are mainly driven by solar radiation and biogeochemical cycling, and are acting on multiple spatial and temporal scales. For this reason it is very difficult, but important to gain an understanding of our environment and the related processes at various scales.

Especially under changing climatic conditions of mean and high temperatures, an expected increase in heavy precipitation and extreme weather events, combined with shifting seasons, a rising snowline and more rain on snow events (Stoffel et al., 2012) in alpine regions, it is essential to foster research in snow-hydrological topics. Mountain snowpacks are continuously altered through solar radiation, wind, precipitation and human impact. Therefore, frequent, high spatial resolution and accurate assessment of snow properties are necessary to monitor alpine water resources (Schoeber et al., 2014; Schattan et al., 2017), estimate snowmelt volume (Elder et al., 1991), timing of run-off for flood forecasting (Luce et al., 1998, Weber et al., 2010; Prasch et al., 2013); as well as avalanche risk assessment (Brun, et al., 1989; Birkeland et al., 1995) for the planning of defence structures (Margreth and Romang, 2010), validation of numerical snowpack models (Lehning et al., 2006), and disaster risk reduction (Einhorn et al., 2015).

The liquid water content (LWC), which is the amount of water within the snow that is in the liquid phase, is a highly underestimated indicator. It provides crucial insight about the condition and of the snowpack. A high LWC caused by strong solar radiation and/or rain on snow impacts the stability of the snowpack (Kattelmann, 1987; Baggi and Schweizer, 2009; Mitterer et al., 2011). However, up to this day it is still difficult to measure the LWC, even though it is an important indicator for wet-snow avalanche prediction (Mitterer et al., 2013), reservoir management (Koch et al., 2011) and flood forecasting (Weber et al., 2010; Prasch et al., 2013). Methods to measure snow wetness have to be quick and non-destructive to the snow cover because any disturbance can impact its structure and related processes within the snowpack (Denoth et al., 1984).

Current in situ, manual LWC measurements lack the spatial resolution, are inaccurate and not efficient. The hand test, for example, provides only point-scale estimations (Fierz et al., 2009). Some in situ LWC measurement techniques are centrifugal separation, freezing- and alcohol calorimetry, dilution method and dielectric measurements, which have been

described and compared for their equivalence by Boyne and Fisk (1987) and Techel and Pielmeier (2011). The capacitance probes Denoth meter (Denoth, 1989; Denoth et al., 1984) and Finnish Snow Fork (Sihvola and Tiuri, 1986) measure the permittivity of snow. Together with a concurrent density measurement the LWC can be derived. However, in situ methods are destructive, time- and labour intensive, and cannot be applied in inaccessible terrain and on avalanche-prone slopes. As these methods are only single point measurements, in combination with weather station data, they need to be spatially interpolated to study a larger area (Foppa et al., 2007). Though, spatial interpolation methods reduce the data precision and the small-scale spatial variability gets lost.

Lundberg (1997) and Schneebeli et al. (1998) used time-domain reflectometry (TDR) methods to measure snow wetness. Although this technique allows for continuous and non-invasive measurement, it is also not applicable in avalanche terrain. Upward-looking frequency modulated wave (upFMCW) and upward-looking ground-penetrating radar (upGPR) can be applied at avalanche starting zones (Okorn et al., 2014; Schmid et al., 2014). However, they are power intensive, expensive and laborious to install.

As it is difficult to simulate and model snowpack dynamics in the rough terrain of the mountains and in situ field samplings are rare and confined in spatial extent, time consuming, and potentially dangerous; remote sensing technologies are on the rise. Satellite- and airborne remote sensing techniques have been used for the analysis of albedo and snowpacks (Dozier and Painter, 2004; Schaffhauser et al., 2008), mapping of avalanche release and run-out zones (Bühler et al., 2009; Eckerstorfer et al., 2016), wet snow detection (Stiles and Ulaby, 1980; Hallikainen, 1989; Rott and Davis, 1993; Mätzler et al., 1997) and to detect changes in glacier volume and dynamics (Geist et al., 2003; Sailer et al., 2012). However, the rough topography and highly variable weather conditions in alpine regions present drawbacks in the application of air- and spaceborne remote sensing techniques. Contemporary passive microwave systems are very coarse with spatial resolutions of up to 25 km^2 (Koch et al., 2014). Buchroithner (1995) pointed out the challenges of spaceborne remote sensing associated to position displacements, extreme incidence angles, shadows and climatic aspects (cloud cover, aerosols, snow). Furthermore, satellites have long repetition times (a few days) that do not support an analysis of dynamic melt processes.

Within this work a new method to analyse the spatio-temporal development of snow wetness is proposed. LiDAR (Light Detection And Ranging) is a remote sensing technology, capable of providing high spatial resolution data in forested covered areas and in rough terrain (Lefsky et al., 2002). LiDAR has large potential for snow hydrological applications, as it is non-destructive to the snow pack and can be applied without exposition to avalanche terrain. Terrestrial laser scanning (TLS) has been used for snow depth measurements (Prokop et al., 2008; Grünewald et al., 2010; Egli et al., 2011; Deems et al., 2013; Lopez-Moreno et al., 2017).

Furthermore, LiDAR systems are not only recording 3D locational data, but also additional data categories such as reflectivity, which provides important spectral information about the target surface properties (Kaasalainen et al., 2006; Höfle & Pfeifer, 2007; Fritzmann et al., 2011; Prantl et al., 2017). In addition, repeated laser scans assist in change detection and monitoring of snow surface processes.

1.1 Aim and research objectives

This study builds a basis for more efficient snow wetness analysis. For this purpose the potential of hyper temporal TLS reflectivity for the identification of wet snow surfaces is explored and compared to conventional measurements with a dielectric device (Denoth meter). The findings will be of significance for snow hydrological applications to monitor alpine water resources, avalanche terrain, melt water run-off for flood forecasting, hydropower management and to validate snow-hydrological models.

- Can TLS reflectivity data be used to classify snow surfaces? In particular, can TLS reflectivity data be used to identify wet snow areas in a high alpine region?
    1. **Hypothesis: TLS reflectivity data can be used to map wet snow areas based on the different spectral reflectance of water and snow. Wet snow has a lower TLS reflectivity at NIR wavelengths than dry snow.**
- How does the reflectivity of snow surfaces change seasonally from March to May?
    2. **Hypothesis: Reflectivity at the snow surface decreases seasonally from March to May because of increasing LWC.**
- How does the reflectivity of snow surfaces change over the period of a day? What are the influencing factors and how are they spatially differing?

3. **Hypothesis: Reflectivity at the snow surface decreases diurnally because of increasing LWC.**

- How do two TLS of different scanning wavelengths (1064 and 1550 nm) compare in their performance on wet snow?
    4. **Hypothesis: A TLS operating at a wavelength of 1550 nm is capable of operating on snow and wet snow surfaces, but less reliable than a TLS at λ 1064 nm.**
- Can TLS reflectivity be verified by liquid water content (LWC) samples measured with a Denoth meter?
    5. **Hypothesis: In situ point-scale LWC samples measured with a Denoth meter correlate with TLS reflectivity.**
- How do range and incident angle affect the TLS reflectivity data?
    6. **Hypothesis: TLS reflectivity as a tool for LWC mapping is transferable to other alpine research areas because of (RIEGL) instrument automated calibration.**

1.2 LiDAR technology

Recent technological developments in LiDAR instruments have increased their application in the natural sciences due to decreasing costs in data acquisition while generating accurate high resolution topographic data of large areas (Deems et al., 2013; Gabbud et al., 2015; Prantl et al., 2017). LiDAR is an active, highly accurate remote sensing technique which can measure the three-dimensional (3D) position of a surface based on a line-of-sight and time of flight (TOF) measurement (e.g. Höfle and Pfeifer, 2007; Eitel et al., 2013; Deems et al., 2013). In comparison to other remote sensing techniques, LiDAR can operate during both day and night because it is an active system (Gabbud et al., 2015). The technology can be applied as Terrestrial Laser Scanning (TLS) from the ground with the LiDAR instrument mounted on a tripod or as Airborne Laser Scanning (ALS) from the air on an airplane or helicopter. This study will focus on the application of TLS (Fig. 1), and the next section will give an overview of its technology and recent developments.

Fig. 1: Terrestrial laser scanner mounted to a tripod and connected to a battery. On top of the TLS an infrared camera is attached (Personal photograph).

1.2.1 Laser light

A laser (light amplification by stimulated emission of radiation) is a device, which is able to amplify light using only a very narrow band of the electromagnetic spectrum (e.g. near infrared) (Van Genechten, 2008). Theodore Maiman built the first laser at Hughes Research Laboratories in 1960; technology evolved and in the following years it became a widely used instrument in scientific, medical, military, engineering and commercial fields (Van Genechten, 2008). The laser light in a well-defined wavelength is very directional, bright and spatially coherent, which makes it possible to travel as a focused pulse of light over long distances (Vosselman and Maas, 2010).

1.2.2 Measurement principle

RIEGL (2014a) specifies the working mechanism of a TLS instrument as “fast rotating or oscillating mirror inside a slower rotating optical head. The emitted laser pulses get deflected by the rotating mirror and pass through the beam exit window (line scan). At the same time the optical head rotates and moves the rotating mirror (frame scan). This mechanism can cover up to 360°. The angular range of the line scan (vertical movement) is limited by the beam exit window” (RIEGL, 2014a).

The emitted laser pulse propagates through the atmosphere until it hits an object causing backscattered signals to travel back to the instrument, where they are deflected back by the mirror and focused onto the photodetector (Fig. 2; Pfeifer and Briese, 2007; Prokop, 2008; Pfennigbauer et al., 2010; Deems et al., 2013; RIEGL, 2014a). With the roundtrip time-of-flight (TOF), the time from emitted to detected laser pulse the distance (d) to the surface can be calculated as (Eitel et al., 2016)

$$d = \frac{c*t}{2}$$

with *c* being the speed of the laser light and *t* being the time of travel.

The speed and properties of the returned laser signal are influenced by atmospheric conditions such as temperature, atmospheric pressure, sea level, visibility and relative humidity. These parameters have to be measured separately and beforehand because they need to be provided for the instruments automatic corrections.

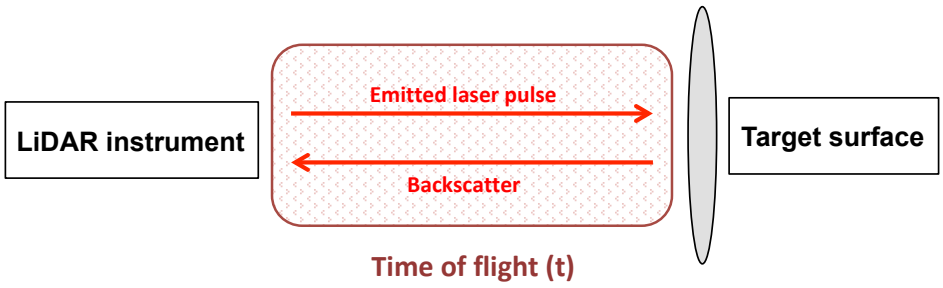

Fig. 2: Roundtrip time-of-flight (TOF) measuring principle of a LiDAR instrument (adapted from Prokop, 2008).

Differential GPS (DGPS) triangulation (for TLS instruments) and an additional inertial measurement unit (IMU) (for ALS instruments) are used to find the absolute position of the LiDAR instrument (Deems et al., 2013; Pfeifer and Briese, 2007). If the absolute position

of the instrument is known, the three-dimensional (3D) locations of the reflecting objects can be determined based on the calculated distances (Rees, 2006). To avoid a loss of data from shading the object of interest is scanned from different positions and angles.

1.2.3 Incident angle

The incident angle is defined as "the angle between the line of sight of the laser beam and the normal vector of the target surface" (Schaer, 2007). Soudarissanane et al. (2007) point out that the quality of the data is highly influenced by the instrument's orientation towards the target. The laser beam hits the surface perpendicular, if the incident angle is 0°; the footprint is a circle, but with increasing incident angles the footprint increases and turns into an ellipse, which can distort the measurements (Prokop 2008).

1.2.4 Laser backscatter

The reflected laser signal or laser backscatter is mainly influenced by the system parameters of the LiDAR, measurement geometry, atmospheric effects and surface characteristics of the object (RIEGL, 2014b; Kaasalainen et al., 2011). "Once the laser light hits an object the signal is reflected to a degree that is related to the physical properties (e.g. colour, type of material, roughness) of the object" and to the incidence angle (Coren & Sterzai, 2006). The backscatter (also referred to as "received optical power (P_r)") can be calculated with the radar range equation (Kashani et al., 2015)

$$P_r = \frac{P_t D_r^2 \eta_{atm} \eta_{sys} \sigma}{4\pi R^4 \beta_t^2}$$

where P_r = received optical power (watts), P_t = transmitted power (watts), D_r = receiver aperture diameter (m), σ = effective target cross section (square meters), η_{atm} = atmospheric transmission factor (dimensionless), η_{sys} = system transmission factor (dimensionless), R = range (m), and β_t = transmit beamwidth (radians).

Effective target cross section (Kashani et al., 2015)

$$\sigma = \frac{4\pi}{\Omega}\rho A_t$$

where ρ = target reflectance at the laser wavelength (dimensionless), Ω = scattering solid angle (steradians), and A_t = target area (m^2).

In addition to locational data, RIEGL TLS are also providing further data categories such as calibrated amplitude, relative reflectance, and pulse deviation for each measured point (Pfenningbauer and Ullrich, 2010). The new TLS instruments operate on near infrared (NIR) wavelengths of 1550 nm (e.g. RIEGL VZ-4000) and 1064 nm (e.g. RIEGL VZ-6000) and are capable of providing good reflectance signals of snow surfaces (RIEGL, 2017b). The reflected signal intensity is greatly depending on the snow surface layer properties such as grain size and form, impurities, water content, age, temperature, etc. Backscatter from a low reflecting target will have lower returned signal intensity compared to that from a high reflecting target. Depending on the target there will either be diffuse reflection (from many angles) or specular reflection (from a single angle) or a mixture of both (RIEGL, 2014a). TLS instruments commonly use Lambertian reflection as diffuse reflection (RIEGL, 2014b).

1.2.5 Automated signal correction

Calibrated amplitude

The calibrated amplitude is one data category of the reflected laser signal and defined as "the ratio of the actual detected optical amplitude (A_{dB}) versus the detection threshold for the entire dynamic range of the instrument (P_{DL})" (RIEGL, 2014b). The dynamic range is the ratio of the largest signal to the detection threshold (Pfenningbauer and Ullrich, 2010).

$$A_{dB} = 10 * log\left(\frac{P_{echo}}{P_{DL}}\right)$$

A_{dB} …Amplitude (decibel), P_{echo} …optical input power, P_{DL} …minimum detectable input power.

According to the RIEGL instrument specification, "the value of the amplitude reading is a ratio, given in the unit of decibel (dB). This measure covers perfectly the wide dynamic range of the RIEGL instrument, usually above 60 dB, i.e. a ratio of more than 1 : 1,000,000. The dB

is a logarithmic unit that indicates the ratio of a physical quantity relative to a specified reference level. A ratio in dB is ten times the logarithm to the base 10 of the ratio of two physical quantities" (RIEGL, 2014b).

However, the calibrated amplitude is range dependent. It decreases with distance according to the laser radar range equation (Jelalian, 1992; Ulaby et al., 1981)

$$\frac{1}{R^2}$$

Relative reflectance

In order to make scan data of different days, scan positions and instruments comparable, RIEGL laser scanner instruments automatically calibrate a relative reflectance attribute. Relative reflectance is defined as "the ratio of the absolute reflectance of a target to the reflectance of the target the instrument was calibrated with (a white reflectance standard with nearly 100% reflectance)" (Pfenningbauer and Ullrich, 2010).

The calibrated relative reflectance results from subtracting the range-dependent amplitude $A_{dB,Ref}^{(R)}$, obtained when measuring to a reflectance standard, from the target's actual amplitude *AdB* (Pfenningbauer and Ullrich, 2010).

$$\rho_{rel} = A_{dB} - A_{dB,Ref}(R)$$

ρ_{rel}… relative reflectance in dB, A_{dB} …calibrated Amplitude, $A_{dB,Ref}{}^{(R)}$ …Amplitude of a reference target at range R.

In addition, "directivity of the reflection is considered and can be interpreted as the normalized laser radar cross section (LRCS) which is defined by three components: the actual area interacting with the laser beam, the reflectance of the target, and the directivity of the reflection. The directivity is quite low for diffusely reflecting targets, but very high for retro-reflecting targets" (RIEGL, 2014a).

1.3 Recent developments in TLS technology

Recently, the application of TLS on snow surfaces has become possible. Furthermore, the instruments are capable of operating over long distances (e.g. up to 6000 m under ideal conditions, RIEGL, 2017b) at data acquisition rates of 222000 measurements/second (RIEGL, 2017b). These long range scanners make it possible to stay out of avalanche-, landslide- and rockfall- prone slopes while covering a large area with high resolution.

1.3.1 Online waveform processing

The high accuracy and reliability of the TLS's is possible through online waveform processing and echo digitization technology, which make scan results available immediately (Fig. 3; Pfenningbauer et al., 2010; RIEGL, 2017b). When the emitted laser pulse hits a target, the optical signal shaped by the laser pulse $P_T(t)$ and the target signature $T(t)$ is returned to the photodetector

$$P_E(t) = P_T(t) * T(t)$$

"there it is transformed into an electrical signal $S_E(t)$ by multiplication with the optical-to-electrical conversion factor k and the impulse response of the receiver $h(t)$" (Pfenningbauer et al., 2010).

$$S_E(t) = k\, P_E(t) * h(t) = k\, (P_T(t) * T(t)) * h(t)$$

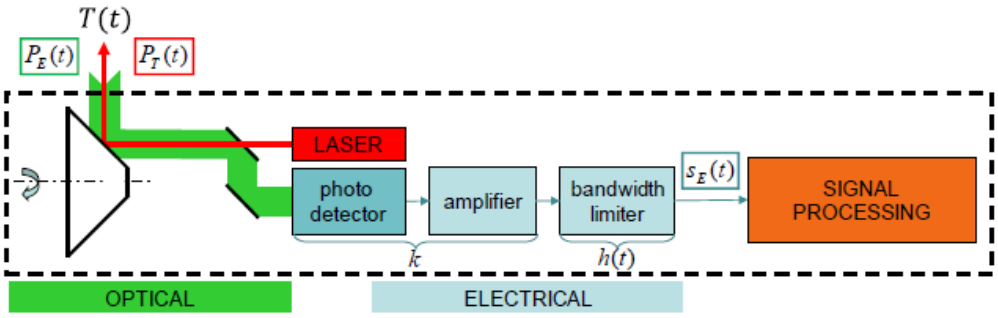

Fig. 3: Online waveform processing and echo digitization of a TLS (figure from Pfennigbauer et al., 2010).

1.3.2 TLS in five dimensions

LiDAR systems are not only recording 3D location (x,y,z coordinates), but also additional data categories such as the automatically calibrated laser return intensity (LRI). “LRI is a measure for the reflectance of an object in the actively emitted wavelength (or multiple-wavelengths) and thus is potentially useful for obtaining spectral information about the biophysical and chemical surface properties” (Eitel et al., 2016). Furthermore, Eitel et al. (2016) point out that an additional time dimension (multi- or hypertemporal) of repeated laser scanning can assist in change detection. Multitemporal scanning refers to more than a monthly or longer return period and hypertemporal means at least several times within a month. “The 3D locational data and time dimensions, combined with the TLS reflectivity at one or more wavelengths (λ) are referred to as the “five dimensions” of LiDAR” (Fig. 4, Eitel et al., 2016). A combined use of these “five dimensions” makes it possible to research and monitor dynamic 3D processes.

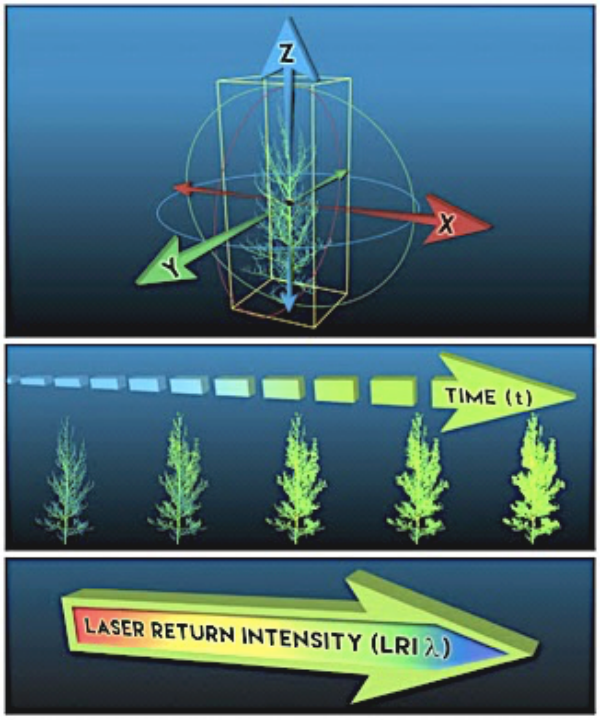

Fig. 4: Five dimensions of LIDAR data: geometric x,y,z coordinates, time (t) dimension and laser return intensity (LRI) in the emitted wavelength (figure from Eitel et al., 2016).

However, a study by Eitel et al. (2016) points out that most of the LiDAR publications to date work entirely with static x,y,z LiDAR data in comparison to using the full potential of LiDAR by incorporating surface reflectivity information and multitemporal or hypertemporal acquisitions and or a combination of those (Fig. 5).

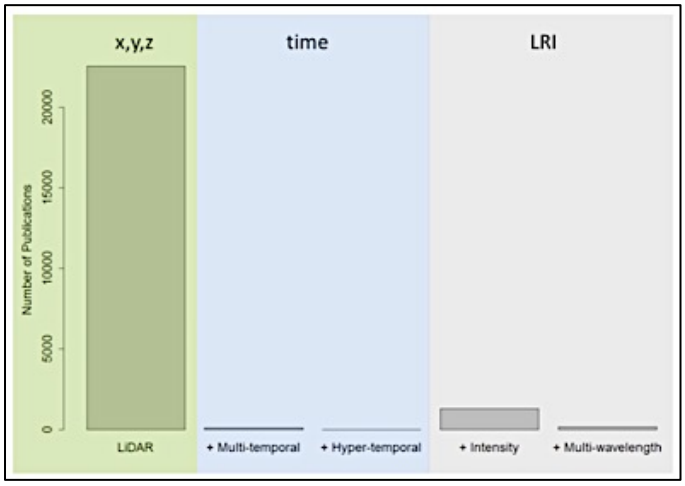

Fig. 5: Number of publications with the keywords "LiDAR", "LiDAR and multi-temporal", "LiDAR and hyper-temporal", "LiDAR and intensity", and "LiDAR and multi-wavelength" searched in the Web of Science database (results of January 2016) (figure from Eitel et al., 2016).

By repeat scanning, changes in spatial patterns can be quantified which are otherwise difficult to model and monitor. Especially the dynamic properties of snow pack metamorphism affected by solar radiation, temperature, exposition, wind, etc. are a field of research where multitemporal and hypertemporal TLS plus the laser reflectivity can provide valuable information about snowpack dynamics and avalanches (Prokop, 2008; Grünewald et al., 2010; Adams et al., 2013, Deems et al., 2015), for the validation of hydrological models (Egli et al., 2012), for the management of hydrologic systems (Painter et al., 2016).

1.4 Snow properties

Snow counts to the most complex materials. "It is a highly porous, sintered material made up of a continuous ice structure and a continuously connected pore space" (Fierz et al, 2009). Snow consists of ice crystals, air, and water at a temperature near 0°C, and it is continuously transforming, referred to as metamorphism (Frolov and Macheret, 1999). Snow is a good insulator due to its porous structure; thus, during melting conditions liquid water can easily percolate (Pomeroy and Brun, 2001). Snow is also highly reflective, especially fresh snow and under cold conditions. Furthermore, it is frequently changing phases, as it is sublimating, evaporating, melting, refreezing (Pomeroy and Brun, 2001).

Doesken and Judson (1997) describe in their detailed work that the formation of snow starts from water vapour high up in the atmosphere. There can only be a certain amount of water vapour depending on the temperature and pressure. The capacity decreases with increasing height until saturation on condensation nuclei (salt particles and droplets of sulphuric and nitric acid) occurs - cloud droplets are formed. As the air cools further these droplets remain liquid and are referred to as supercooled. With continued cooling a state of supersaturation develops and water vapour directly condenses onto cloud condensation nuclei (CCN) such as dust particles forming ice crystals. Also, a transfer of water molecules from the droplets to the crystals evolves because of vapour pressure differences. (Doesken and Judson, 1997)

For snow to form a combination of the three factors is required: (i) air temperature ≤ 0 °C, (ii) sufficient supercooled water droplets and (iii) sufficient suitable aerosols (cloud condensation nuclei, CCN) (Pomeroy and Brun, 2011). Ice crystals grow into multi-crystal flakes as they collide and agglomerate while descending through atmospheric layers of varying temperature and humidity (Doesken and Judson, 1997). Nevertheless, many snow crystals evaporate or melt even before they reach the ground. A snowfall gauge, an open-top cylinder shielded from wind exposure, is generally used to measure snowfall (Pomeroy and Brun, 2001). The accumulation of snow is measured periodically as snow water equivalent (SWE).

1.4.1 Forms of snow crystals

The atmospheric conditions and especially temperature significantly affect the structure of the snowflakes. They can fall as symmetrical, six-sided snowflakes (stellar crystal) or larger clusters of flakes (polycrystals). “A cloud can produce different types of crystals at the same time; however, the most have a hexagonal symmetry because of the molecular arrangement of atoms in the crystal lattice” (Doesken and Judson, 1997). For an overview of common snow crystals refer to Fig. 6.

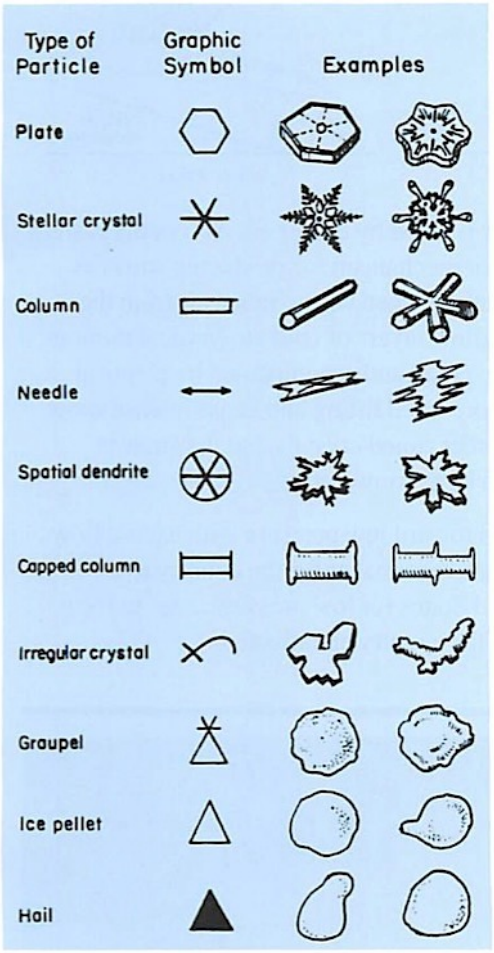

Fig. 6: Common snow crystal forms (figure from Doesken and Judson, 1997).

1.4.2 Snowpack types

As soon as snowflakes hit the ground they are immediately subject to the surrounding conditions of temperature, solar insulation, wind and the snowpack below. Snowpack (or snow cover) includes all the snow and ice on the ground that have not melted (National Snow and Ice Data Center, 2018). Some types of snow are defined in Table 1 (National Snow and Ice Data Center, 2018).

Table 1 Snowpack types on the ground (adapted from National Snow and Ice Data Center, 2018).

Type	Characteristics
New snow	recent snow deposit, original ice crystals can be recognized
Powder snow	dry new snow, loose fresh ice crystals
Névé	young granular snow, partially melted, refrozen and compacted
Firn	rounded well-bonded snow, older than one year, density > 550 kg/m^3
Crust	hard snow surface formed by rain, sun or wind
Cornice	overhanging accumulation of ice and snow
Ripple marks	distinct wind blown patterns
Seasonal snow	lasts for one season
Perennial snow	persists for several years
Old snow	deposited snow, original snow crystals can no longer be recognized

The albedo, “the most significant and commonly measured optical property of snow”, of fresh snow ranges at 0.8 - 0.9 and reflects most solar shortwave radiation, transmits little, and absorbs most longwave radiation (Pomeroy and Brun, 2001; Perovich, 2007). It is therefore an important player in the climate system. Pomeroy and Brun (2001) point out that a fresh snowpack reflects eight times more solar radiation than bare soil. However, the albedo of an aged, dusty and wet snowpack decreases to 0.5. Furthermore, snow is a very light material and often gets redistributed and reworked by wind (Schmidt and Gluns, 1991; Colbeck, 1991). As snowpacks have a low thermal conductivity, they serve as an ideal insulator (Pomeroy and Brun, 2001).

1.4.3 Wet snow metamorphism

As soon as snowflakes hit the ground they are immediately subject to the surrounding conditions of temperature, solar insulation, wind and the snowpack below. Snow metamorphism is defined “as the change in structure and texture of snow grains, which result from variations in temperature, migration of liquid water and water vapour, and pressure within the snow cover” (Doesken and Judson, 1997). While dry snow is characterized by a relative absence of liquid water and has a snow temperature below the melting point (0°C), with the introduction of liquid water through snow melt or rain the faceted crystal structure changes rapidly into a rounded shape and the grains grow up to 0.5 mm (diameter) in a few hours (Colbeck, 1997; Pomeroy and Brun, 2001). Large snow grains bond together to form clusters (Clustered, rounded grains code: MFcl; Raymond and Tunsima; 1979; Fierz et al., 2009). Under natural conditions of diurnally and daily variation in LWC and solar input, grains grow linearly to 1 mm (diameter) within several days (Marsh and Woo, 1987; Pomeroy and Brun, 2001). Wet snow metamorphism also leads to an increase in bulk density up to 350 - 550 kg /m^3 (Colbeck, 1997; Marshall et al. 1999; Jordan et al., 2008).

1.4.4 Characterization of the snowpack

Prevailing snow metamorphism builds a heterogeneous snowpack with distinct layers differing by snow density, grain size, grain shape, LWC, snow hardness, snow temperature, impurities and layer thickness (see Table 2). The following section will define different characterizing parameters of a snowpack (Fierz et al., 2009). A widely used method to classify snow layers is the combination of grain shape and snow density (Fierz et al., 2009).

Table 2: Primary physical characteristics of snow defined by the International Classification for Seasonal Snow on the Ground (according to Fierz et al., 2009).

Characteristics	Units	Symbol
Grain shape		F
Grain size	µm - mm	E
Snow density	kg/m-3	ρs
Snow hardness	depends on instrument	R
Snow water equivalent	kg/m2 or l/m2	SWE
Liquid water content	% vol	LWC or θ
Snow temperature	°C	Ts
Impurities	mass fraction	J
Layer thickness	cm	L

Grain shape

Snow crystals and grains appear in many different forms and shapes. As this study focuses on wet snow, only the melt forms of snow are depicted in Table 3 (Fierz et al., 2009).

Table 3: Grain shape classification for melt forms of snow defined by the International Classification of Seasonal Snow on the Ground (adapted from Fierz et al., 2009).

Class	Shape	Code	Physical process	Important parameters
Clustered rounded grains	Clustered rounded crystals held by large ice-to-ice bonds; water in internal veins	MFcl	Wet snow at relatively low water content (pendular regime), holding free liquid water, clusters form to minimize surface free energy	Meltwater can drain; too much water leads to MFsl
Rounded polycrystals	Individual crystals are frozen into a solid polycrystalline particle , either wet or refrozen	MFpc	Melt-freeze cycles form polycrystals when water in veins freezes; either wet at low water content (pendular regime) or refrozen	Particle size increases with number of melt-freeze cycles; radiation penetration may restore MFcl
Slush	Separated rounded particles completely immersed in water	MFsl	Wet snow at high LWC (funicular regime); poorly bonded, fully rounded single crystals and polycrystals form as ice and water are in thermodynamic equilibrium	Water drainage blocked by capillary barrier, impermeable layer; high energy input
Melt-freeze crust	Crust of recognizable melt-freeze polycrystals	MFcr	Crust of melt-freeze polycrystals from a surface layer of wet snow that refroze after having been wetted by melt or rainfall	Particle size and density increases with melt-freeze cycles

Grain size

The grain size (E) is "the size of a grain or particle at its greatest extension measured in mm. As long as single crystals or grains are recognizable, grain size refers to the single crystals in clusters" (Fierz et al., 2009). The average of all the grain sizes within the snow layer is considered the grain size. Often also the snow grain radius is used to describe grain size. Snow grain radii are very small in fresh and cold snow (50 µm) and increase in size (>1000 µm) with increasing temperature and clustering of wet snow (Painter et al., 2003; Nolin and Dozier, 2000).

Snow density

"Snow density (ρ_s) generally refers to the bulk density, which is the total mass per volume (kg/m^{-3})" (Fierz et al., 2009). Total snow density includes liquid water, ice and air.

Snow hardness

The snow hardness is "the resistance of the snow structure to the penetration of an object" (Fierz et al., 2009). This characteristic is not easily measured since there is no common method or instrument. A widely accepted instrument is the Swiss rammsonde (Fierz et al., 2009).

Snow water equivalent

"Snow water equivalent (SWE) is the amount of water contained within the snowpack and is defined as the depth of water that would result if the mass of snow melted completely; SWE is the product of snow depth (m) and the density (kg/m^3)" (Fierz et al., 2009; Hartzell et al., 2015). It is expressed in mm of water equivalent, which is equivalent to kg/m^2 or l/m^2. Table 4 shows common names of snow water equivalent.

Table 4: Symbols for snow water equivalent measurements (adapted from Fierz et al., 2009).

Description	Symbol
Snow water equivalent	SWE, HSW
Water equivalent from base to height H	HW
Water equivalent of a single layer of thickness L	LW
Water equivalent of snowfall	HNW

Liquid water content

The liquid water content (LWC, θ or free-water content) of snow is defined as "the amount of water within the snow (vol %) that is in the liquid phase" (Fierz et al., 2009). Within this work liquid water content is referred to as LWC or θ. Liquid water is introduced to the snowpack either by rain or melt or a combination of the two processes. Incoming solar shortwave radiation at different slope expositions, aspects as well as elevations drives wet snow metamorphism and melting, which makes the distribution of liquid water very heterogeneous spatially and within the snow pack (Techel and Pielmeier, 2011; Fierz et al., 2009).

The amount of the introduced water is a key factor for its distribution and behaviour within the snowpack (Mitterer et al., 2013). "At low LWC, there are continuous paths of air within the pore space, capillary forces dominate, and water is kept between snow grains (pendular regime)" (Colbeck, 1991). Water is held by capillary forces in grain clusters (Colbeck, 1997) or in ring-shaped bodies surrounding snow grains (Denoth, 2003). At high LWC, water surrounds the snow grains continuously (Colbeck, 1991) and starts to flow due to gravity (funicular regime). Depending on density, this corresponds to a LWC of 3 – 8% (Mitterer et al., 2013). The onset of gravitational flow corresponds to a LWC > 3%vol and liquid water will start to percolate into deeper layers (Mitterer et al., 2013). LWC rarely exceeds 8 vol.% in natural snow (Martinec, 1991; Fierz and Föhn, 1994; Kattelmann and Dozier, 1999). Thus, "in freely draining snow, estimated snowpack wetness would be expected to lie mostly in the dry, moist or wet range" (Table 5; Fierz et al., 2009).

Within this project, a Denoth meter (Denoth, 1989), developed at the University of Innsbruck (Austria) was used for in situ reference measurements to the TLS acquisitions. The dielectric device was used in a study by Fierz and Föhn (1994) to take LWC profiles in the field and to validate snowpack models (Mitterer et al., 2010).

Table 5: Snow categories based on the liquid water content (θ / LWC) after the International Classification of Seasonal Snow on the Ground (adapted from Fierz et al., 2009).

Category	Wetness index	Code	Description	Approximate range of θ_w
dry	1	D	Usually T_s is below 0°C, but dry snow can occur at any temperature up to 0°C. Disaggregated snow grains have little tendency to adhere to each other when pressed together.	0
moist	2	M	T_s = 0°C. The water is not visible even at 10x magnification. When lightly crushed, the snow has a distinct tendency to stick together.	0 – 3
wet	3	W	T_s = 0°C. The water can be recognized at 10x magnification by its meniscus between adjacent snow grains, but water cannot be pressed out by moderately squeezing the snow in the hands (pendular regime).	3 – 8
very wet	4	V	T_s = 0°C. The water can be pressed out by moderately squeezing the snow in the hands, but an appreciable amount of air is confined within the pores (funicular regime).	8 – 15
soaked	5	S	T_s = 0°C. The snow is soaked with water and contains a volume fraction of air from 20 – 40% (funicular regime).	> 15

1.4.5 Spectral reflectance of snow

Reflectivity of snow is very sensitive to LWC and grain size in the NIR and shortwave-infrared wavelengths, but in comparison to the visible wavelengths, it is not affected by impurities (organic soot, dust) (Wiscombe and Warren, 1980; Green et al., 2002). “The rate of grain growth is exponentially proportional to snow temperature; (…) albedo is a function of the grain size” (Jordan, 1991).

Liquid water that enters the snowpack initiates wet snow metamorphism that causes snow grains to stick to each other and to form grain clusters (Colbeck, 1979). Consequently, reflectivity in the NIR decreases when the LWC increases because of the grain clusters. “This is due to the fact that larger grains are both more absorptive and more forward scattering” (Deems et al., 2013; Nolin and Dozier, 2000). Also, when wet snow refreezes, the reflectivity in the NIR remains depressed (O’Brien and Munis 1975).

“Snow grain radii typically range from about 50 μm for fresh, cold snow to 1000 μm (1 mm) for aged, wet snow or grain clusters” (Fig. 7, Nolin and Dozier, 2000). Nolin and Dozier (2000) calculated spectral reflectance for 17 Airborne Visible and NIR Imaging Spectrometer (AVIRIS) channels and snow grain radii (50 - 1000 μm) with the DISTORT model (Stamnes et al., 1988). As the Fig. 7 shows, spectral reflectance is strongest for small grain sizes and at shorter wavelengths. “At 1.0 - 1.3 μm (1000 - 1300 nm) spectral reflectance at the snow surface is most sensitive to grain size” (Nolin et al., 1993; Dozier and Painter, 2004). This figure displays the operating wavelengths of the two TLS instruments used within this project. RIEGL VZ-6000 operates at 1064 nm, which lies within the grain size sensitive spectral range. In comparison, RIEGL VZ-4000 operates at the slightly longer wavelength 1550 nm where spectral reflectance is reduced, but data is less sensitive to grain size.

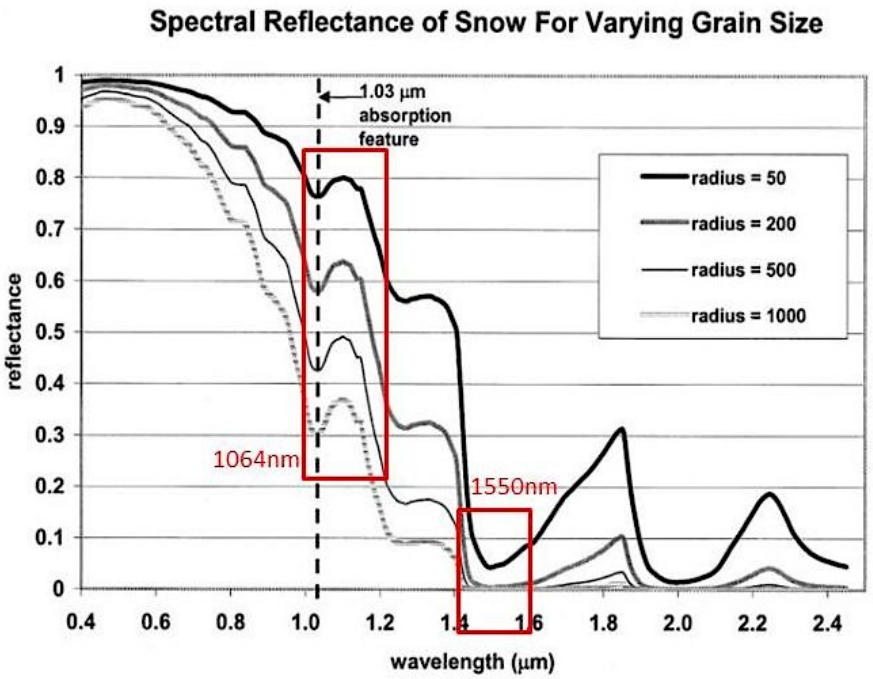

Fig. 7: Spectral reflectance of snow for varying grain sizes as calculated using the DISORT model (Stamnes et al., 1988). The curves represent the spectra of different snow grain radii ranging from 50 μm to 1000 μm (adapted from Nolin and Dozier, 2000).

2 RESEARCH AREA

The study site is located at Lake Weisssee (46.8712874, 10.7124295) (2466 m a.s.l.) in the Kaunertal, a high mountain valley in the Ötztaler Alps of the state Tyrol, Austria. The research area is in close proximity to the Kaunertaler Glacier Skiing Resort at Weissseeferner glacier and is connected to the Kaunertal valley through a road that is kept snow free all year. The Kaunertal is a north south facing valley in the district of Landeck. It runs from the town of Prutz (884 m a.s.l.) to the Weissseespitze (3501 m a.s.l.) at the border to Italy. Lake Weisssee's outflow leads into Krummgampenbach, which flows into the Riffler Bach and connects to the Fagge river, a major tributary of the Inn river. In the upper course of the Kaunertal there is the Gepatsch Reservoir where the upper Fagge catchment drains a highly glacierized area of 51.85 km^2 (Schattan et al., 2017). Yearly mean precipitation in the upper Kaunertal is > 1500 mm/a (IWHW Wien, 2005).

The research area is accessible over the Kaunertaler Glacier Road and located towards the end of the valley at the bottom of Weissseeferner (Fig. 8). The site is confined by the mountain peaks of Großer Nörderberg (2885 m a.s.l.) to the east; Zahn (3376 m a.s.l.) and Weissseespitze (3501 m a.s.l.) to the south-east; Vordere Karlesspitze (3230 m a.s.l.), Hintere Karlesspitze (3160 m a.s.l.) and Wiesjagglskopf (3127 m a.s.l.) to the south-west; Nasse Wand (3049 m a.s.l.) and Hennesiglspitz (3142 m a.s.l.) to the west; Glockturm (3353 m a.s.l.), Habicht (3094 m a.s.l.) and Krummgampenspitzen (3086 m a.s.l.) to the north-west. To the north of Lake Weisssee the middle station of the skiing lift Ochsenalmbahn (2420 m a.s.l.) borders the research site. To the west and south of the lake runs the Kaunertaler glacier road. TLS scan position 1 (SP1, 2523 m a.s.l.) (46.872854, 10.710579) is located on the Kaunertaler Glacier Road facing east into the research area. Scan position 2 (SP2, 2693 m a.s.l.) (46.867004, 10.711617) faces the research area in northern direction from an elevated and more distant position. Distances between the scanner and scanned field sampling site are 150 – 350 m (SP1) and 600 - 700 m (SP2).

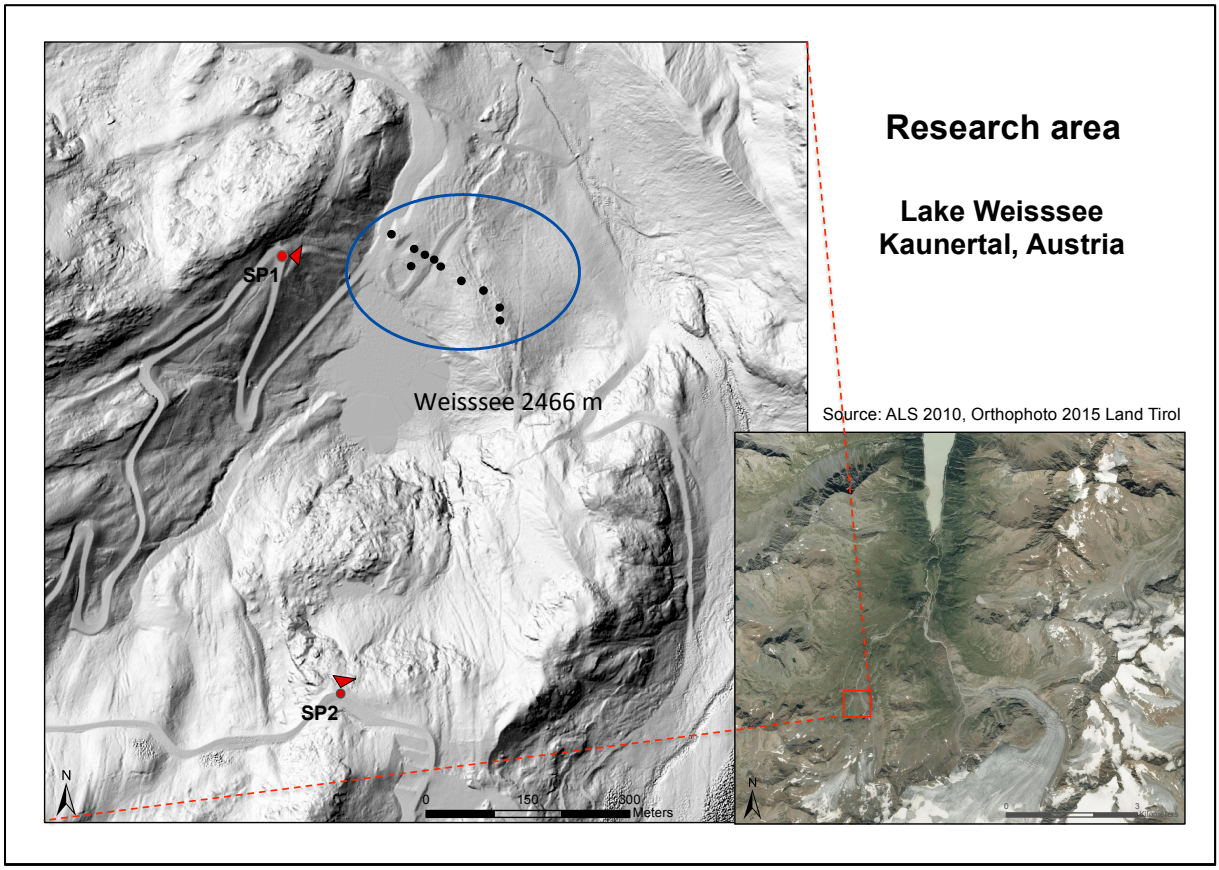

Fig. 8: Research area Lake Weisssee in the Kaunertal, Austria. Scan Positions 1 and 2 are marked on the Kaunertaler Glacier Road. The area of in situ snow sampling is indicated in blue. Data source: Land Tirol, 2017.

The area at the northern shore of Lake Weisssee was chosen as the site for the transect and in situ measurements because of its relatively level topography and proximity to SP1 and an automatic weather station (AWS) operated by TIWAG (Tiroler Wasserkraft AG). The AWS measures precipitation, temperature, wind direction, wind speed and surface energy fluxes. Furthermore, a Snow-Pack-Analyzer (Sommer) is installed to record bulk snow density (Stähli et al., 2004). The elevation ranges between 2420 and 2500 m a.s.l. within a 230 m radius around the AWS and the mean slope is 14.5±10.0° (Schattan et al., 2017). The map in Fig. 9 displays the slope exposition of the surrounding terrain of Lake Weisssee and Fig. 10 displays the elevation profile from SP 1 through the transect towards the skiing lift.

Geologically this area is located in the south western part of the major Austroalpine thrust unit of the polymetamorphic Ötztal–Stubai basement complex (Brandner 1985). The bedrock slopes of the Kaunertal valley are made up of several 100 m thick series of Paleozoic para-gneisses and some intercalations of orthogneisses (Hammer 1923; Purtscheller 1978). The vegetation within the high mountain environment is sparse and limited to ephemeral alpine grass and a dominating surface cover of gravel and rocks from a glacial ground moraine.

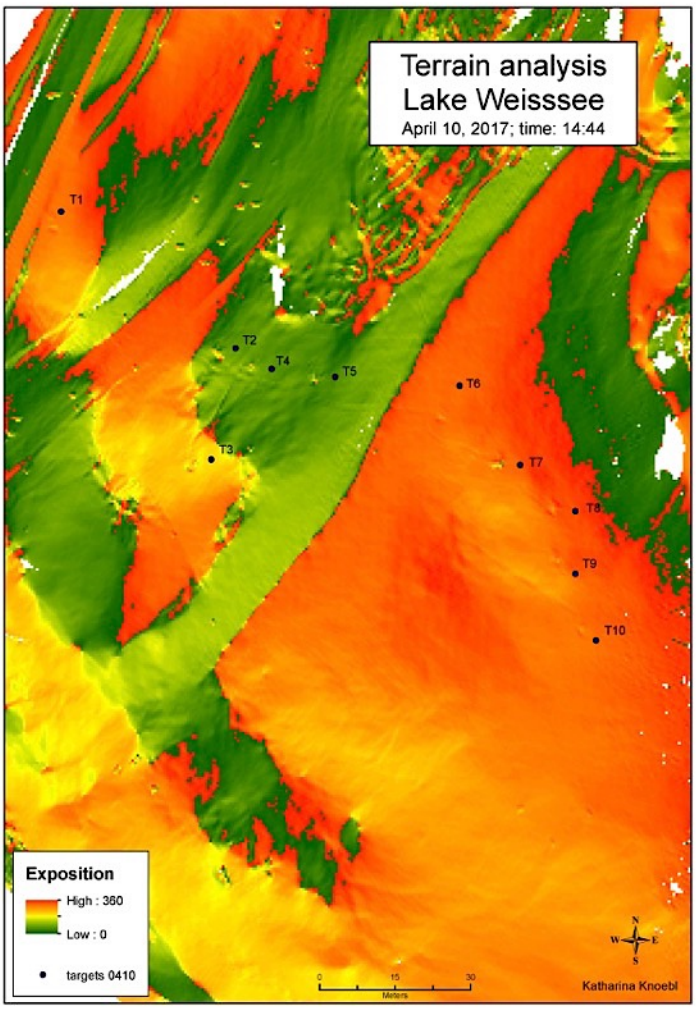

Fig. 9: Slope exposition at the research area Lake Weisssee.

Fig. 10: Elevation profile from the TLS scan position 1 to the skiing lift in the research area at Lake Weisssee (figure from Land Tirol, 2017.

3 METHODS

This section will lead through the several steps of fieldwork planning, data acquisition (in situ snow sampling and TLS), data processing, statistical analysis and mapping of snow wetness. Fig. 11 provides an overview of the workflow for the snow wetness analysis.

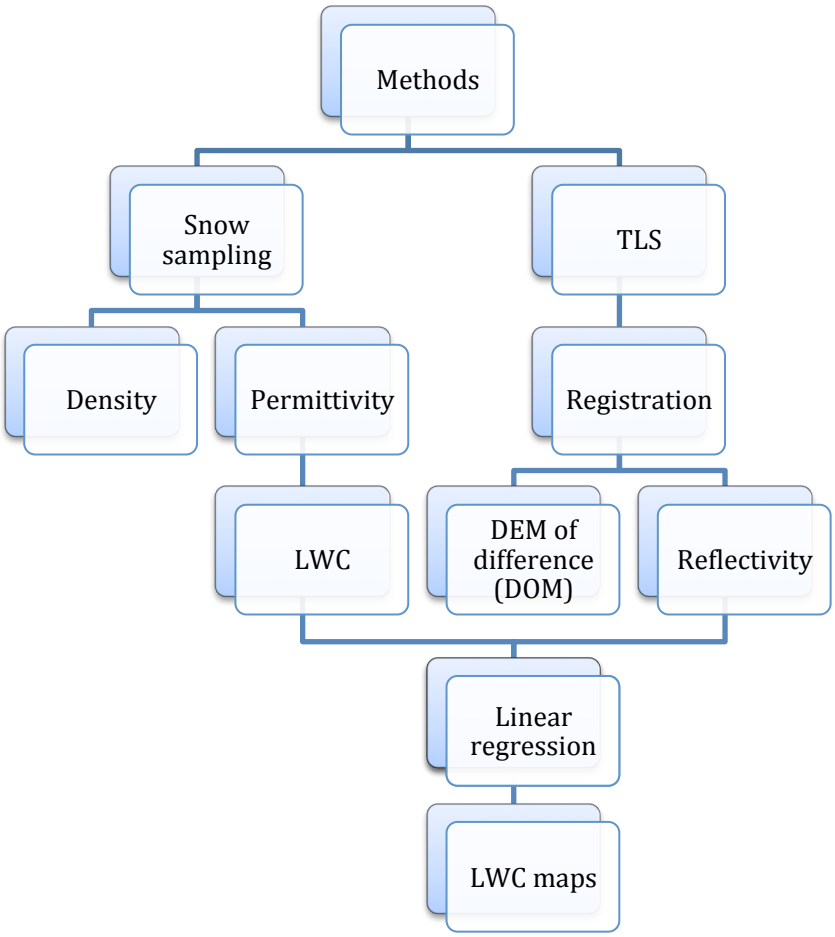

Fig. 11: Workflow for snow wetness analysis from in situ snow samples and terrestrial laser scanning (TLS) reflectivity.

3.1 Fieldwork

The fieldwork consisted of concurrent TLS acquisitions (RIEGL VZ-4000 and VZ-6000) and in situ snow sampling at ten snow pits along an east-west transect at Lake Weisssee. Date and timing of the TLS scans was coordinated with the Sentinel-1A/B satellite overflights in order to make the data comparable to the ENVEO Sentinel-1 wet-snow map product (Nagler et al., 2016). Table 6 displays and sums up the fieldwork conducted within this project.

Planning of the field campaigns needed coordination of (1) weather conditions (no strong winds, no snow fall, no low clouds, constant conditions throughout the day); (2) availability of TLS and TIWAG employee (3) availability of snow sampling equipment and Denoth meter (4) satellite overflight**.** Since the research area is located in a high mountain area where weather conditions can change rapidly, scanning campaigns were planned for days with good predictions. As it was scanned several times throughout the day it needed to be considered to have enough batteries or another electricity source available in the field. Furthermore, there were skiers around during the opening hours of the skiing resort. For this reason scan positions and the location of the snow sampling transect needed to be chosen with consideration.

Table 6: Field campaigns at Lake Weisssee consisting of TLS acquisitions at scan position (SP) 1 and 2 during Sentinel 1 overflights and in situ snow sampling including LWC, hand test, snow depth and picture documentation.

Date	TLS	SP1 (time)	SP2 (time)	Sentinel	LWC	Hand test	Snow depth	Picture
Sep. 13	VZ-4000	09:40-10:10	10:35-10:55	x	x	x	x	✓
Mar. 8	VZ-4000	16:07–37	17:19–29	x	x	x	x	✓
Mar. 13	VZ-4000	14:20–50; 16:58–17:25	13:25–45; 16:26–45	18:04–12	✓	✓	✓	✓
Apr. 10	VZ-4000	11:45-12:15; 14:44-59	10:39–59; 15:48–16:08	07:23–28	✓	✓	✓	✓
May 17	VZ-4000	09:16–46; 14:26–56	12:55–13:25	07:11–23	✓	✓	✓	✓
May 17	VZ-6000	09:50–10:10; 15:13–33	12:10–20; 16:11–31	07:11–23	✓	✓	✓	✓

3.1.1 In situ snow sampling

Fig. 12: In situ snow sampling transect viewed from scan position 1 (Personal photograph).

During each scan in situ point scale snow samples of 1) snow density, 2) snow permittivity, 3) snow depth were taken three times at each snow pit along the transect (Fig. 12). Furthermore, a 4) hand test, 5) pictures and 6) a qualitative description of the snowpack and comments to fieldwork procedures were obtained. The snow pits were marked with targets (for better recognition in the laser scans) and located on different slope expositions. All the snow pit walls were facing south to provide shading conditions for the measurements.

Snow density (ρ) was measured with a cylinder (5 x 6.6 cm), which was inserted vertically into the snow surface layer to obtain a snow sample (Fig. 13). The filled cylinder was weighted with an electronic scale and ρ was calculated from the volume and the weight of the cylinder.

Fig. 13: Snow density measurement with a cylinder (Personal photograph).

Snow permittivity was measured with a Denoth meter developed at the University of Innsbruck, Austria (Denoth, 1989). The Bundesforschungszentrum für Wald (BFW) provided the instrument for this project. The capacitance sensor needs to be fully inserted, about 3 cm below, and parallel to the snow surface of a snowpit wall. LWC can be calculated from concurrent snow density and permittivity measurements (Denoth, 1989).

For the snow depth (sd) measurement a scaled snow stick with 1 cm resolution was pushed vertically into the snowpack until it hit the ground. At each snow pit density and snow depth was measured three times and the values were averaged per snow pit.

Liquid water content was also qualitatively estimated by conducting hand tests according to the International observational guidelines (see Table 5, WSL, 2008; Fierz et al., 2009). This classification is also based upon the description of the different regimes in wet snow, e.g. pendular (grade 3) and funicular (grade 4) (Colbeck, 1973). During this test, a sample of snow is squeezed by hand, and the water content is estimated from the snow structure and visible/nonvisible water (Techel and Pielmeier, 2011). The hand test generally overestimates the volumetric liquid water content.

Furthermore; pictures were taken of the snow surface, the sampling set up and the research area with a common smartphone (IPhone 6), and a qualitative description included comments on the structure and condition of the snow pack and the snow surface, as well as the snow sampling set up and procedure.

Calculations of snow densities, permittivities and LWC after Denoth (1989); Tiuri et al. (1989); Frolov et al. (1999); Mitterer et al. (2011); Koch et al. (2014) and statistical analysis were done within Microsoft Excel 2010.

LWC from Denoth meter measurements

Snow consists of ice, liquid water and air at different compositions and is shaped by prevailing environmental conditions. Since the dielectric function of both ice and liquid water is depending on frequency and temperature (Hasted, 1973; Evans, 1965; Mätzler and Wegmüller, 1987), the dielectric function of snow is also depending on these two parameters. However, Denoth (1982) found that effects of particle size may be neglected in the low- and radio frequency range. Especially in the frequency range from 1 MHz to 10 GHz the dielectric permittivity of melt water (at 0 °C) $\varepsilon = 86$ (Smith and Evans, 1972) is much higher than those of air ($\varepsilon \sim 1$), and ice ($\varepsilon \sim 3.15$) (Frolov and Macharet, 1999; Louge et al., 1998). Thus, the fraction of liquid water in snow can be found based on dielectric permittivity measurements with a Denoth meter (Denoth, 1982).

This device consists of a tuning and display unit, and a 13.5 x 13 cm^2 flat capacitive sensor, which needs to be, inserted about 3 cm below the snow surface (Fig. 14). “90% of the volume the probe is sensing lays within 1.5 cm on both sides of the plate” (Fierz and Föhn, 1994). The grain size characteristics at the snow surface (first 0.5 to 3 cm) are expected to be homogeneous (Nolin and Dozier, 2000). Precise and simultaneous measurements of density ρ and permittivity ε in close proximity yield the LWC.

Fig. 14: Denoth senor inserted into the snow surface layer (Personal photograph).

According to Denoth et al. (1994), snow permittivity (ε) is calculated from the two tuning operations, in air as a reference measurement (U_{ref}, $e^{'} = 1$), and in snow (U):

$$\varepsilon = 1 + k \log(U/U_{ref})$$

where *k* is the sensor-specific calibration factor (*k* = 9.74).

"The reference measurement in air should be made with the sensor unit cooled down to snow temperature (0° C); in the range from -5° to +5°C sensor electronics are not sensitive to changes in ambient temperature" (Denoth, 1994). The accuracy of measurements is ±0.5 vol.% (Sihvola and Tiuri, 1986; Fierz and Föhn, 1994). The measuring range extends from ε = 1 (air) to ε = 6.5 and "the limits for reliable results are set by the validity range of the equation rather than by the measuring range of the instrument, as for θ = 10% by volume and ρ = 650 kg/m^3 results in ε = 4.76" (Fierz and Föhn, 1994). An evaluation of the absolute error can be found in (Fierz and Föhn, 1994).

For water contents up to 10% by volume and densities ρ < 650kg/m^3, the following empirical relation was established (Denoth, 1989):

$$\varepsilon = 1 + 1.92\rho + 0.44\rho^2 + 0.187\theta + 0.0045\theta^2$$

where ρ is expressed in g/cm^3 (or Mg/m^3) and θ (or LWC) in % by volume.

To avoid outliers from measurement error (e.g. air compartments, snow compression) the minimum of the Denoth air reference measurements together with the maxima of three snow measurements per target were used to calculate the permittivity. LWC was calculated from the permittivity combined with the average of three snow density measurements per target.

3.1.2 Terrestrial Laser scanning

Fig. 15: Terrestrial laser scanner RIEGL VZ-6000 with a thermal camera mounted on top (Personal photograph).

In addition to the RIEGL VZ-4000 Terrestrial Laser Scanner operating at NIR λ 1550 nm, the RIEGL VZ-6000 3D Terrestrial Laser Scanner operating at NIR λ 1064nm was used during the field campaign in May 2017 (Fig. 15, RIEGL, 2017b). The shorter wavelength makes this scanner better suitable to record reflections from ice, snow and firn. However, at this wavelength the reflectivity is expected to be less sensitive to changes in LWC. In addition, eye exposure to the direct as well as the reflected laser beam (e.g. glass, binoculars, mirrors,…) is hazardous and since the study area is located within a public skiing resort it can only be used outside the skiing resort's operating hours and a laser pulse repetition rate (PRR) of 300 kHz needed to be used to minimize the extended nominal ocular hazard distance (ENOHD) zone and maintain safety for skiing resort visitors, hunters, rangers, technical personal etc. (Fig. 16; http://www.lasersafetyfacts.com/3B/). For the RIEGL TLS instrument specifications see Table 7.

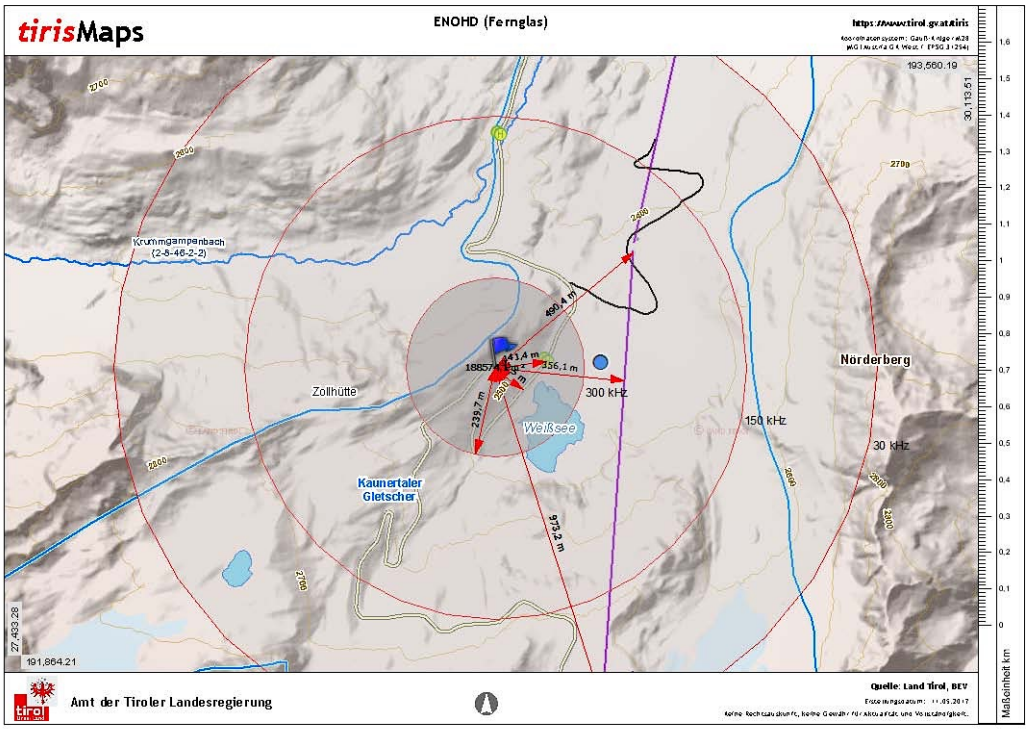

Fig. 16: Extended Nominal Ocular Hazard Distance (ENOHD) zones for 30, 150 and 300kHz scans with the TLS VZ-6000 (figure from Land Tirol, 2017).

Table 7: Instrument specifications of RIEGL VZ-4000 and 6000 at the laser pulse repetition rates (PRR) of 150 kHz (VZ-4000) and 300 kHz (VZ-6000) as used within this project (adapted from RIEGL, 2017ab).

	RIEGL VZ-4000	**RIEGL VZ-6000**
Laser Class	1	3B
Laser wavelength (nm)	1550	1064
Laser Pulse Repetition Rate (kHz)	150	300
Effective measurement rate (meas./sec)	113000	222000
Max. measurement range (ρ≥90 / 20%)	2700 / 1450 m	3300 / 1800 m
Accuracy (mm)	15	15
Precision (mm)	10	10
Min. range (m)	5	5
Laser beam divergence (mrad)	0.15	0.12
Laser beam footprint	18mm@exit; 75mm@500m	15mm@exit; 60mm@500m
Field of view (vertical/horizontal)	60° / 360°	60° / 360°
Scan speed (vertical/horizontal)	100 - 14400 / 0 - 60 °/sec	100 - 14400 / 0 - 60 °/sec
Angular step width (vertical/horizontal)	0.002 - 0.280° / 0.002 - 3°	0.002 - 0.280° / 0.002 - 3°
Angle measurement resolution	better 0.0005°	better 0.0005°
Max. humidity (%)	80	80
Temperature range (°C)	-20 - 50 / 0 - 40 (standard)	-20 - 50 / 0 - 40 (standard)

A snow-off scan was recorded from two scan positions in September 2016 and four snow scan campaigns were launched from March - May 2017. During each campaign two scans a day from two scan positions (except afternoon May 17, VZ-4000, only SP1) were conducted which makes a total of 19 scans within this project (Table 8). In order to record the changing snow characteristics under changing temperature and radiation conditions it was scanned several times throughout the day. The road provided the stable ground needed for mounting the TLS survey tripod to avoid tilting and shifting errors while generating the point cloud. The TLS needed to be adjusted in a way to capture an area including the skiing lift station Ochsenalmbahn at the northern border and the most southern skiing lift pillar at the top of the mountain slope. Also, the glacier road needed to be visible on the scans because those objects are essential for data processing steps of the point cloud. Scan acquisition at SP1 took approximately 30 minutes and the duration at SP2 was approximately 20 minutes.

Table 8: Instrument inputs of weather conditions and measurement frequency at the specific scanning campaigns.

Date; time	Scanner type	Air temperature (°C)	Rel. Humidity (%)	Pressure (mbar)	Weather	PRR (kHz)*
Sep. 13 2016	VZ-4000	11	75	756	clear	150
Mar. 8; 16:07	VZ-4000	-2	60	749	overcast	150
Mar. 13; 14:20	VZ-4000	-3	60	734	clear	150
Mar. 13; 16:58	VZ-4000	-2	60	734	clear	150
Apr. 10; 11:45	VZ-4000	2	60	738	clear	150
Apr. 10; 14:44	VZ-4000	5	55	738	clear	150
May 17; 09:16	VZ-4000	8	55	757	clear	150
May 17; 14:26	VZ-4000	10	55	756	clear	150
May 17; 09:50	VZ-6000	8	55	757	clear	300
May 17; 15:13	VZ-6000	10	55	756	clear	300

- Laser Pulse Repetition Rate (PRR)

3.2 Processing of TLS data

TLS data was geo-referenced and registered with the producer specific software RiSCAN PRO Version 2.5.1 (RIEGL Laser Measurement Systems, Horn, Austria); the open source software SAGA GIS (www.saga-gis.org) and the proprietary extension LIS PRO 3D developed by Laserdata GmbH (Innsbruck, Austria) (www.laserdata.at) were used for geospatial analysis, Esri ArcMap 10.5.1 for visualization and mapping, Microsoft Excel 2010 and Python for statistical analysis and plotting. Fig. 17 provides an overview of the workflow for registration and geo-referencing in RiSCAN (2.5.1).

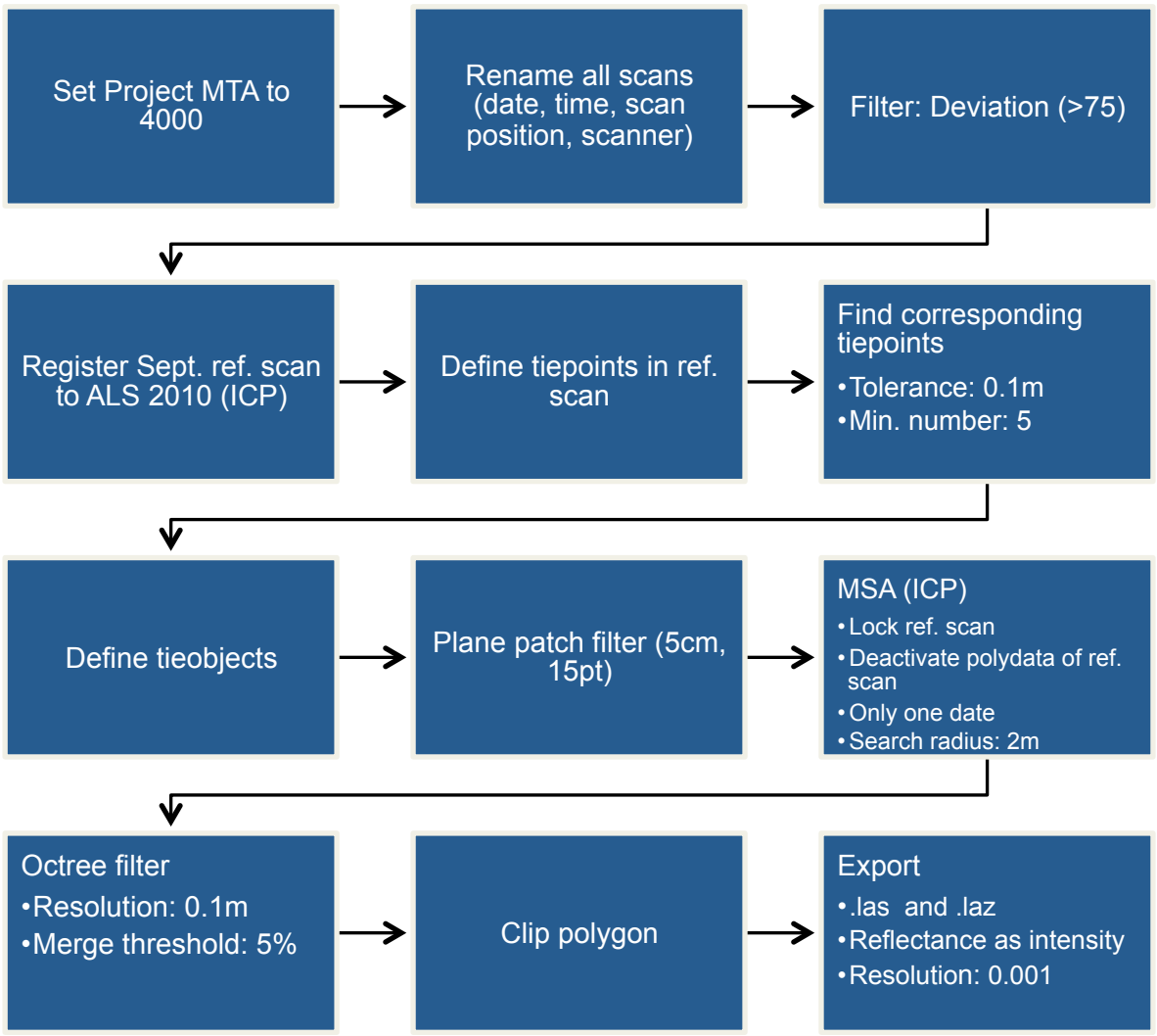

Fig. 17: Workflow for registration and geo-referencing in RiSCAN Pro.

Multiple Time Around (*MTA*), a RiSCAN plugin function to correctly determine the range to a target in TLS instruments with short laser pulse repetition rates (PRR), was set to 4000 m for the whole project. When there are several pulses in the air at the same time the *MTA* plugin determines “the correlation of each received echo pulse to its emitted laser pulse and assigns range zones” (RIEGL, 2015).

In addition to the raw TLS data, the pictures of the inbuilt camera were imported to RiSCAN and merged with the point clouds prior to geo-referencing. In subsequent steps these images get geo-referenced concurrently to the TLS data. The pictures enable to assign true colour to the point cloud. The imported and converted laser echo signals provide ranging, angular, signal amplitude, relative reflectance, pulse shape deviation and RGB information for every point of the point cloud. With these attributes a 3D point cloud can be displayed.

In a pre-processing step the *deviation filter* (>75) was applied to all 19 point clouds and the selected points were deleted.

3.2.1 Geo-referencing and registration

In this study the TLS September 2016 snow-free scan was considered the reference scan for the other snow scans within the project to be matched to. The TLS September 2016 scan was geo-referenced, transformed into a global coordinate system (*GCS*), and registered with an ALS point cloud from 2010 (Fey and Wichmann, 2016) using an *iterative closest points algorithm* (*ICP*, Besl and McKay, 1992; Chen and Medioni, 1992). In this case it was transformed to the national coordinate system Gauss Krüger M28.

In a next step, with the process of point cloud registration the several scans could be matched into the common externally defined project coordinate system (*PRCS*, Prokop et al., 2008; Lichti and Skaloud, 2010; Pfaffenholz, 2012).

Consequently, all the other point clouds were transformed into the global reference frame by matching it with the reference point cloud (Fey and Wichmann, 2016). An *ICP* based registration is not suitable for snow scans because the surface between snow-free and snow scan changes. Registration of the snow scans was performed by searching tiepoints and planes in snow free areas (e.g. ski station walls, pillars, avalanche protections, roads etc.) in the snow-free and snow scan.

Registration via tiepoints

The process of matching the various scans and scan positions in the *PRCS* is based on finding corresponding tiepoints within the snow-free September 2016 reference point cloud (for SP1 and SP2) and the 17 individual point clouds of the snow-covered scans.

First, these tiepoints were defined in the September 2016 reference scans (in the point clouds of both scan positions) as recognizable points at edges and tips on buildings, lift pillars, avalanche protection measures, street signs and other constantly visible spots in the landscape. The tiepoints also needed to be detectible under snow conditions. For SP1 23 tiepoints and for SP2 22 tiepoints were defined in the reference point cloud.

Secondly, the snow-free reference scan (SP1 and 2 separately) and each snow-covered scan individually were arranged horizontally and these tiepoints were exactly searched for and matched manually in the 17 point clouds. The criteria for the tool *Find corresponding tiepoints* was set to a minimum of five matching tiepoints and a tolerance limit of 0.1 m.

Definition of tieobjects

Manual definition of overlapping rectangular surface patches (tieobjects) in the reference and the 17 snow covered scans. The tieobjects were selected on larger snow free areas such as the street, the lift station and the base of the lift pillars. Overall 45 tiepoints were defined for SP 1 and 2 in order to increase registration accuracy.

Iterative closest point algorithm (ICP)

With the *Multi Station Adjustment* (*MSA*) plugin the registration of the point clouds can be further improved. The *MSA* uses an *iterative closest point algorithm* (*ICP*); “by modifying orientation and position of each scan the best overall fit is found” (RIEGL 2014a). The point clouds were prepared with a *plane patch filter*, which produces plane patches with the biggest possible size while fulfilling the conditions of "*Maximum plane error*" and "*Minimum number of points per plane*". For this project the "Maximum plane error" was set to 5 cm and the "*Minimum number of points per plane*" was defined as 15. The *ICP* algorithm uses the tiepoints, tieobjects and polydata objects (reduced point clouds).

While applying the *MSA* the reference scan was locked, its polydata objects were deactivated and only the scans of one campaign at a time were used in order to align a campaign as close as possible to the geo-referenced September scan. A search radius of 2 m was applied in this process.

In a next step, an *octree filter* (resolution: 0.1 m, merge threshold: 5%) was applied and a common polygon enclosing the snow sampling area was clipped from the 19 point clouds to reduce the processing time of further geospatial analysis. Finally, the clipped point clouds were exported as LAS and LAZ files (resolution: 0.001 m). LAS is a binary file format and is the predominant method for transmitting point cloud data (ASPRS, Deems et al., 2013). The current version of the LAS specification is LAS 1.4 (Graham, 2012). LAZ (LASzip) is a compression format based on the LAS specification, and reduce file sizes to 7 - 20% of the original LAS file size (Isenburg, 2013).

3.2.2 Geospatial analysis

The System for Automated Geoscientific Analyses (SAGA) is an open-source Geographic Information System (GIS) software for geodata processing and analysis, and the extension LIS PRO 3D enables laserscan analysis in the 3D point cloud.

In the first step, the software was used to simplify the dense LiDAR point clouds to surface models by rasterizing the 3D point clouds to grids with a resolution of 0.5 x 0.5m. The process of rasterization derives a single *z*-value for each grid (raster) cell that is representative for the surrounding point *z*-values within the grid cell. If the grid interval is smaller than the nominal point spacing of the TLS point cloud, an interpolation method (e.g. inverse distance weighting or kriging) is used to compute the grid cell *z*-value; however, in the TLS point clouds, the point spacing is usually smaller than the grid resolution, and an average of all coordinate *z*-values within each raster cell is used (Hartzell et al., 2015).

Snow depth

In a subsequent step, the gridded digital elevation models (DEM) were used to generate DEMs of difference (DoD) between the 17 snow covered grids and the snow-free September 2016 grid (SP1 and 2). Here the snow-free grid is subtracted from each snow-covered grid to result in grids displaying the areas covered with snow only. This method was applied for each scan date, time and SP separately. The grids were reclassified to account for a 3 cm registration error and vectorized. The resulting snow-covered polygons for each date, time and scan position were used to clip the corresponding z-value grids in order to obtain snow depth grids. Furthermore, the reclassified snow-covered polygons were also used to clip the corresponding point clouds to produce a more precise version of snow-covered elevation point cloud in comparison to the simplified rasterized grid. Fig. 18 displays an overview of the workflow for snow depth extraction.

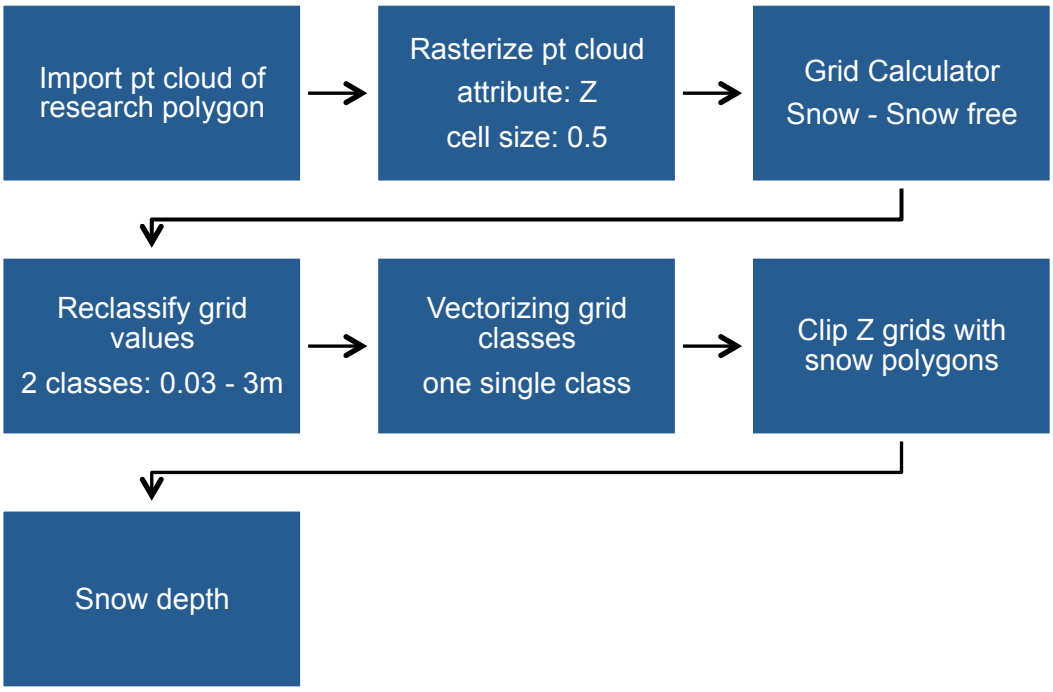

Fig. 18: Workflow for snow depth extraction in SAGA GIS.

Reflectivity

In addition to the scanner's automated range correction (Pfenningbauer and Ullrich, 2010), a topographic correction was implemented. Since the incidence angle of a laser signal hitting an object is varying, it is necessary to topographically correct the reflectivity data in order to make the data comparable over different scan positions and research regions.

Topographic correction of reflectivity

First, range, normal vectors and incidence angles of the point clouds were calculated after Fey and Wichmann (2017).

Secondly, a topographic reflectivity correction after Höfle and Pfeifer (2009) was applied; however, it was overestimating the reflectivity data, possibly due to the fact that this method was established for the correction of raw ALS data. In our case the RIEGL TLS already automatically calibrated the reflectivity for the distance.

In a different method we fitted a linear regression of the mean incidence angles and mean reflectivities (VZ-4000) of SP 1 and 2 at the ten target locations. Since there was not enough comparable data with a single VZ-6000 scan, only VZ-4000 reflectivity data was used for the correction, and for further analysis.

Based on the resulting function the topographically corrected reflectivity could be calculated as:

$$ref_{cor} = ref_{non-cor} * ref_{cor-factor}$$

$$ref_{cor-factor} = \frac{1}{(-0.0099 * \text{angle} + 1.7221)}$$

so

$$ref_{cor} = ref_{non-cor} * \frac{1}{(-0.0099 * \text{angle} + 1.7221)}$$

To produce grids of the TLS reflectivity, the point clouds with the corrected laser reflectivity were clipped with the snow covered polygons for each date, time and scan position within the LIS PRO 3D extension of SAGA GIS. The resulting point clouds, displaying the TLS reflectivity of areas covered with snow, were rasterized to 0.5 x 0.5 m grids for further analysis. Histograms of the reflectivity value distribution within the entire research area were extracted for the several scenes.

In addition, reflectivity values were extracted from all the SP1 point clouds along three profiles drawn (1) along the E-W transect and through the snow pits of the sampling sites of each field campaign, (2) through smooth and undisturbed snow in E-W direction displaced in parallel to the south of the snow sampling transect, and (3) from the transect in southern direction towards target #4 close to Lake Weisssee. The extraction of data along those profiles provides ground to directly compare the reflectivity values among dates and times of the scan campaigns. The data was plotted as reflectivity scaled from 0 - 45000 along the range of the profile.

Furthermore, gird statistics at the ten target locations (from in situ snow sampling) were extracted for each campaign date. To do so, for each campaign 10 point shapefiles were created in ArcGIS. The shapefiles were located on undisturbed snow surface just off to the north-eastern corner of the snow pits. With 1 m buffers around the 10 points separate polygons were created and used to extract grid statistics (min, max, mean, std, sum, variance) from 10 cm reflectivity grids of all the scans. Fig. 19 displays the workflow for TLS snow surface reflectivity extraction.

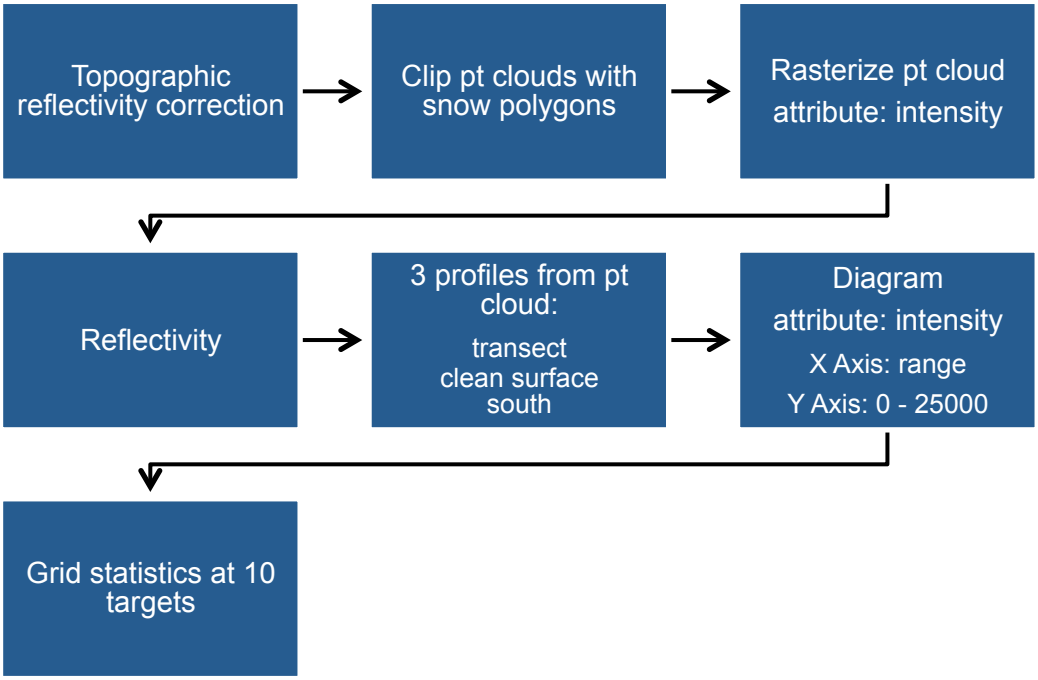

Fig. 19: Workflow for the extraction of TLS reflectivity and profiles in SAGA GIS and LIS Pro 3D.

Terrain

In addition, the SAGA GIS *Morphometry* tool was used to produce grids for slope and exposition of each point cloud in order to investigate the geometric effects on laser scanning reflectivity as well as the influence of topography on LWC (Fig. 20).

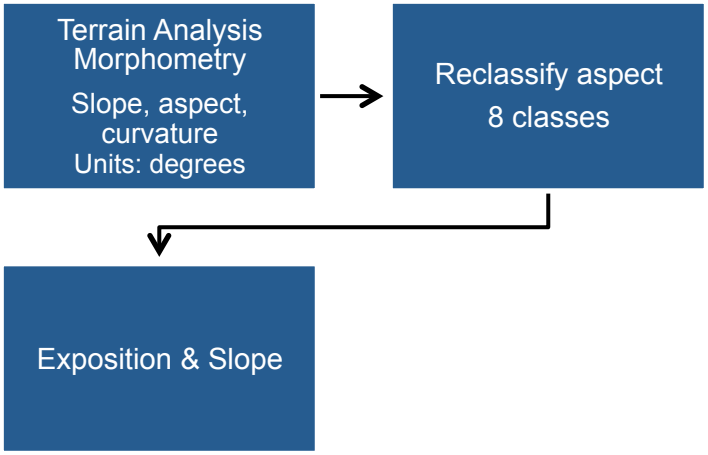

Fig. 20: Workflow for the rasterization of exposition and slope in SAGA GIS.

3.3 LWC and TLS reflectivity

A linear regression model was established based on the relationship of TLS VZ-4000 reflectivity and in situ measured LWC for the months March to May (Fig. 21). Based on the regression LWC was calculated as:

$$LWC = -0.0005 * ref_{cor} + 10.3699$$

For the final snow wetness maps, LWC (%/vol) was manually classified into four classes (dry, moist, wet and very wet), which are in accordance with the International Classification of Seasonal Snow on the Ground (Table 9, Fierz et al., 2009). Through a table join in ArcMap the same classification categories were also used to display the LWC of the Denoth meter snow measurements which were taken in the snow pits along the transect.

Table 9: Snow wetness categories after the International Classification of Seasonal Snow on the Ground (Fierz et al., 2009).

Wetness Content	Category	LWC (%/vol)
Dry	1	0
Moist	2	0 - 3
Wet	3	3 - 8
Very Wet	4	8 - 15

Esri ArcMap 10.1 was used for visualization and mapping of the ALS 2010 DEM, snow depth, targets, TLS reflectivity, profiles, slope, exposition and LWC for the ten grids at SP1. The ALS 2010 base map was displayed as a hillshade in greyscale highlighting the location of SP 1 and 2 on the Kaunertaler glacier road. Exposition was reclassified into eight classes. The target locations were numbered along the transect in the exposition, slope, snow depth, TLS reflectivity and LWC maps and the corresponding profiles were added to some maps. A stretched classification scheme with a blue to red colour ramp was used for the TLS reflectivity and LWC maps, scaled to 0 - 25000 (TLS reflectivity), 0 - 10 vol % (LWC).

4 RESULTS

This section will present the results of the in situ snow samples, TLS reflectivity and the spatio-temporal distribution of LWC from TLS reflectivity.

4.1 In situ snow samples

Table 10 gives an overview of the results of the in situ point scale snow samples at the transect at Lake Weisssee (see also Appendix A).

Table 10: In situ snow samples at the transect at Lake Weisssee.

Date; Time	Target	Exposition	Density (kg/m3)	LWC (vol %)	Hand test	Snow depth (cm)
Mar. 13; 13:00 - 14:33	1	WNW	132	0.222	1	
	2	ENE	144	-0.107	1	
	3	NNE	134	0.205	1	
	4	SSW	170	0.391	1	
	5	ESE	140	0.132	1	
	6	WNW	061	1.171	1	
	7	WNW	133	0.972	1	
	8	NNW	139	0.341	1	
	9	WNW	157	0.905	1	
	10	NNW	125	1.240	1	
Mar. 13; 16:20 - 17:30	1	WNW	131	0.658	1	92.33
	2	ENE	165	-0.096	1	53.00
	3	NNE	129	0.096	1	107.67
	4	SSW	172	-0.382	1	115.00
	5	ESE	150	0.261	1	137.00
	6	WNW	131	0.270	1	121.33
	7	WNW	154	-0.387	1	74.67

	8	NNW	153	-0.370	1	159.67
	9	WNW	151	0.052	1	207.33
	10	NNW	131	-0.128	1	68.33
Apr. 10; 11:36 - 13:22	1	WNW	297	5.149	2	56
	2	ENE	357	5.149	2	46
	3	SSW	369	7.409	2	65.33
	4	NNE	332	6.038	2	77.00
	5	WNW	353	5.916	3	104.00
	6	WNW	323	4.745	2	74.00
	7	WNW	325	5.281	3	52.00
	8	WNW	359	5.792	2	41.67
	9	NNW	353	5.792	2	28.33
	10	WNW	311	6.398	3	58
Apr. 10; 14:29 - 15:06	1	WNW	313	7.265	3	
	2					
	3	SSW	403	8.176	4	
	4					
	5	WNW	327	7.680	4	
	6					
	7	WNW	339	7.265	4	
	8	WNW	317	7.370	4	
	9	NNW	354	7.158	4	
	10	WNW	322	8.369	4	
May 17; 09:52 - 12:16	1	WNW	409	4.539	2	
	2	ENE	454	7.729	3	98
	3	WNW	446	8.130	2	120
	4	WSW	447	7.831	2	
	5	WNW	450	8.031	2	63
	6	WNW	442	8.610	3	70
	7	WNW	441	8.889	3	56.67
	8	WNW	427	8.704	3	65.67

	9	NNW	437	8.130	3	92
	10	NNW	454	9.159	3	
May 17; 15:13 - 16:55	1	WNW	448	5.681	3	72
	2	ENE	442	5.933	3	94
	3	WNW	475	5.319	3	103
	4	WSW	454	5.913	3	77
	5	WNW	472	5.635	3	56.67
	6	WNW	473	5.139		60.00
	7	WNW	480	4.655		71.00
	8	WNW	456	5.409	3	73.67
	9	NNW	472	5.251		81.67
	10	NNW	457	4.893		88

March

The snowpack in March was characterised by a fine-grained snow layer with small wind rippel (Fig. 21). Weather station data at Weisssee indicated 40 cm of new snow four days before the March field campaign. The in situ snow samples yielded snow densities of 133 ± 0.03 kg/m^3 (at 13:00 o'clock) and 147 ± 0.016 kg/m^3 (at 16:20 o'clock) (Table 10). At below freezing air temperatures and permittivities around one, snow LWC was -0.107 - 1.171 % (at 13:00) and -0.387 - 0.658 % in the late afternoon (Fig. 22). The hand test according to the International observational guidelines (WSL, 2008; Fierz et al., 2009) was found to be category one: dry snow with disaggregated snow grains, which had little tendency to adhere together and snow depth ranged from 53 - 207 cm.

Fig. 21: Snow surface with wind rippel on March 13, 2017 (Personal photograph).

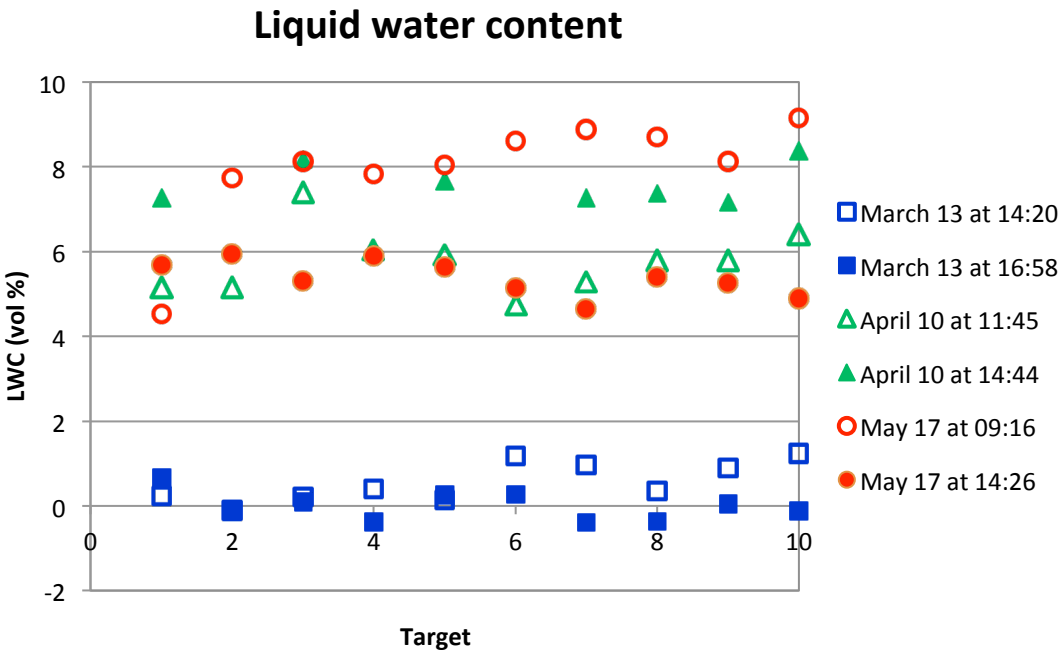

Fig. 22: In situ measured LWC at the ten target locations along the transect at Lake Weisssee. The samples were taken in the mornings and afternoons of March, April and May.

April

With no new snow events since the March sampling, the snow surface structure had transformed until the April 10, 2017 measurements. Snow grains were classified as rounded melt form and had grown in size during air temperatures above freezing. In the morning the snow layer had a crust on top with a looser arrangement of snow grains approximately three cm below the surface. In the afternoon temperatures and solar radiation had strongly increased and the snowpack was soft. Densities were measured at 338 ± 0.037 kg/m^3 (at 11:40) and 339 ± 0.017 km/m^3 (at 14:30) (Table 10). LWC ranged from 4.745 - 7.409 % in the morning and increased to 7.158 - 8.369 % in the afternoon (Fig. 22). The hand test yielded categories 2 (moist) and 3 (wet) in the morning and categories 3 and 4 (very wet, water could be pressed out of the sample) in the afternoon. Snow depth ranged from 21 - 106 cm.

May

On May 17, 2017 the snow surface was classified as a melt-freeze crust with refrozen polycrystals (MFcr, Fierz et al., 2009) at the surface and with rounded frozen clustered grains approximately three cm below the snow surface (Fig. 23). Snow densities of 440 ± 0.017 kg/m^3 (at 10:00) and 462 ± 0.017 kg/m^3 (at 15:15) were measured (Table 10). The LWC in the morning was the highest measured during the study (7.729 - 9.195 %) and decreased to 4.655 – 5.933 in the afternoon (Fig. 22). The hand test was found to correspond to category 2 (moist) and 3 (wet) in the morning and to 3 in the afternoon. Snow depth ranged from 55 - 112 cm.

Fig. 23: Snow surface grain structure in the afternoon of May 17, 2017 (Personal photograph).

4.2 TLS reflectivity

The accuracy of the TLS point cloud registration was 0.033 ± 0.05 m at planar snow-free surfaces. The TLS VZ-4000 was capable of operating on snow surfaces returning a good amount of reflectivity signals. Depending on the snow properties, range and incidence angle this signal varied in its intensity. Within this section the results drawn from TLS reflectivity data will be present, compared among scan dates, scan times and to the VZ-6000.

4.2.1 Seasonal development of TLS reflectivity

A general decrease in laser signal reflectivity can be observed from March to May for the overall research area. The reflected TLS signal was mapped for the months March, April and May (Figures 24-26). The afternoon scans (between 14 - 15 o'clock) were used for the seasonal comparison in order to analyse at conditions of similar solar insulation.

In March, a clear difference between undisturbed and disturbed snow surfaces is visible; the snow pits and foot tracks from snow sampling have higher reflectivity values, as well as the skiing route in the upper left corner (Fig. 24). Furthermore, higher values can be observed near target 4 on the southerly exposed shore of Lake Weisssee as well as on southern slopes and north-western slopes (e.g. near the road).

In April, the reflected signal intensity is clearly reduced compared to March. Nevertheless, the disturbed snow surface of the snow pits and the footpath along the transect also show higher reflectivity than the undisturbed snow surfaces (Fig. 25). Furthermore, the north-western as well as south-western slopes can clearly be distinguished by their higher reflectivity. The skiing route, however, shows different characteristics compared to the data of March. In April, it did not reflect stronger than the surrounding area; in fact, it had a very low reflectivity similar to that of the easterly exposed slope of the depression between target 5 and 6 (a covered creek).

The TLS results of the May scan also show much lower laser signal reflectivity than the March scan (Fig. 26). Compared to the April data, it is more homogenous over the whole research area with patches of very high reflectivity where the laser beam hits soil surface.

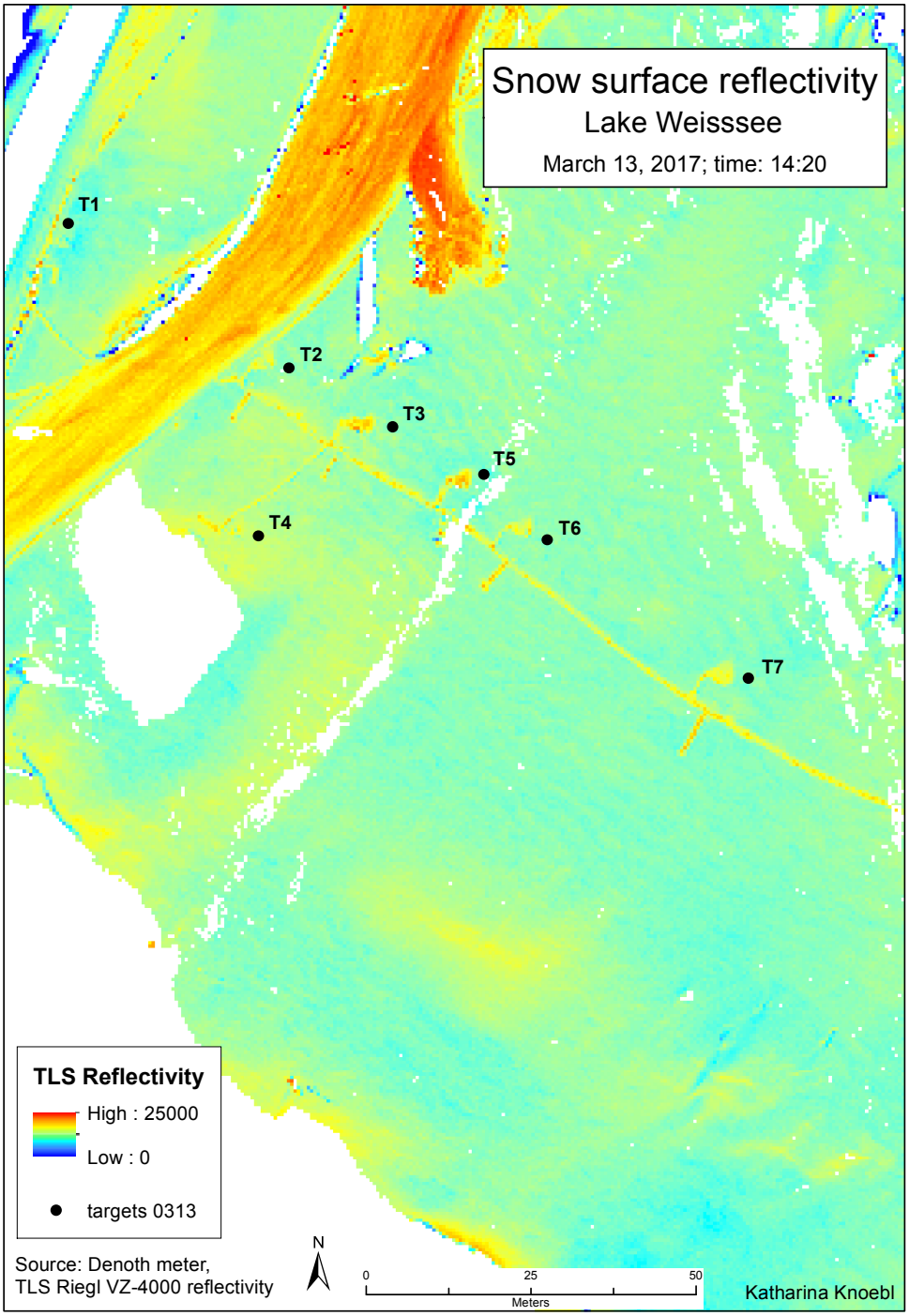

Fig. 24: TLS VZ-4000 snow surface reflectivity in the afternoon of March 13, 2017. Scanned from scan position 1 (distance: 150 - 300 m) to the research site Lake Weisssee.

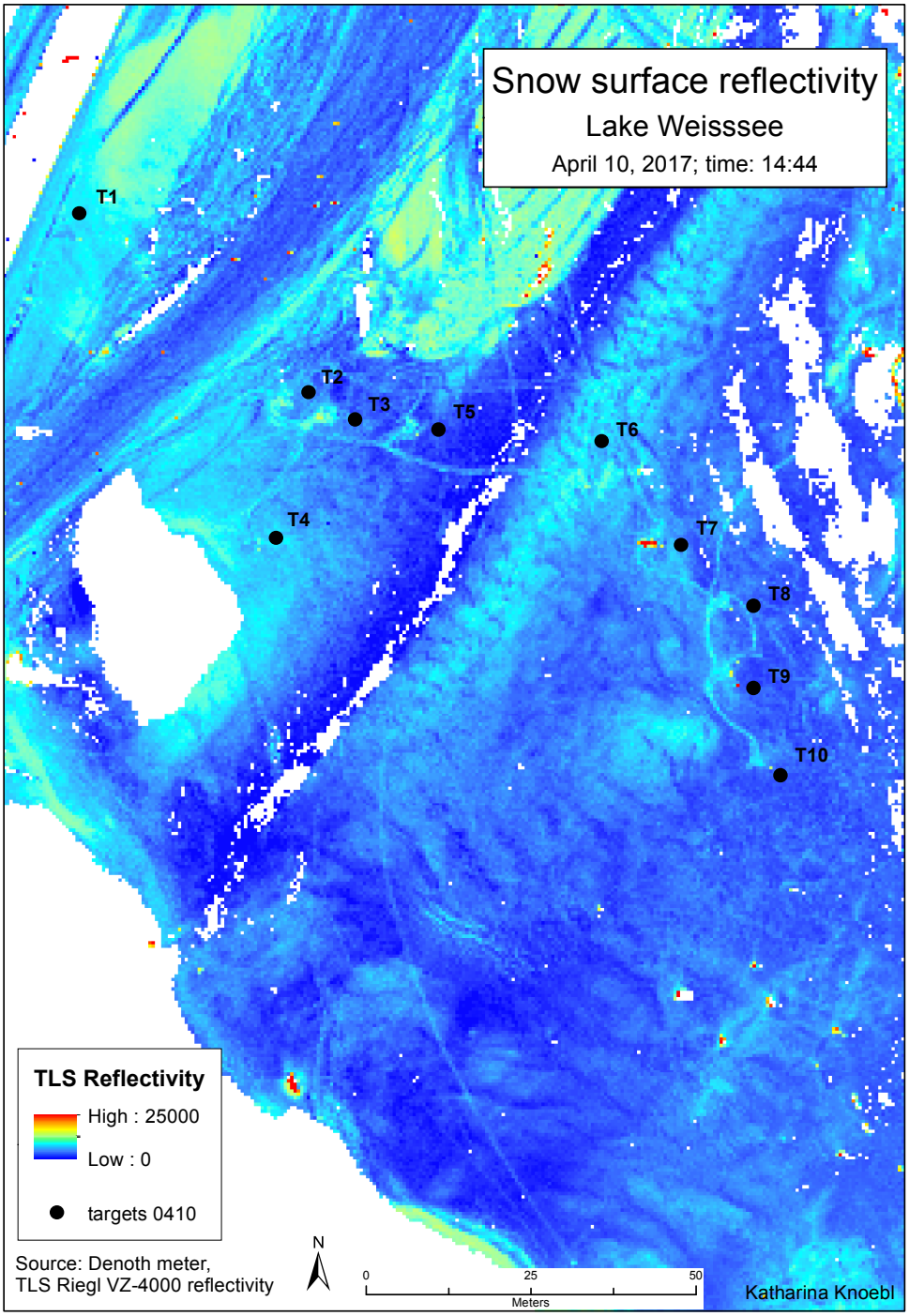

Fig. 25: TLS VZ-4000 snow surface reflectivity in the afternoon of April 10, 2017. Scanned from scan position 1 (distance: 150 - 300 m) to the research site Lake Weisssee.

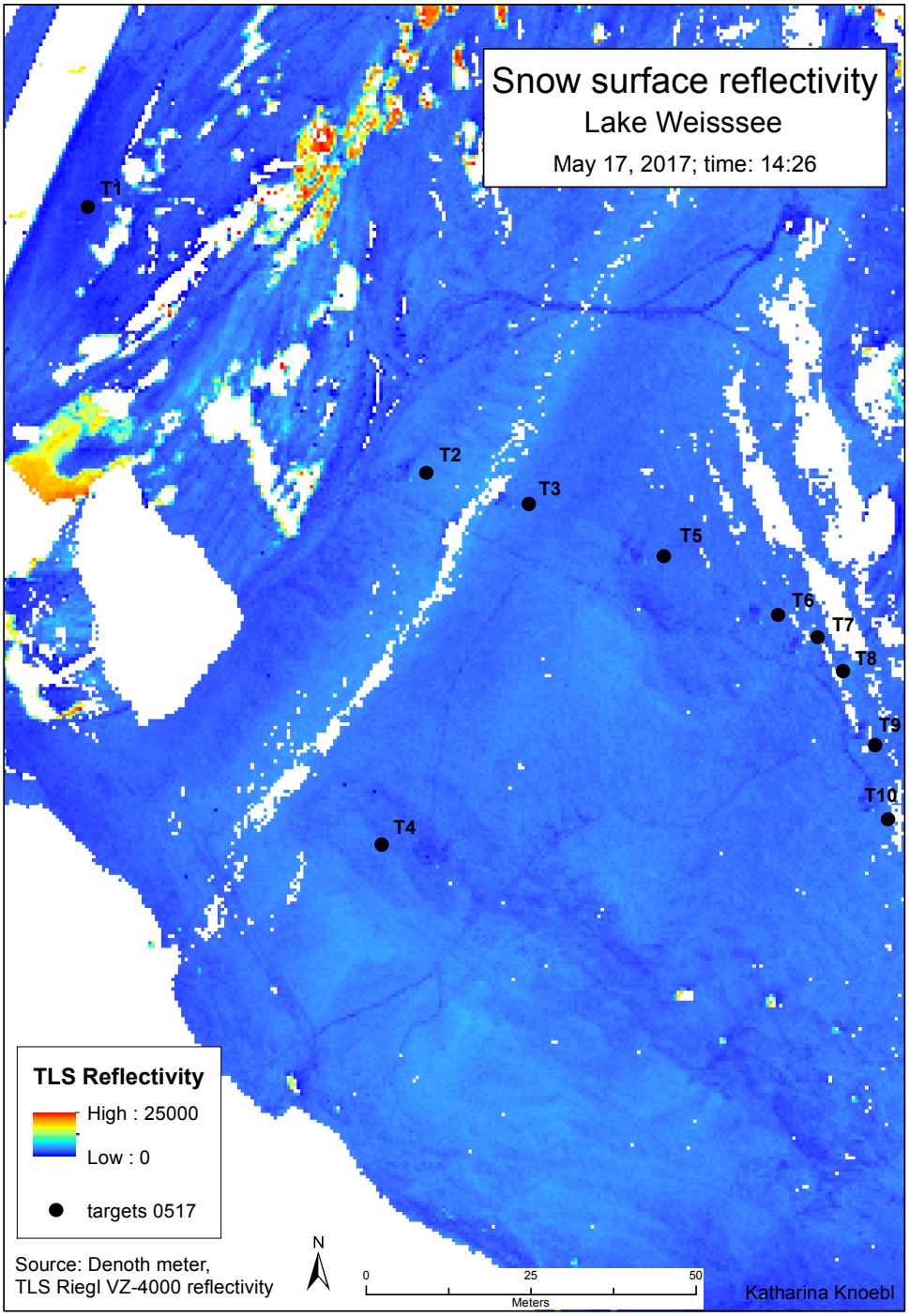

Fig. 26: TLS VZ-4000 snow surface reflectivity in the afternoon of May 17, 2017. Scanned from scan position 1 (distance: 150 - 300 m) to the research site Lake Weisssee.

4.2.2 Diurnal development of TLS reflectivity

TLS data showed a decreasing trend of snow surface reflectivity over the term of the scan day. While there was not much change of snow surface reflectivity between the two scans in March (temperatures below freezing), the April and May scans revealed a diurnal reduction of the reflected signal intensity. Especially the April data indicates a very distinctive reduction of the signal in the afternoon (Fig. 27). Furthermore, spatially distributed patches of higher reflectivity could be observed in the morning and afternoon of April and to a smaller extend in the morning of May.

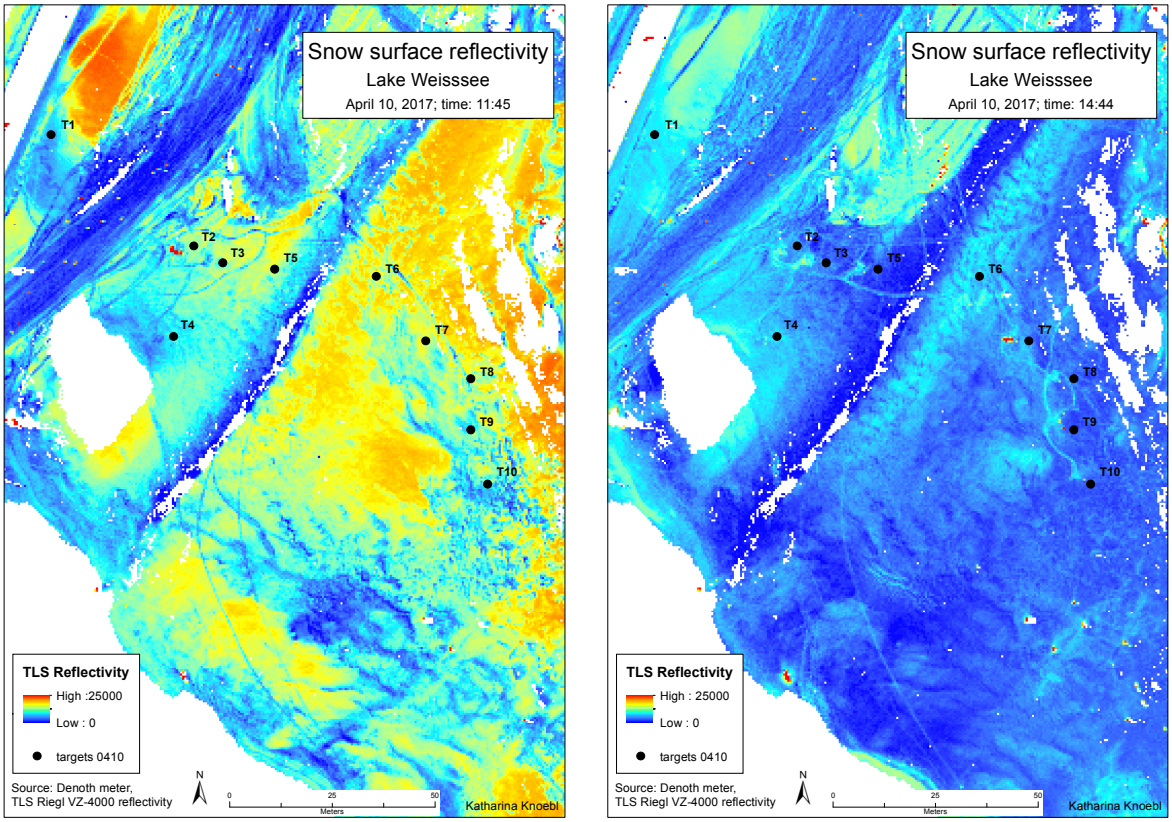

Fig. 27: Diurnal development of TLS snow surface reflectivity at the research site Lake Weisssee on April 10, 2017.

4.2.3 TLS reflectivity at differing scanning wavelengths

Results show that the TLS VZ-4000 operating at λ 1550 nm is even capable of obtaining data on wet snow surfaces. While the VZ-4000 had quite low reflectivity, the VZ-6000 operating at the shortwave NIR λ 1064 nm had clearly higher reflectivity (Fig. 28). Disturbed snow features such as the snow pits, the transect and skiing tracks reflected stronger. Especially the area around target 1 displays noticeably higher values, while the depression between target 2 and 3 is detectable because of its lower reflectivity.

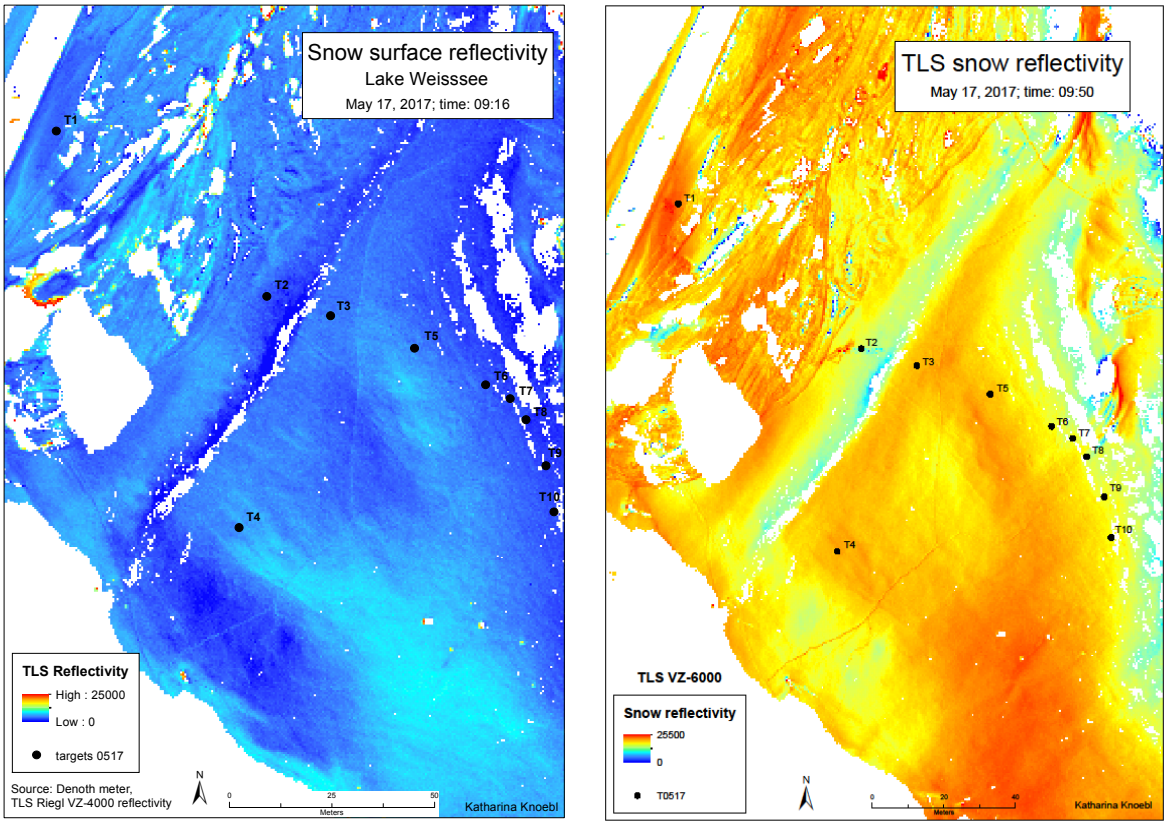

Fig. 28: Comparison of TLS VZ-4000 (right) and TLS VZ-6000 (left) snow surface reflectivity in the morning of May 17, 2017 at Lake Weisssee.

4.3 Liquid water content derived from TLS reflectivity

TLS reflectivity correlates with the LWC measured in situ (Fig. 29). The linear regression displays the relationship of LWC from Denoth field sampling and TLS reflectivity data at the target locations along the transect. Wetter snow surfaces had lower TLS reflectivity compared to the drier snow.

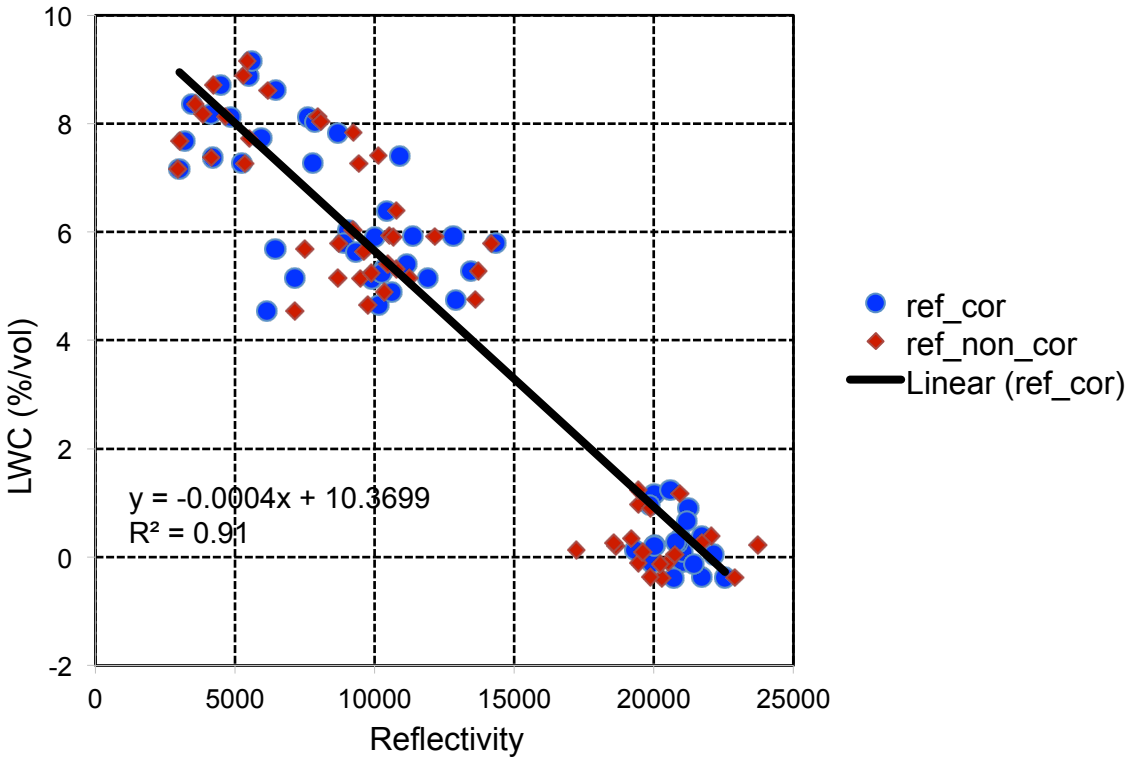

Fig. 29: Linear regression of in situ measured LWC and TLS VZ-4000 reflectivity at the research site Lake Weisssee. Blue: topographically corrected reflectivity, red: reflectivity before correction.

4.3.1 Seasonal development of LWC distribution

In situ measured LWC and spatial distribution of LWC derived from TLS reflectivity correlate well (Figures 30-32). Uncertainties appear close to the class limits. A clear increase of LWC from March with 0 – 3 % LWC (category dry and moist) to April with 3 – 10 % LWC (category wet and very wet) can be observed in the afternoon scans. Yet, May did not indicate a LWC of the highest category in the afternoon (as shown in Fig. 32); the morning scan, however did (Fig. 33).

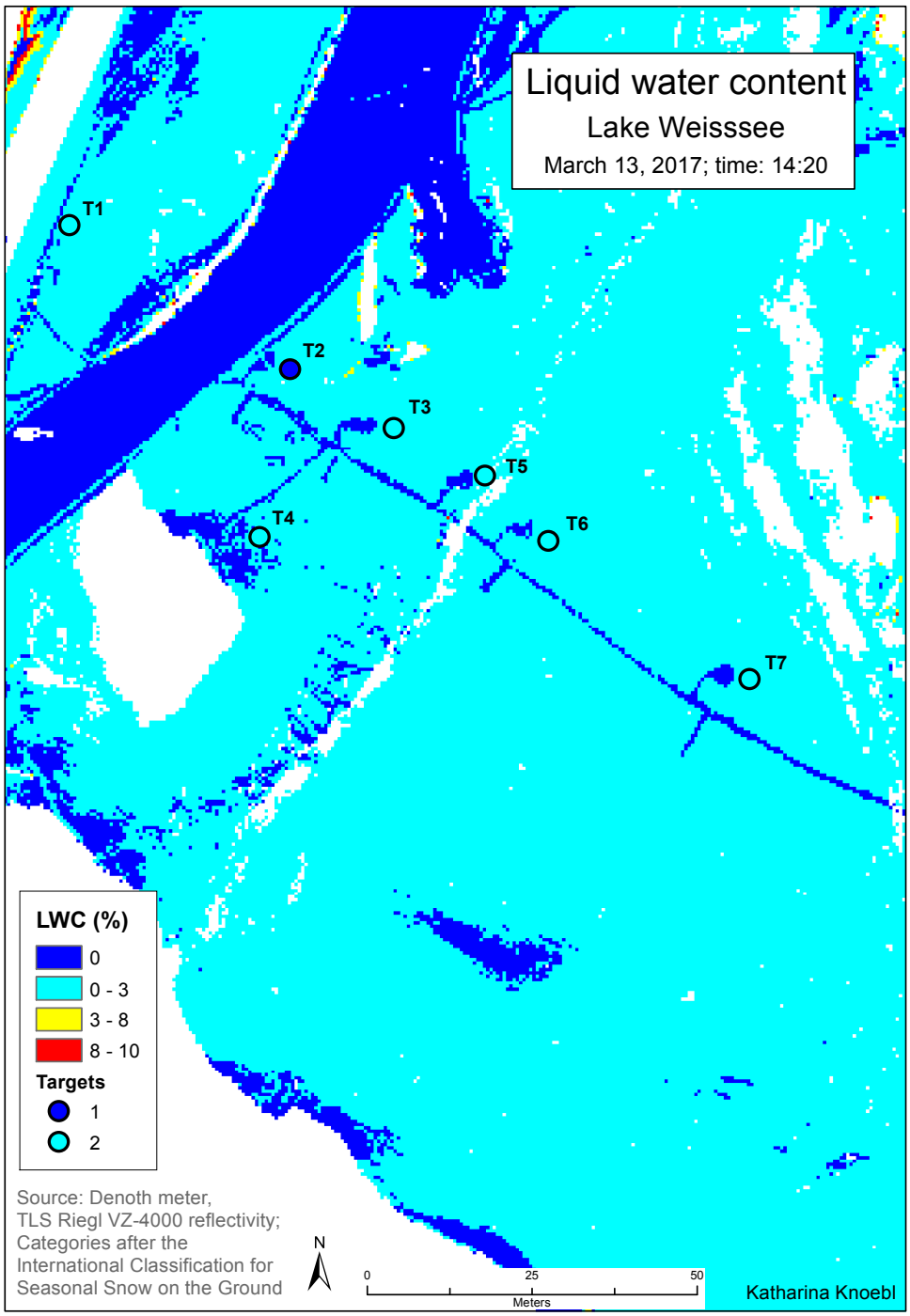

Fig. 30: Derived LWC distribution in the afternoon of March 13, 2017. Data classified based on the linear regression of in situ LWC and TLS reflectivity and categorized into four classes (dry, moist, wet, very wet) according to the International Classification of Seasonal Snow on the Ground (Fierz et al., 2009).

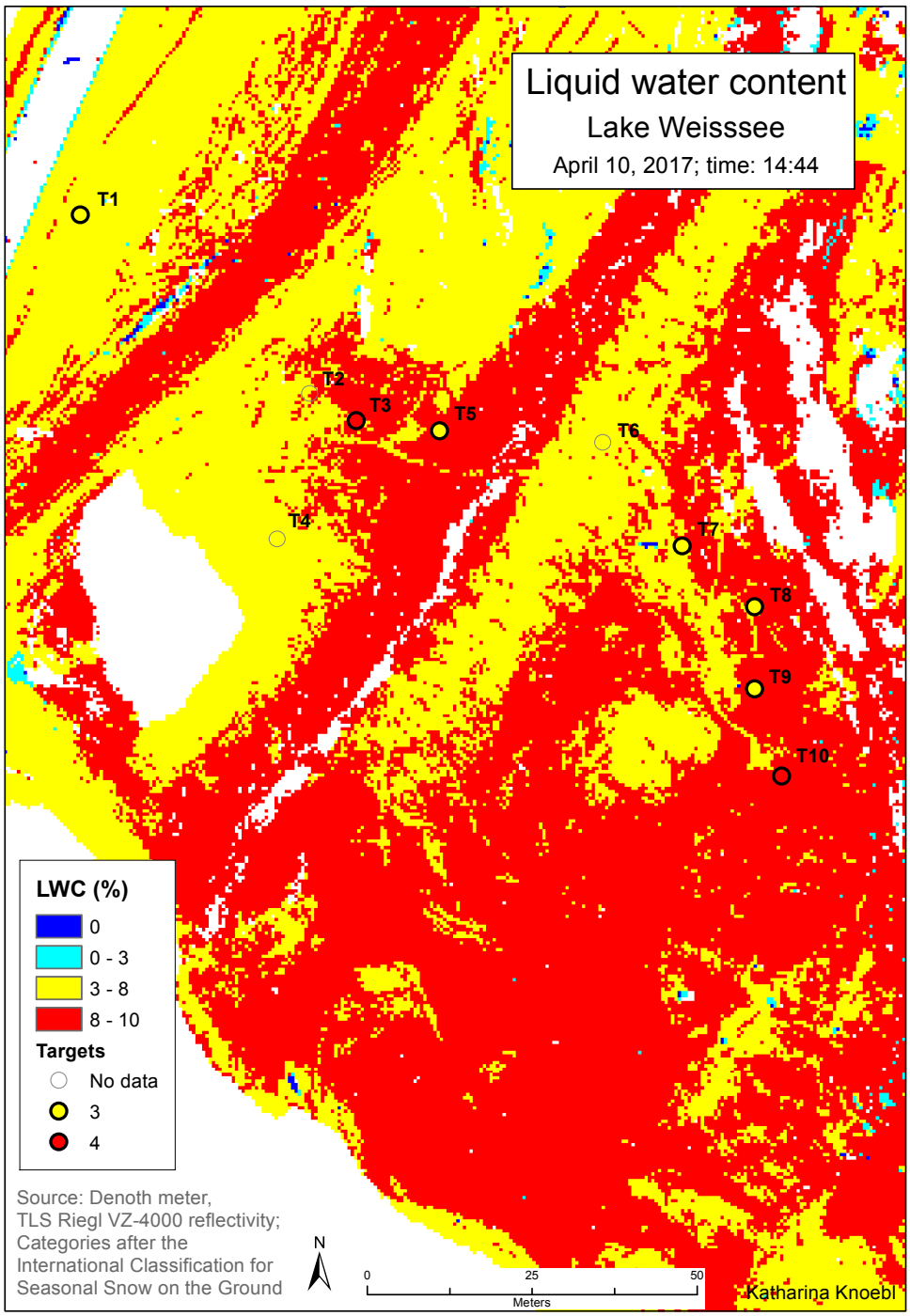

Fig. 31: Derived LWC distribution in the afternoon of April 10, 2017. Data classified based on the linear regression of in situ LWC and TLS reflectivity and categorized into four classes (dry, moist, wet, very wet) according to the International Classification of Seasonal Snow on the Ground (Fierz et al., 2009).

Fig. 32:

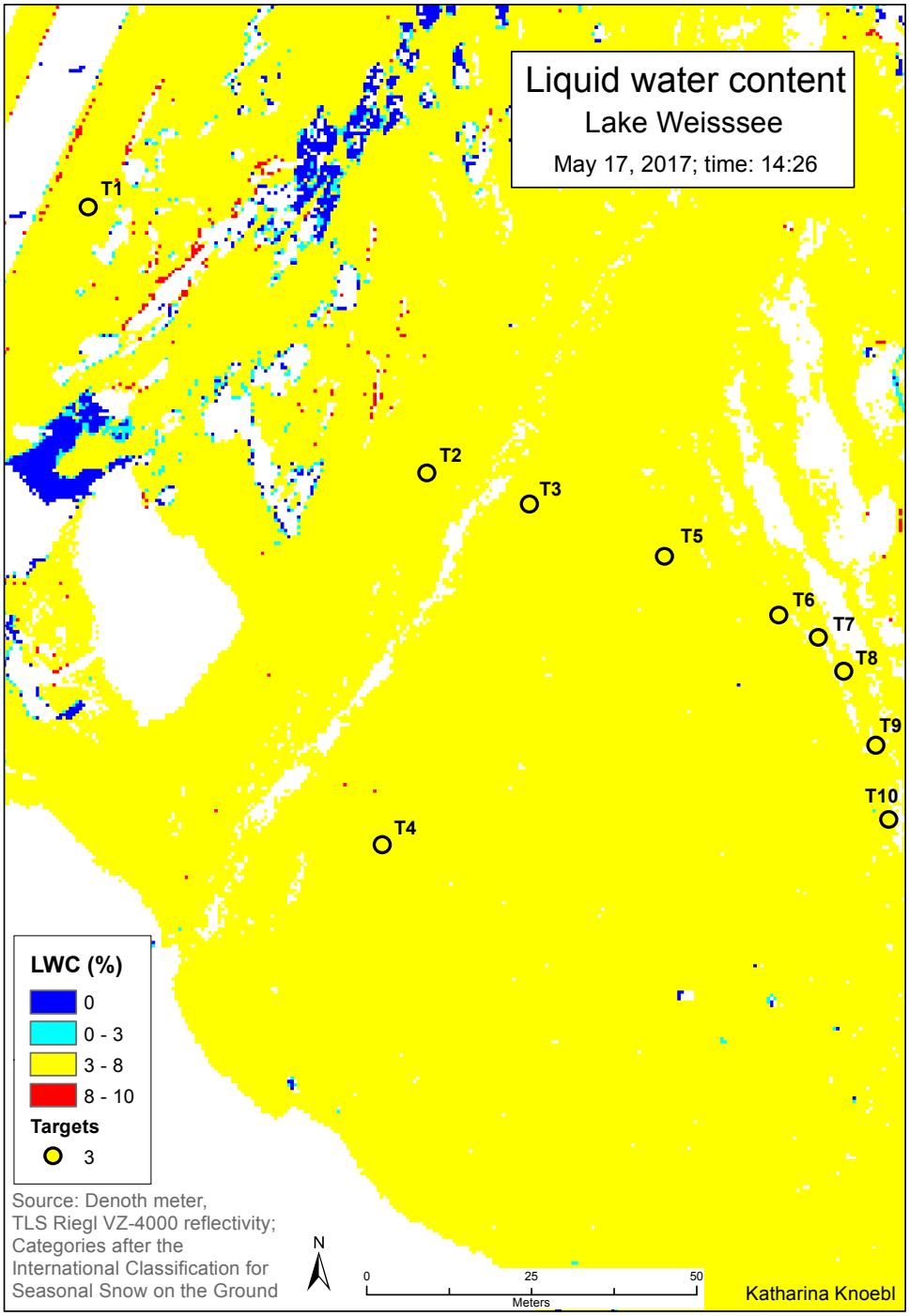

Derived LWC distribution in the afternoon of May 17, 2017. Data classified based on the linear regression of in situ LWC and TLS reflectivity and categorized into four classes (dry, moist, wet, very wet) according to the International Classification of Seasonal Snow on the Ground (Fierz et al., 2009).

4.3.2 Diurnal development of LWC distribution

Diurnal changes of snow wetness can be mapped from LWC derived from TLS reflectivity. In the late afternoon scan of March a slight decrease in LWC could be observed in some patches of the research area (Fig. 33). In the afternoon of April, LWC increased to the highest category (very wet) in large parts of the area (Fig. 34). Data in the afternoon of May however, did not show any LWC of the highest wetness category compared to the morning (Fig. 35). However, patches of category 1 (dry) appear where the skiing slope was located. Also, some signal drop outs (white spaces) could be observed. Fig. 36 shows a picture of the research area at Lake Weisssee taken in the afternoon of May 17, 2017. For maps with a stretched classification of LWC refer to Appendix A.

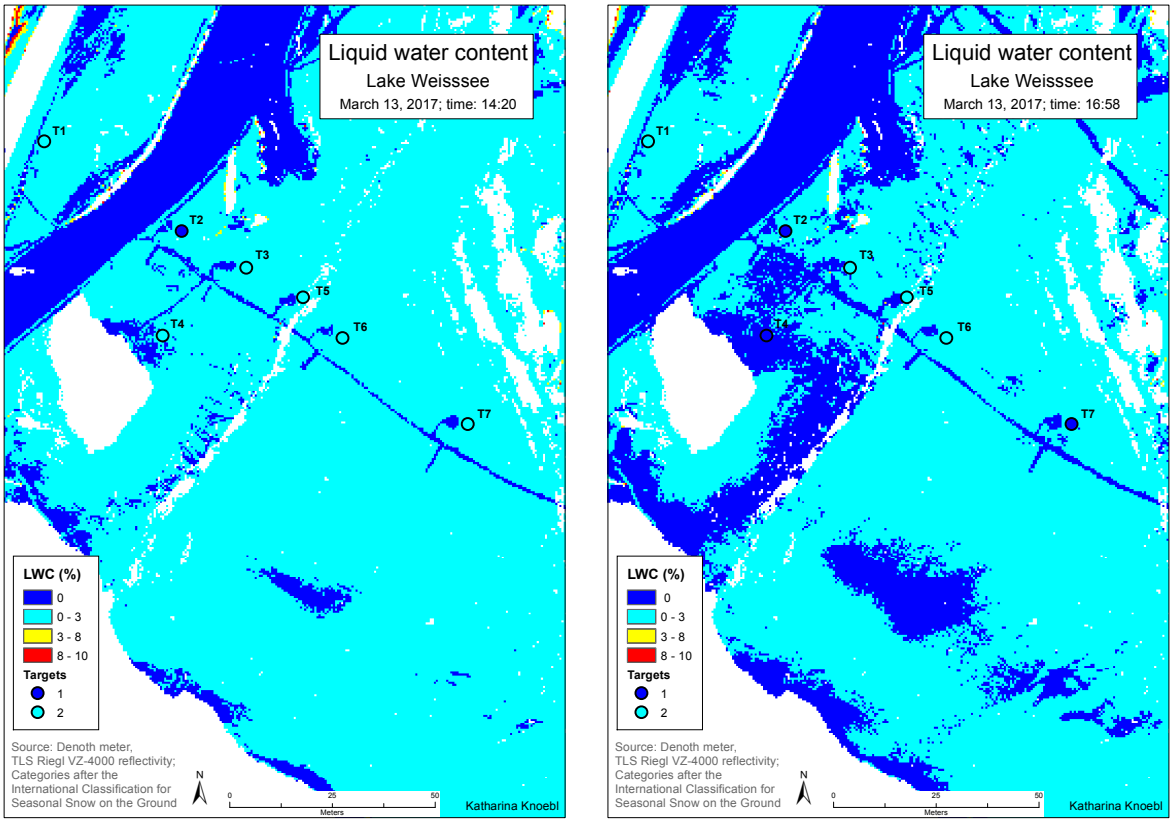

Fig. 33: Diurnal comparison of the liquid water content (LWC) distribution at the snow surface at the research site Lake Weisssee on March 13, 2017. Data classified based on the linear regression of in situ LWC and TLS reflectivity. Blue circles indicate the locations of in situ LWC measurements, category 1 (dry) and 2 (moist).

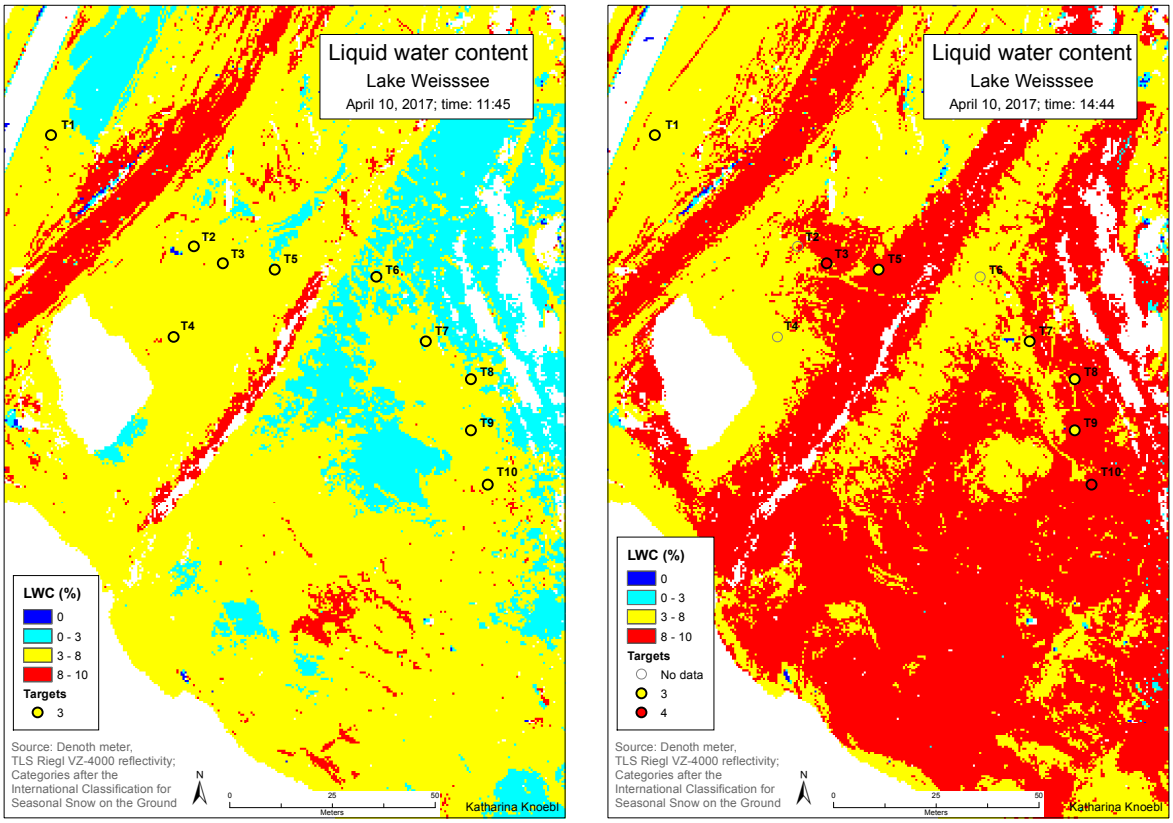

Fig. 34: Diurnal comparison of the liquid water content (LWC) distribution at the snow surface at the research site Lake Weisssee on April 10, 2017. Data classified based on the linear regression of in situ LWC and TLS reflectivity. Yellow and red circles indicate the locations of in situ LWC measurements, category 3 (wet) and 4 (very wet).

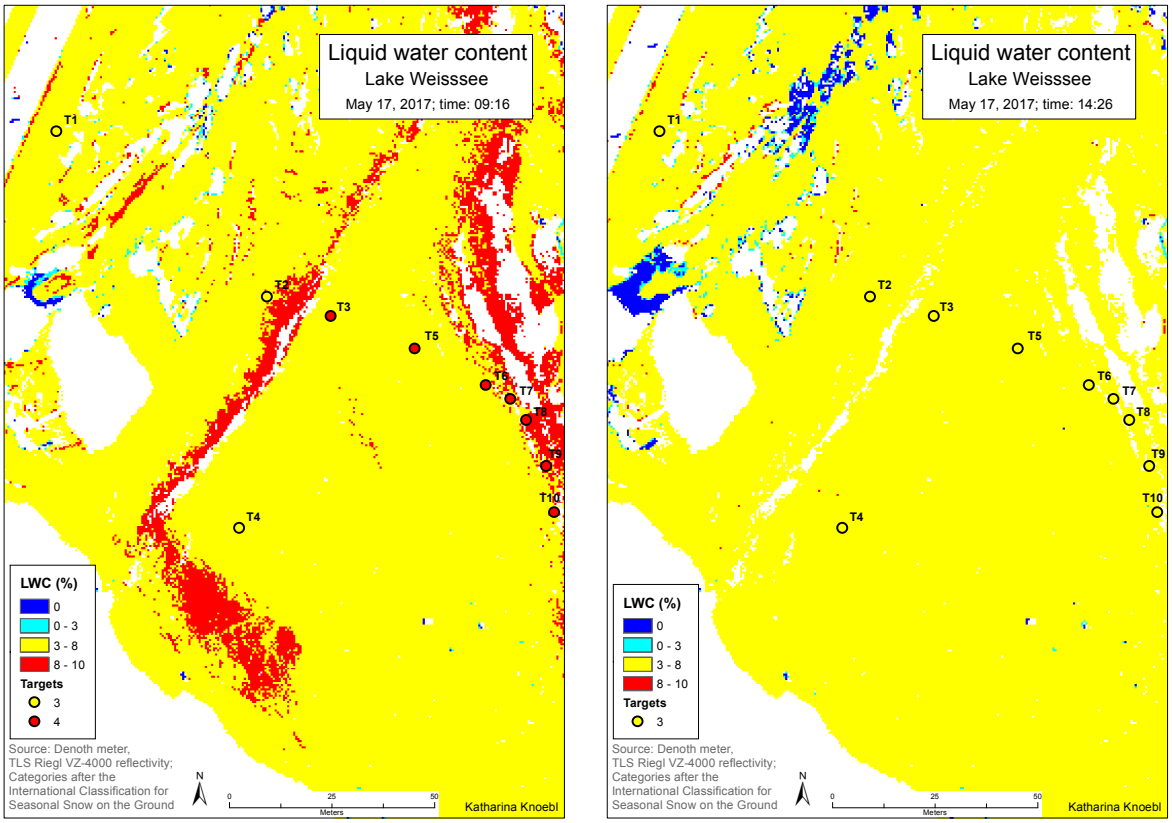

Fig. 35: Diurnal comparison of the liquid water content (LWC) distribution at the snow surface at the research site Lake Weisssee on May 17, 2017. Data classified based on the linear regression of in situ LWC and TLS reflectivity. Yellow and red circles indicate the locations of in situ LWC measurements, category 3 (wet) and 4 (very wet).

Fig. 36: Research area Lake Weisssee in the afternoon of May 17, 2017 (Personal photograph).

5 DISCUSSION

This study found that snow wetness could be spatially and temporally analyzed from TLS reflectivity data. Terrestrial laser scans conducted during March, April and May 2017 and concurrent in situ snow surface samples yielded a good correlation for LWC based on TLS reflectivity. A general increase of diurnal and seasonal LWC distribution could be observed and mapped. This section will discuss the results of this study as well as some limitations and uncertainties.

5.1 TLS reflectivity and LWC

TLS reflectivity was found to be a promising method for high-resolution investigation of spatial LWC distribution at the snow surface. The technique is based on the different spectral reflectance of water and snow. The laser pulse of a TLS operating at NIR gets reflected from the first cm of the snow surface (Deems et al., 2013).

Increasing solar radiation duration and intensity throughout a day and the season causes consecutive melt/freeze cycles within the snow pack due to wet snow metamorphism. Increased wetness leads to clustering of the ice crystals (Colbeck, 1979), which lets them grow into larger grains and thus results in a reduction of reflectivity in the NIR (Wiscombe and Warren, 1980; Green et al., 2002; Rees, 2006; Prokop, 2008; Deems et al., 2013).

From Fig. 27 a decreasing trend in reflectivity can be observed from the morning scan (11:45) in April to the afternoon scan (14:44). As it can be assumed that the snow grain size is not changing significantly within the course of three to five hours (the time period between the measurements), the reduced laser backscatter is caused by a different effect. In situ snow sampling results and the LWC maps indicate an increased LWC in the afternoon. Thus, increasing snow wetness might represent an influencing factor on the loss in laser signal reflectivity. However, the exact proportion of grain size and LWC cannot be quantified.

Furthermore, laser signal absorption from liquid water can cause laser signal dropouts (Wolfe and Zissis, 1993; Deems et al., 2013; Hartzel et al., 2015). Prokop (2008) found that the rate of laser pulse returns was only 50% with wet snow conditions.

The relationship between snow reflectivity in the NIR and snow density is less clear. TLS reflectivity maps in this study displayed higher values on disturbed snowpacks (e.g. foot tracks, skiing tracks), which would indicate more compacted and denser snow layers. Bohren

and Beschta (1979) found no relationship between reflectivity and density in their study of compacted snow.

Additionally, the snow cover “can be assumed pollution-free because in the NIR snow surface reflectivity is not affect by absorbing particles, such as soot or desert dust; ice itself is more absorptive. Impurities affect the reflectivity only in the visible wavelengths” (Warren and Wiscombe, 1980).

5.2 Scanning wavelength

The study found that the TLS VZ-4000 operating at a wavelength of 1550 nm was suitable for the application on wet snow. However, compared to the TLS VZ-6000, reflectivity was less intense under melting conditions in May and especially suffered dropouts at longer scan distances. Referring to the diagram of spectral reflectance of snow (Fig. 7), it can be observed that at a wavelength 1064 nm the covered range of grain sizes is larger compared to a wavelength of 1550 nm. Thus, it is expected that varying grain size have a larger influence on laser signal returns at a scanning wavelength of 1064 nm (operating wavelength of RIEGL VZ-6000). “At 1.0 - 1.3 µm (1000 - 1300 nm), snow reflectivity is especially sensitive to grain size” (Wiscombe and Warren, 1980; Nolin et al., 1993; Dozier and Painter, 2004). However, in the shortwave IR wavelengths, the operating wavelength of TLS RIEGL VZ-4000, ice is absorbing stronger and the reflectivity at the snow surface is reduced to <10% (Deems et al., 2013).

As the TLS RIEGL VZ-4000 operates on the shortwave IR (1550 nm) it was not designed originally for the application on wet snow surfaces. However, as this project infers, a TLS of this class was able to return data of wet snow surfaces at moderate distance. Subsequently, the returned signal intensity can be used to distinguish between the types of snow condition. Therefore, the shortwave IR TLS can be suggested to practitioners and engineers for avalanche mitigation and hydrological purposes because based on its operating wavelength it provides a wide range of application options, while being eye safe during its operation.

5.3 LWC from in situ snow sampling

TLS reflectivity could be verified by in situ LWC samples measured with a Denoth meter. The LWC is highly depended on the diurnal weather situation and snow cover temperature. The in situ LWC samples (as displayed in Fig. 22) in March did not show a diurnal increase. The second snow sampling in the late afternoon of March (at 16:20 – 17:30) yielded slightly lower LWC than the first measurements; however, this could be caused by decreasing temperatures (-5°C during sampling) and refreezing processes in the late afternoon. Additional "snow temperature measurements may be an indicator of dry snow, although small amounts of liquid water even have been measured in snow at temperatures below 0°C (< 1 vol. %)" (Techel and Pielmeier, 2011; Kattelmann and Dozier, 1999). Some LWC results indicate negative values. Additionally to an already very low LWC this could be the result of a measurement error caused by snow compression when the density cylinder or the Denoth meter got inserted into the snow layer. Furthermore, the early snow density measurement of approximately 130 kg/m^3 on March 13 corresponds well with snow densities for fresh snow (50 - 120kg/m^3) found in literature (Pomeroy and Brun, 2001). Due to snow metamorphism from diurnal and daily temperature gradients, snow density keeps increasing at different rates. The new fine-grained snow structure and below freezing air temperatures, hold little liquid water and imply dry snow conditions. Perovich (2007) found in a dual-detector spectroradiometer experiment that even a thin layer of new snow does enhance albedo. The small snow grains have a higher spectral reflectivity than aged snow with larger grains (Wiscombe and Warren, 1980).

The more intense solar radiation and warmer air temperatures in the afternoons of April and May demonstrate melting conditions. Also, the larger well-rounded snow grains resulting from melt-freeze metamorphism suggest higher liquid water contents late in the season. However, Techel and Pielmeier (2011) point out that it is particularly difficult to measure the LWC of thawing melt-freeze-crusts because the range of LWC and hardness is larger. Especially in the mornings of April and May the melt-freeze snow crust was rather hard and inserting the Denoth sensor plate as well as the cylinder was difficult and might have produced some measuring error. Moreover, during the field campaign in May the snow density measurements were done by a different person, which could have caused an error.

Interestingly, the in situ measured surface LWC in the afternoon of May was lower than the morning measurement, which could be due to liquid water percolating towards deeper snow layers. As mentioned in 1.4.4, it is likely that "in very wet snow packs that gravitational flow is dominating (funicular regime) and water will drain" (Mitterer et al., 2013).

Furthermore, the order of the afternoon sampling in March and May was reversed due to better operability and an increased avalanche hazard on the steeper western slope of the transect in the May field campaign. It was decided to start sampling at target 10 rather than target 1. The effect can be observed in Figure 22 with the LWC at target 10 (4.89%) being higher than at target 1 (5.27%).

5.4 Transferability of the method

The RIEGL laser scanner software automatically corrects for the range of the laser signal providing a distance independent relative reflectance (Pfenningbauer and Ullrich, 2010). However, Wagner et al. (2004) pointed out that the reflectivity and directionality of the backscattered signal strongly depends upon the surface properties and the orientation of the target. In order to make the method, introduced in this study, applicable to other areas and slopes, a topographic correction was implemented to correct for the differing incidence angles when scanned from other scan positions. Nevertheless, this correction was only drawn from the incident angles and reflectivities at the ten target locations; further research based on the point cloud needs to be conducted.

5.5 Limitations

Even tough LiDAR is the most progressive, constantly developed surveying technology to gather precise geographic information and structural data of surfaces at this day, and this study was conducted to the best knowledge and at the most recent state of the art, some limitations and uncertainties will be discussed in this section.

5.5.1 Laser beam divergence, range and pulse repetition rate

Even though a laser pulse is very focused and spatially coherent, it maintains a physical spread as it travels through space (Deems et al., 2013; Coren & Sterzai, 2006). RIEGL (2017ab) state that the laser beam diverges at a known rate (e.g. TLS RIEGL VZ-4000 has a laser beam divergence of 0.15 mrad and TLS VZ-6000 at 0.12 mrad). The resulting laser footprint for VZ-4000 is specified as 18 mm at exit and 75 mm at a distance of 500 m, and

VZ-6000 as 15 mm at exit and 60 mm at 500 m. As the footprint diameter increases with range, with high resolution an overlapping/oversampling error, positional uncertainty and a decrease of the point cloud resolution occurs (Beraldin et al., 2010). TLS reflectance also decreases with increasing distance from the scanner. Data quality can be improved by adjusting the pulse repetition rate (PRR). By lowering the PRR (e.g. 30 kHz) the laser pulse has more energy and is reflected stronger from the target surface. This input could be applied at short distance and MTA zone 1. With increasing range a higher PRR rate gets necessary; however, the result is reduced energy and possibly wrong MTA zone assignment since more laser pulses might be in the air at the same time.

5.5.2 Scanning geometry and incident angle

The new TLS instruments are equipped with very good calibration and correction functions; however, an incorrect scanning geometry with too large incident angles and ranges cannot be resolved. A large incident angle produces a bigger footprint, which distorts the measurement (Schaer et al., 2017). Also, the density of laser point data is reduced with high incidence angles (Lindenbergh et al., 2005). Furthermore, error of the laser measurement increases with increasing distance to the target (Prokop 2008; Soudarissanane et al., 2007; Deems et al., 2013).

Also, vertical errors on slopes can occur from uncertainty in horizontal position on inclined slopes and the laser point may seem to be located below or above the actual surface (Fig. 37a, Hodgson and Bresnahan, 2004). These terrain-induced errors can also result from laser beam divergence over a steep slope, which distorts the returned laser pulse (“time walk”) and the threshold of the scanner’s signal registration may be reached (Fig. 37b, Baltsavias, 1999).

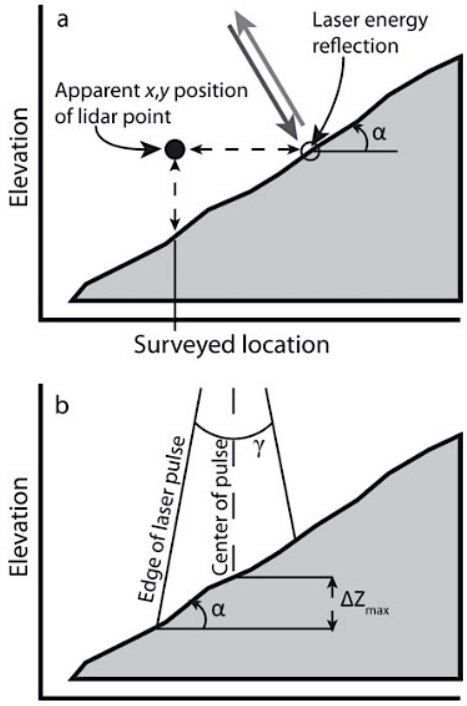

Fig. 37: (a) Positional error induced by horizontal inaccuracy (after Hodgson and Bresnahan, 2004). (b) 'Time walk' error from laser beam divergence over a steep slope; α = slope angle, γ = laser beam divergence, ΔZmax = maximum elevation error (after Baltsavias, 1999).

5.5.3 Environmental conditions

Since the laser pulse needs to traverse through the atmosphere (different atmospheric layers) to reach the target surface and return to the receiver, natural errors from atmospheric variations in temperature, air pressure and humidity produce uncertainties (Fey and Wichmann, 2016). These uncertainties are hard to assess or correct for since it is not possible to accurately measure all these factors. Furthermore, wind can influence the scan because motion and small vibrations can highly distort the aquired data. The laser scanner needs to be mounted on stable ground (Deems et al., 2013). Also, the possible melting of snow due to solar radiation needs to be considered when choosing the ground medium.

5.5.4 Registration errors

Errors from registration can have a big influence on the resulting data and can result in low accuracy. There are several methods for point cloud registration and high expertise is required to select the appropriate method and apply it properly. Further research to improve data registration workflows is highly needed as it potentially limits the processing and use of the recently highly improved data quality and resolution of new LiDAR instruments.

5.5.5 Systematic errors

Furthermore, systematic errors from manufacture and assembly can exist in instruments (Vosselman and Maas, 2010). At a scan rate of 100000 to 200000 measurements per second and a laser beam divergence of 0.15 mrad the manufacture of oscillating mirror and rotating head have to be at highest precision.

5.5.6 Methodological errors

Planning of the scanning campaign is an essential factor for a successful data acquisition. The choice of scanner (type, range, operating wavelength(s)), weather conditions (precipitation, fog), location (required permit, transport of equipment), position (incidence angle, field of view), time (changing solar radiation might affect surface properties), functioning equipment (scanner, batteries, thermometer, altimeter, tripod), scanning parameters (point repetition rate, resolution - oversampling), procedures and handling and user experience have to be considered. In addition, data processing steps have to be thought of, such as reflectors, GPS, visible and stable objects for registration and geo-referencing purposes.

Since the research area is located in a high alpine area where weather conditions can change rapidly, scanning campaigns were planned for days with good predictions. Planning field campaigns needed a coordination of (1) weather conditions (no strong winds, no snow fall, no low clouds, constant conditions throughout the day); (2) satellite overflight (correct day, but also time since a 4 or 5 o'clock overflight required the organization of an overnight stay in the Kaunertal valley; (3) availability of TLS and TIWAG employee; (4) availability of Denoth meter**.** It was scanned several times throughout the period of a day and sufficient electricity had to be provided for in the field. Furthermore, there were skiers around during

the opening hours of the skiing resort. For this reason scan positions and the location of the snow sampling transect had to be chosen with consideration.

Despite limitations and possible error sources, the results of this study are very promising and provide a ground for spatio-temporal snow wetness analysis and further research.

6 CONCLUSION AND OUTLOOK

The study concludes that the application of TLS reflectivity provides a promising option for the investigation of spatial LWC distribution and temporal changes of snow surface wetness based on the principle of differing spectral reflectivities of water compared to ice. As an accurate and high-resolution method TLS reflectivity could potentially be applied to aid in the spatially confined, time consuming and labour intensive point-scale in situ LWC sampling. Especially near avalanche prone slopes and in hardly accessible mountainous terrain, this new method is promising for its safety and effectiveness.

It was found that wet snow surfaces have a lower TLS reflectivity at NIR wavelengths than dry snow. Accordingly TLS reflectivity data of RIEGL VZ-4000 and VZ-6000 could be used to map areas of increased surface wetness. In situ LWC samples measured with the Denoth meter correlate well with TLS reflectivity. Reflectivity at the snow surface decreases diurnally and seasonally from March to May due to increasing LWC. Furthermore, results show that the TLS VZ-4000 operating at λ 1550 nm is capable to record moderately wet snow surfaces, even tough it was not originally designed for snow. Since this TLS type is operating on a wavelength that is eye safe, it provides a wide range of application options to practitioners for avalanche warning and hydrological purposes.

Regarding transferability of the method to other alpine research areas it was found that RIEGL TLS operate an automated range correction to provide a distance independent relative reflectance. However, in our opinion a topographic correction should be done additionally for incidence angle normalization. Also, with larger distance to the target laser signal dropouts are increasing

More field campaigns need to be conducted to improve snow wetness analysis and to reduce potential influencing factors on the measurements. The topographic incidence angle correction of the reflectivity should be improved and additionally a correction for the pulse shape deviation could be added to the scanner's automatic range correction to increase the accuracy of the laser scan data. Furthermore, concurrent in situ snow temperature measurements and a thermal camera mounted and calibrated to the TLS could be used to get more information about the properties of the snowpack. Also, field grain structure analyses are an option to add. In addition, models (e.g. radiative transfer models) to quantify and correct the effects of grain size and radiation need to be set up to reduce uncertainty. Also, a comparison and validation with the ENVEO satellite (Sentinel 1) wet snow maps is a potential task for the future.

TLS snow surface reflectivity has large potential for the spatio-temporal analysis snow wetness, especially with the rapid technological development in LiDAR over the last few years. Continuing research effort in LiDAR instruments and improvement of the processing workflows are an important task for the future. The findings of this study are of significance for snow-hydrological issues, as to monitor alpine water resources, avalanche terrain, melt water run-off for flood forecasting, to validate snowpack dynamics of hydrological models and for hydropower management.

7 REFERENCES

Baggi, S. & Schweizer, J. (2009). Characteristics of wet-snow avalanche activity: 20 years of observations from a high alpine valley (Dischma, Switzerland). *Nat. Hazards*, *50*, 97–108.

Baltsavias, E. P. (1999). A comparison between photogrammetry and laser scanning. *ISPRS Journal of Photogrammetry and Remote Sensing, 54, 83-94.*

Besl, P. J., McKay, H. D. (1992). A method for registration of 3-D shapes. *IEEE Transactions on Pattern Analysis and Machine Intelligence,* 14(2), 239–256.

Bhardwaj, A., Sam, L., Bhardwaj, A., & Martín-Torres, F. J. (2016). LiDAR remote sensing of the cryosphere: Present applications and future prospects. *Remote Sensing of Environment, 177*, 125-143.

Birkeland, K. W., Hansen, K. J. & Brown, R. L. (1995). The spatial variability of snow resistance on potential avalanche slopes. *J. Glaciol.*, 41(137), 183–190.

Boyne, H. & Fisk, D. (1987). A comparison of snow cover liquid water measurement techniques *Water Resour. Res.*, *23*, 1833–1836.

Brandner, R. (1985). Geologische und Tektonische Übersichtskarte von Tirol. *Tirol-Atlas, C1, C3*. Innsbruck: Univ.-Verlag Wagner.

Briese, C., Chatzikyriakou, C. & Mandlburger, G. (2016). Orientation and Processing of Airborne Laser Scanning Data, Module RadioCal. Accessed on July 3, 2017 http://geo.tuwien.ac.at/opals/html/ModuleRadioCal.html.

Brun, E., Martin, E., Simon, V., Gendre, C. & Coleou, C. (1989). An energy and mass model of snow cover suitable for operational avalanche forecasting. Journal of Glaciology, 35 (121), 333-342.

Buchroithner, M. F. (1995). Problems of Mountain Hazard Mapping Using Spaceborne Remote Sensing Techniques. *Advances in Space Research,* 15 (11), 57–66.

Bühler, Y., Hüni, A., Christen, M., Meister, R. & Kellenberger, T. (2009). Automated Detection and Mapping of Avalanche Deposits Using Airborne Optical Remote Sensing Data. *Cold Regions Science and Technology,* 57 (2–3), 99–106.

Bühler, Y., Marty, M., Egli, L., Veitinger, J., Jonas, T., Thee, P., & Ginzler, C. (2015). Snow depth mapping in high-alpine catchments using digital photogrammetry. *The Cryosphere, 9*(1), 229-243.

Chen, Y. & Medioni, G. (1992). Object modelling by registration of multiple range images. Image and Vision Computing, 10(3), 145–155.

Colbeck, S. C. (1979). Grain clusters in wet snow. *J. Colloid Interface Sci.,* 72, 371–84

Conrad, O., Bechtel, B., Bock, M., Dietrich, H., Fischer, E., Gerlitz, L., Wehberg, J., Wichmann, V. & Boehner, J. (2015). System for Automated Geoscientific Analyses (SAGA) v. 2.1.4. Geosci. Model Dev., 8, 1991-2007.

Coren, F. & Sterzai, P. (2006). Radiometric correction in laser scanning. *International Journal of Remote Sensing*, 27(15), 3097-3104.

Deems, J. S., Fassnacht, S. R., & Elder, K. J. (2006). Fractal Distribution of Snow Depth from Lidar Data. *Journal of Hydrometeorology, 7*(2), 285-297.

Deems, J. S., Painter, T. H., & Finnegan, D. C. (2013). Lidar measurement of snow depth: a review. *Journal of Glaciology, 59*(215), 467-479.

Deems, J. S., Gadomski, P. J., Vellone, D., Evanczyk, R., Lewinter, A. L., Birkeland, K. W., & Finnegan, D. C. (2015). Mapping starting zone snow depth with a ground-based lidar to assist avalanche control and forecasting. *Cold Regions Science and Technology, 120*, 197-204.

Denoth, A. (1982). Effect of grain geometry on electrical properties of snow at frequencies up to 100 MHz, *J. Appl. Phys*., 53, 7496.

Denoth, A., Foglar, A., Weiland, P., Mätzler, C., Aebischer, H., Tiuri, M., & Sihvola, A. (1984). A comparative study of instruments for measuring the liquid water content of snow. *Journal of Applied Physics, 56*(7), 2154-2160.

Denoth, A. (1989). Snow dielectric measurements. *Advances in Space Research, 9*(1), 233-243.

Denoth, A. (1994). An electronic device for long-term snow wetness recording. *Annals of Glaciology, 19*, 104-106.

Doesken, J. N. & Judson, A. (1997). *A Guide to the Science, Climatology, and Measurement of Snow in the United States*. Fort Collins, USA: Colorado State University.

Dozier, J., & Painter, T. H. (2004). Multispectral And Hyperspectral Remote Sensing Of Alpine Snow Properties. *Annual Review of Earth and Planetary Sciences, 32*(1), 465-494.

Dozier, J., Green, R. O., Nolin, A. W., & Painter, T. H. (2009). Interpretation of snow properties from imaging spectrometry. *Remote Sensing of Environment, 113*.

Eckerstorfer, M., Bühler, Y., Frauenfelder R. & Malnes E. (2016). Remote Sensing of Snow Avalanches: Recent Advances, Potential, and Limitations. *Cold Regions Science and Technology*, 121, 126–140.

Egli, L., Jonas, T., Grünewald, T., Schirmer, M., & Burlando, P. (2011). Dynamics of snow ablation in a small Alpine catchment observed by repeated terrestrial laser scans. *Hydrological Processes, 26*(10), 1574-1585.

Einhorn, B., Eckert, N., Chaix, C., Ravanel, L., Deline, P., Gardent, M., Boudieres, V., Richard, D., Vengeon, J., Giraud, G. & Schoeneich, P. (2015). Climate Change and Natural Hazards in the Alps: Observed and potential impacts on physical and socio-economic systems. *Journal of Alpine Research*, 103, 2.

Eitel, J. U. H., Vierling, L. A. & Magneys, T. S. (2013). A light weight, low cost autonomously operating terrestrial laser scanner for quantifying and monitoring ecosystem structural dynamics. *Agricultural and forest meteorology*. 180, 86-96.

Eitel, J. U. H., Höfle, B., Vierling, L. A., Abellan, A., Asner, G. P., Deems, J. S., Glennie, C. L., Joerg, P. C., Lewinter, A. L., Magney, T. S., Mandlburger, G., Morton, D. C., Müller, J. & Vierling, K. T. (2016). Beyond 3-D: The new spectrum of lidar applications for earth and ecological sciences. - *Rem. sens. of Environm*. 186, 372-392.

Evans, S. (1965). Dielectric properties of ice and snow – A review. *Journal of Glaciology*, 5, 773.

Fey, C. & Wichmann, V. (2016). Long-range terrestrial laser scanning for geomorphical change detection in alpine terrain - handling uncertainties. *Earth Surface Processes and Landforms*, 42(5), 789–802.

Fierz, C. & Föhn, P. (1994). Long-term observation of the water content of an Alpine snowpack. In *Proceedings International Snow Science Workshop* (pp. 117-131). Snowbird, Utah.

Fierz, C., Armstrong, R.L., Durand, Y., Etchevers, P., Greene, E., McClung, D.M., Nishimura, K., Satyawali, P.K. & Sokratov, S.A. (2009). *The International Classification for Seasonal Snow on the Ground.* IHP-VII Technical Documents in Hydrology N°83, IACS Contribution N°1, UNESCO-IHP, Paris.

Foppa, N., Stoffel, A. & Meister, R. (2007). Synergy of in Situ and Space Borne Observation for Snow Depth Mapping in the Swiss Alps. *International Journal of Applied Earth Observation and Geoinformation,* 9(3), 294–310.

Fritzmann, P., Höfle, B., Vetter, M., Sailer, R., Stötter, J., & Bollmann, E. (2011). Surface classification based on multi-temporal airborne LiDAR intensity data in high mountain environments. A case study from Hintereisferner, Austria. *Zeitschrift für Geomorphologie, Supplementary Issues, 55*(2), 105-126.

Frolov, A. D. & Macheret, Y. Y. (1999). On dielectric properties of dry and wet snow. *Hydrological Processes*, 13, 1755-1760.

Gabbud, C., Micheletti, N. & Lane, S.N. (2015). Instruments and methods. LiDAR measurements of surface melt for a temperate alpine glacier at the seasonal ad hourly scales. *Journal of Glaciology*, 61, 963–974.

Geist, T., Lutz, E. & Stötter, J. (2003). Airborne laser scanning technology and its potentials for applications in glaciology. In H. G. Maas, G. Vosselman & A. Streilein (Eds.) *3-D Reconstruction from Airborne Laserscanner and INSAR Data*; ISPRSWorkshop: Dresden, Germany.

Graham, L. (2012). The LAS 1.4 specification. *Photogramm. Eng. Remote Sens.*, 78(2), 93–102.

Green, R. O., Dozier, J., Roberts, D., & Painter, T. (2002). Spectral snow-reflectance models for grain-size and liquid-water fraction in melting snow for the solar-reflected spectrum. *Annals of Glaciology, 34*(1), 71-73.

Grünewald, T., Schirmer, M., Mott, R., & Lehning, M. (2010). Spatial and temporal variability of snow depth and ablation rates in a small mountain catchment. *The Cryosphere, 4*(2), 215-225.

Hammer, W. (1923). *Geologische Spezialkarte der Republik Österreich 1:75.000, Blatt Nauders 5245.* Wien: Verl. Geol. B.-A.

Hallikainen, M. T. (1989). Microwave radiometry of snow. *Adv. Space Res.*, *9*, 267–275.

Hartzell, P. J., Gadomski, P. J., Glennie, C. L., Finnegan, D. C., & Deems, J. S. (2015). Rigorous error propagation for terrestrial laser scanning with application to snow volume uncertainty. *Journal of Glaciology, 61*(230), 1147-1158.

Hasted, J. B. (1973). *Aqueous Dielectrics*. London: Chapman and Hall.

Heilig, A., Schneebeli, M. & Eisen, O. (2009). Upward-looking ground-penetrating radar for monitoring snowpack stratigraphy. *Cold Reg. Sci. Technol.*, *59*, 152–162.

Helfricht, K., Schöber, J., Seiser, B., Fischer, A., Stötter, J., & Kuhn, M. (2012). Snow accumulation of a high alpine catchment derived from LiDAR measurements. *Advances in Geosciences, 32*, 31-39.

Hodgson, M. & Bresnahan, P. (2004). Accuracy of Airborne LIDAR-Derived Elevation: Empirical Assessment and Error Budget. *Photogrammetric Engineering & Remote Sensing*, 70, 331-339.

Höfle, B., & Pfeifer, N. (2007). Correction of laser scanning intensity data: Data and model-driven approaches. *ISPRS Journal of Photogrammetry and Remote Sensing, 62*(6), 415-433.

Isenburg, M. (2013). LASzip: lossless compression of Lidar data. *Photogramm. Eng. Remote Sens*., 79(2), 209–217.

IWHW Wien (2005). *Hydrologischer Atlas Österreichs, HAÖ*. Wien: Bundesministerium für Land- und Forstwirtschaft, Umwelt und Wasserwirtschaft.

Jelalian, A. V. (1992). Laser Radar Systems. Boston London: Artech House.

Kaasalainen, S., Kaasalainen, M., Mielonen, T., Suomalainen, J., Peltoniemi, J., & Näränen, J. (2006). Optical properties of snow in backscatter. *Journal of Glaciology, 52*(179), 574-584.

Kaasalainen, S., Jaakkola, A., Kaasalainen, M., Krooks, A. & Kukko A. (2011). Analysis of Incidence Angle and Distance Effects on Terrestrial Laser Scanning Intensity: Search for Correction Methods. *Remote Sens*., 3(10), 2207-2221.

Kashani, A. G., Olsen, M. J., Parrish, J. E. & Wilson, N. (2005). A review of LIDAR Radiometric Processing: From *Ad Hoc* Intensity Correction to Rigorous Radiometric Calibration. *Sensors*, 15, 28099-28128.

Kattelmann, R. (1987). Some measurements of water movement and storage in snow. Symposium at Davos Avalanche formation, movement and effects. In B. Salm & H. Gubler (Eds.) *IAHS Publications (International Association of Hydrological Sciences)* (Volume 162, pp. 245–254) Oxfordshire, UK: Wallingford.

Kattelmann, R. & Dozier, J. (1999). Observations of snowpack ripening in the Sierra Nevada, California, USA, *J. Glaciol*., 45, 409–416.

Kim, I., McArthur, B. & Korevaar, E. (2000). Comparison of laser beam propagation at 785nm and 1550nm in fog and haze for optical wireless communications. *SPIE Photonics East/Optical Wireless Communications III*, 4214, 26–37.

Koch, F., Prasch, M., Bach, H., Mauser, W., Appel, F. & Weber, M. (2011). How will hydroelectric power generation develop under climate change scenarios? A case study in the Upper Danube basin. Energies, 4, 1508–1541.

Koch, F., Prasch, M., Schmid, L., Schweizer, J. & Mauser, W. (2014). Measuring Snow Liquid Water Content with Low-Cost GPS Receivers. *Sensors*, 14, 20975-20999.

Lefsky, M.A., Cohen, W.B., Parker, G.G. & Harding, D.J. (2002). Lidar remote sensing for ecosystem studies. *BioScience*, 52(1), 19–30.

Lehning, M., Völksch, I., Gustafsson, D., Nguyen, T.A., Stähli, M. & Zappa, M. (2006). ALPINE3D: A Detailed Model of Mountain Surface Processes and Its Application to Snow Hydrology. *Hydrological Processes* 20 (10), 2111–2128.

Lichti, D. & Skaloud, J. (2010). Registration and calibration. In G. Vosselman & H. Maas (Eds.), Airborne and Terrestrial Laser Scanning (pp. 83-133). Dunbeath: Whittles Publishing.

Lindenbergh, R., Pfeifer, N. & Rabbani, T. (2005). Accuracy Analysis of the Leica HDS3000 and feasibility of tunnel deformation monitoring. In: Proceedings of the ISPRS Workshop, Laser scanning 2005, Vol. 36(3/W3), pp. 24–29. Enschede, The Netherlands.

López-Moreno, J.I., Revuelto, J. & Alonso-Gonzáles, E. (2017). Using very long-range Terrestrial Laser Scanning to Analyze the Temporal Consistency of the Snowpack Distribution in a High Mountain Environment. *J. Mt. Sci.*, 14, 823–842.

Louge, M., Foster, R., Jensen, N., & Patterson, R. (1998). A Portable Capacitance Snow Sounding Instrument, *Cold Reg. Sci. Technol*., 28, 73–81.

Luce, H., Tarboton D.G. & Cooley K.R. (1998). The influence of the spatial distribution of snow on basin-averaged snowmelt. *Hydrol. Process.*, 12(10–11), 1671–1683.

Lundberg, A. (1997). Laboratory calibration of TDR-probes for snow wetness measurements. *Cold Regions Science and Technology*, 25(3), 197-205.

Luzi, G., Noferini, L., Mecatti, D., Macaluso, G., Pieraccini, M., Atzeni, C. & Nagler, T. (2009). Using a Ground-Based SAR Interferometer and a Terrestrial Laser Scanner to Monitor a Snow-Covered Slope: Results From an Experimental Data Collection in Tyrol (Austria). *IEEE Transactions on Geoscience and Remote Sensing, 47*(2), 382-393.

Maetzler, C. & Wegmueller, U. (1987). Dielectric properties of fresh water ice at microwave frequencies. Z. Physik D. *Applied Physics*, 20, 1623.

Maetzler, C., Strozzi, T., Weise, T., Floricioiu, D.M. & Rott, H. (1997). Microwave snowpack studies made in the Austrian Alps during the SIR-C/X-SAR experiment. *Int. J. Remote Sens.*, *18*, 2505–2530.

Margreth, S. & Romang, H. (2010). Effectiveness of Mitigation Measures against Natural Hazards. *Cold Regions Science and Technology* 64(2), 199–207.

Marsh, P., and Woo, M.K. (1987). Soil heat flux, wetting front advance and ice layer growth in cold, dry snow covers. In *Snom Property Measurement Workshop.* Technical Memorandum No. 140, Snow and Ice Subcommittee, Associate Committee on Geotechnical Research, National Research Council of Canada, Ottawa, pp. 497-524.

Marshall, H., Conway, H., & Rasmussen, L. (1999). Snow densification during rain, *Cold Reg. Sci. Technol*., 30, 35–41.

Martinec, J., Seidel, K., Burkart, U., & Baumann, R. (1991). Areal modelling of snow water equivalent based on remote sensing techniques. In *XX General Assembly IUGG in Vienna 1991*, IAHS-IUFRO Symposium Snow, Hydrology and Forests in High Alpine Areas, pages 121-129. IAHS Publication No. 205.

Mitterer, C., Heilig, A., Schweizer, J. & Eisen, O. (2011). Upward-looking ground-penetrating radar for measuring wet-snow properties. *Cold Reg. Sci. Technol.*, *69*, 129–138.

Mitterer, C., Techel, F., Fierz, C., & Schweizer, J. (2013). An operational supporting tool for assessing wet-snow avalanche danger. In Proceedings *International Snow Science Workshop.* Grenoble-Chamonix Mont-Blanc.

Middleton, W. E. K. (1952). *Vision Through the Atmosphere*. Toronto: U. of Toronto Press.

Mott, R., Schirmer, M. & Lehning, M. (2011). Scaling properties of wind and snow depth distribution in an Alpine catchment. *J. Geophys. Res.,* 116(D6), D06106.

Nagler, T., & Rott, H. (2000). Retrieval of wet snow by means of multitemporal SAR data. *IEEE Transactions on Geoscience and Remote Sensing, 38*(2), 754-765.

Nagler, T., Rott, H., Ripper, E., Bippus, G., & Hetzenecker, M. (2016). Advancements for Snowmelt Monitoring by Means of Sentinel-1 SAR. *Remote Sensing, 8*(4), 348.

NWS Office of Climate, Water and Weather Services (2013). Snow Measurement Guidelines for National Weather Service Surface Observing Programs.

Nolin A. W, Dozier J. & Mertes L. A. K. (1993). Mapping alpine snow using a spectral mixture modeling technique. *Ann. Glaciol.,* 17, 121– 24.

Nolin, A. W. & Dozier, J. (2000). A Hyperspectral Method for Remotely Sensing the Grain Size of Snow. *Remote Sensing of Environment, 74*(2), 207-216.

O'Brien, H. & Munis, R. H. (1975). *Red and near- infrared spectral reflectance of snow. Research Rep. 332*, Hanover, NH: U.S. Army CRREL.

Okorn, R., Brunnhofer, G., Platzer, T., Heilig, A., Schmid, L., Mitterer, C., Schweizer, J. & Eisen, O. (2014). Upward-looking L-band FMCW radar for snow cover monitoring. *Cold Reg. Sci. Technol*., 103, 31-40.

Painter, T. H., Dozier, J., Roberts, D. A., Davis, R. E. & Green, R. O. (2003). Retrieval of subpixel snow-covered area and grain size from imaging spectrometer data. *Remote Sensing of Environment*, 85, 64-77.

Painter, T. H. & Dozier J. (2004). Measurements of the hemispherical–directional reflectance of snow at fine spectral and angular resolution. *J. Geophys. Res.*, 109(D18), D18115

Painter, T. H., Berisford, D. F., Boardman, J. W., Bormann, K. J., Deems, J. S., Gehrke, F., Winstral, A. (2016). The Airborne Snow Observatory: Fusion of scanning lidar, imaging spectrometer, and physically-based modeling for mapping snow water equivalent and snow albedo. *Remote Sensing of Environment, 184*, 139-152.

Perovich, D. K. (2007). Light reflection and transmission by a temperate snow cover. *Journal of Glaciology, 53*(181), 201-210.

Paffenholz J. (2012). Direct geo-referencing of 3D point clouds with 3D positioning sensors. Dissertation, Hannover University, Germany.

Pfeifer, N. & Briese, C. (2007). *Geometrical Aspects of Airborne Laser Scanning and Terrestrial Laser Scanning*. Rönnholm, P., Hyyppä, H., Hyypä, J., Eds.; International Archives Photogrammetry and Remote Sensing: Espoo, Finnland.

Pfenningbauer, M., & Ullrich, A. (2010) Improving quality of laser scanning data acquisition through calibrated amplitude and pulse deviation measurement. *Proc. SPIE* 7684-53.

Pfennningbauer, M., Clifford, W., & Ullrich, A. (2013). Enhancing onlinewaveform processing by adding new point attributes. *SPIE Baltimore*.

Pinzer, B. R. & Schneebeli, M. (2009). Snow metamorphism under alternating temperature gradients: Morphology and recrystallization in surface snow. *Geophysical Research Letters*, 36.

Pomeroy, J.W. & Brun, E. (2001). Physical properties of snow. In: H. G. Jones et al. (Eds.) *Snow Ecology* (pp. 45-126). Cambridge: Cambridge University Press.

Prantl, H., Nicholson, L., Sailer, R., Hanzer, F., Juen, I., & Rastner, P. (2017). Glacier Snowline Determination from Terrestrial Laser Scanning Intensity Data. *Geosciences, 7*(3), 60.

Prasch, M., Mauser, W. & Weber, M. (2013). Quantifying present and future glacier melt-water contribution to runoff in a Central Himalayan river basin. *Cryosphere*, *7*, 889–904.

Pratt, W. K. (1969). *Laser Communication Systems*. New York: J. Wiley & Sons.

Prokop, A., Schirmer, M., Rub, M., Lehning, M., & Stocker, M. (2008). A comparison of measurement methods: terrestrial laser scanning, tachymetry and snow probing for the determination of the spatial snow-depth distribution on slopes. *Annals of Glaciology, 49*(1), 210-216.

Prokop, A. (2008). Assessing the applicability of terrestrial laser scanning for spatial snow depth measurements. *Cold Regions Science and Technology, 54*(3), 155-163.

Purtscheller, F. (1978). *Ötztaler und Stubaier A*lpen. Sammlung geologischer Führer Nr. 53, 128pp. Stuttgart: Gebr. Bornträger.

Rees, W. G. (2006). *Remote Sensing of Snow and Ice*. United States of America: Taylor and Francis Group,

Raymond, C. E. & Tusima, K. (1979). Grain coarsening of water-saturated snow. *Glaciol.,*

22(86), 83-105.

Rieg, L., Wichmann, V., Rutzinger, M., Sailer, R., Geist, T. & Stötter. J. (2014). Data Infrastructure for Multitemporal Airborne Lidar Point Cloud Analysis – Examples from Physical Geography in High Mountain Environments. *Computers, Environment and Urban Systems,* 45, 137–146.

RIEGL Laser Measurement Systems GmbH (2014a). 3D Terrestrial Laser Scanner RIEGL VZ-4000 / RIEGL VZ-6000 General Description and Data Interfaces. Horn, Austria.

RIEGL Laser Measurement Systems GmbH (2014b). LAS extrabytes implementation in RIEGL Software. WHITEPAPER. Horn. Austria

RIEGL Laser Measurement Systems GmbH (2015). Data Sheet, Airborne Laser Scanning Software RiMTA ALS for Automated Resolution of Range Ambiguities. Horn, Austria.

RIEGL Laser Measurement Systems GmbH (2017a). Data Sheet, RIEGL VZ-4000. Horn, Austria.

RIEGL Laser Measurement Systems GmbH (2017b). Data Sheet, RIEGL VZ-6000. Horn, Austria.

Rondeau-Genesse, G., Trudel, M., & Leconte, R. (2016). Monitoring snow wetness in an Alpine Basin using combined C-band SAR and MODIS data. *Remote Sensing of Environment, 183*, 304-317.

Rott, H. & Davis, R.E(1993). Multifrequency and polarimetric sar observations on alpine glaciers. *Ann. Glaciol.*, *17*, 98–98.

Sailer, R., Bollmann, E., Hoinkes, S., Rieg, L., Sproß, M. & Stötter, J. (2012). Quantification of Geomorphodynamics in Glaciated and Recently Deglaciated Terrain Based on Airborne Laser Scanning Data. *Geografiska Annaler: Series A, Physical Geography,* 94, 17–32.

Schaer, P., Skaloud, J., Landtwing, S. & Legat, K. (2007). Accurancy estimation for laser point cloud including scanning geometry. *Int. Arch. Photogramm. Remote Sens.*, 36(5/W8).

Schaffhauser, A., Adams, M., Fromm, R., Jörg, P., Luzi, G., Noferini, L., & Sailer, R. (2008). Remote sensing based retrieval of snow cover properties. *Cold Regions Science and Technology, 54*(3), 164-175.

Schattan, P., Baroni, G., Oswald, S. E., Schöber J., Fey, C., Kormann, C., Huttenlau, M. & Achleitner, S. (2017). Continuous monitoring of snowpack dynamics in alpine terrain by aboveground neutron sensing. *Water Resources Research*, 53.

Schmid, L., Heilig, A., Mitterer, C., Schweizer, J., Maurer, H., Okorn, R. & Eisen, O., (2014). Continuous snowpack monitoring using upward-looking ground-penetrating radar technology*. J. Glaciol.,* 60, 509-525.

Schmidt, R. A. & Gluns, D. R. (1991). Snowfall interception on branches of three conifer species. *Can. J. For. Res.*, 21, 1262-1269.

Schoeber, J., Schneider, K., Helfricht, K., Schattan, P., Achleitner, S., Schöberl, F., & Kirnbauer, R. (2014). Snow cover characteristics in a glacierized catchment in the Tyrolean Alps - Improved spatially distributed modelling by usage of Lidar data. *Journal of Hydrology, 519*, 3492-3510.

SNICAR-Online, Flanner, M. G., Zender, C. S., Randerson, J. T. & Rasch P. J. (2007). Present day climate forcing and response from black carbon in snow, *J. Geophys. Res.*, 112, D11202.

Snow and Ice Data Center. "All About Snow." Accessed 16 May 2018. https://nsidc.org/cryosphere/snow.

Soudarissanane, S., Van Ree, J., Bucksch, A. & Lindenbergh, R., (2007). Error budget of terrestrial laser scanning: influence of the incidence angle on the scan quality. In: *Proceedings 3D-NordOst 2007*, Berlin, Germany.

Soudarissanane, S., Lindenbergh, R. & Gorte, B. (2008). Reducing the error in terrestrial laser scanning by optimizing the measurment set-up. In: *The International Archives of the Photgrammetry, Remote Sensing and Spatial Information Sciences*. Vol. 37. Part B5. Beijing.

Staehli, M., Stacheder, M., Gustafsson, D., Schlaeger, S., Schneebeli, M. & Brandelik, A. (2004). A new in situ sensor for large-scale snow-cover monitoring, *Ann. Glaciol*., 38(1), 273–278.

Stoffel, M. & Huggel, C. (2012). Effects of climate change on mass movements in mountain environments. *Progress in Physical Geography*, 36(3), 421-439.

Stuefer, S., Kane, D. L. & Liston, G. E. (2013). In situ snow water equivalent observations in the US Arctic, *Hydrol. Res*., 44(1), 21–34.

Techel, F. & Pielmeier, C. (2011). Point observations of liquid water content in wet snow – investigating methodical, spatial and temporal aspects. *The Cryosphere, 5*(2), 405-418.

Tedesco, M., Derksen, C., Deems, J. S., & Foster, J. L. (2014). Remote sensing of snow depth and snow water equivalent. *Remote Sensing of the Cryosphere,* 73-98.

Tiuri, M., Sihvola, A., Nyfors, E. & Hillikainen, M. (1984). The complex dielectric constant of snow at microwave frequencies. *IEEE Journal of Oceanic Engineering,* OE-9(5), 377-382.

Toon, O. B., C. P. McKay, T. P. Ackerman, & K. Santhanam (1989). Rapid calculation of radiative heating rates and photodissociation rates in inhomogeneous multiple scattering atmospheres, *J. Geophys. Res*., 94 (D13), 16, 287-16,301.

Ulaby, F.T., Moore, R.K., & Fung, A.K., (1981). Microwave remote sensing, Active and passive. *Volume II: Radar remote sensing and surface scattering and emission theory*. Norwood: Artech House Inc.

Van Genechten, B. (2008). 3D RiskMapping. Theory and Practice on Terrestrial Laser Scanning. Training material based on practical applications. *Universidad Polytecnica de Valencia Editorial.*

Vosselman, G., & Maas, H. (2010). *Airborne and Terrestrial Laser Scanning*. Dunbeath: Whittles Publishing.

J. M. Wallace & Hobbs, P. V. (1977). *Atmospheric Science: An Introductory Survey*. Orlando: Academic Press.

Warren, S. G., & Wiscombe, W. J. (1980). A Model for the Spectral Albedo of Snow. II: Snow Containing Atmospheric Aerosols. *Journal of the Atmospheric Sciences, 37*(12), 2734-2745.

Warren, S. G. (1982). Optical properties of snow. Reviews of Geophysics, 20(1).

Weber, M., Braun, L., Mauser, W. & Prasch, M. (2010) Contribution of rain, snow-and icemelt in the Upper Danube discharge today and in the future. *Geogr. Fis. Din. Quat.*, *33*, 221–230.

Wiscombe, W. J., & Warren, S. G. (1980). A Model for the Spectral Albedo of Snow. I: Pure Snow. *Journal of the Atmospheric Sciences, 37*(12), 2712-2733.

Wolfe, W., & Zissis, G. (1993). *The Infrared Handbook*. Prepared by the Infrared Information Analysis (IRIA) Center. New York: Environmental Research Institute of Michigan.

WSL-Institut für Schnee- und Lawinenforschung (Hrsg.) (2016). *SLF-Beobachterhandbuch*. Davos: WSL-Institut für Schnee- und Lawinenforschung SLF.

8 APPENDIX

APPENDIX A

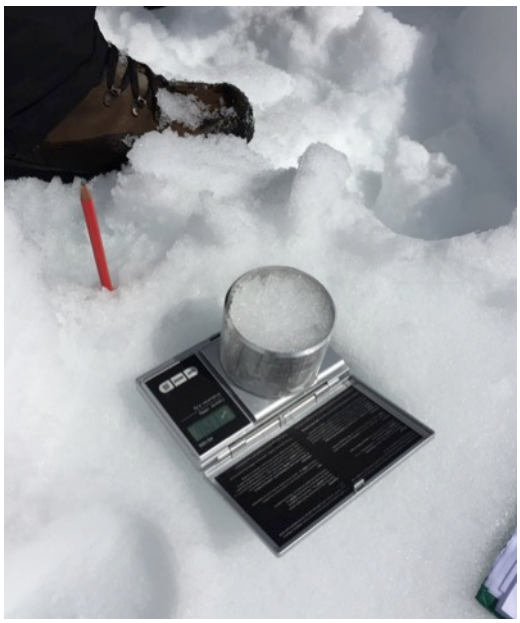

Fig. A. 1: In situ snow density measurement with a cyclinder and electrical scale (Personal photograph).

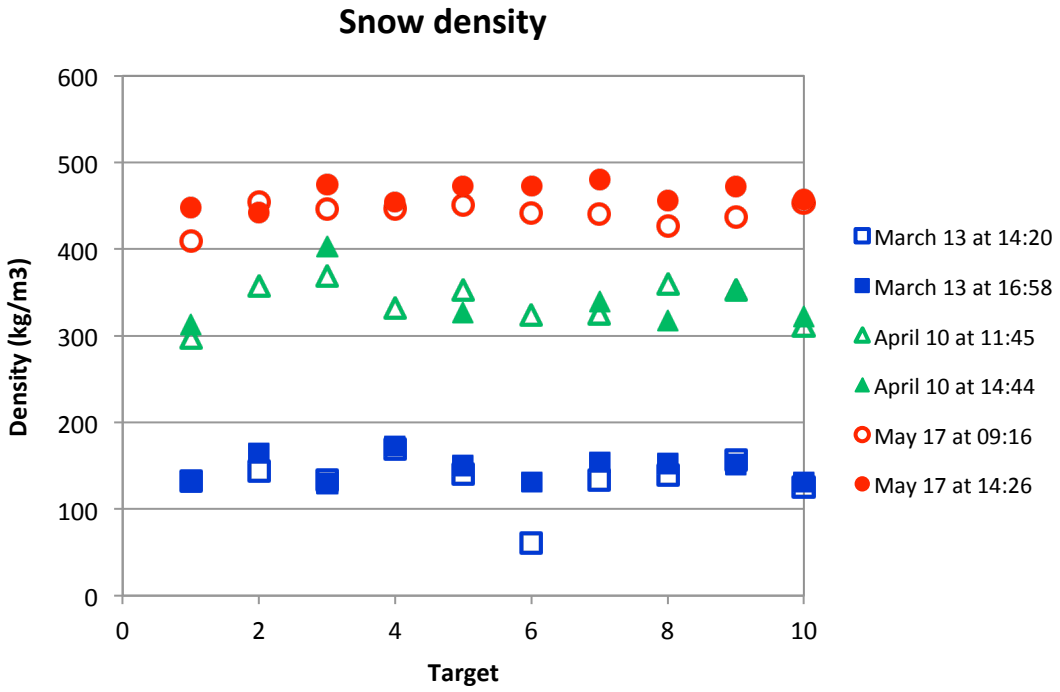

Fig. A. 2: In situ snow density results.

APPENDIX B

LWC maps with stretched classification

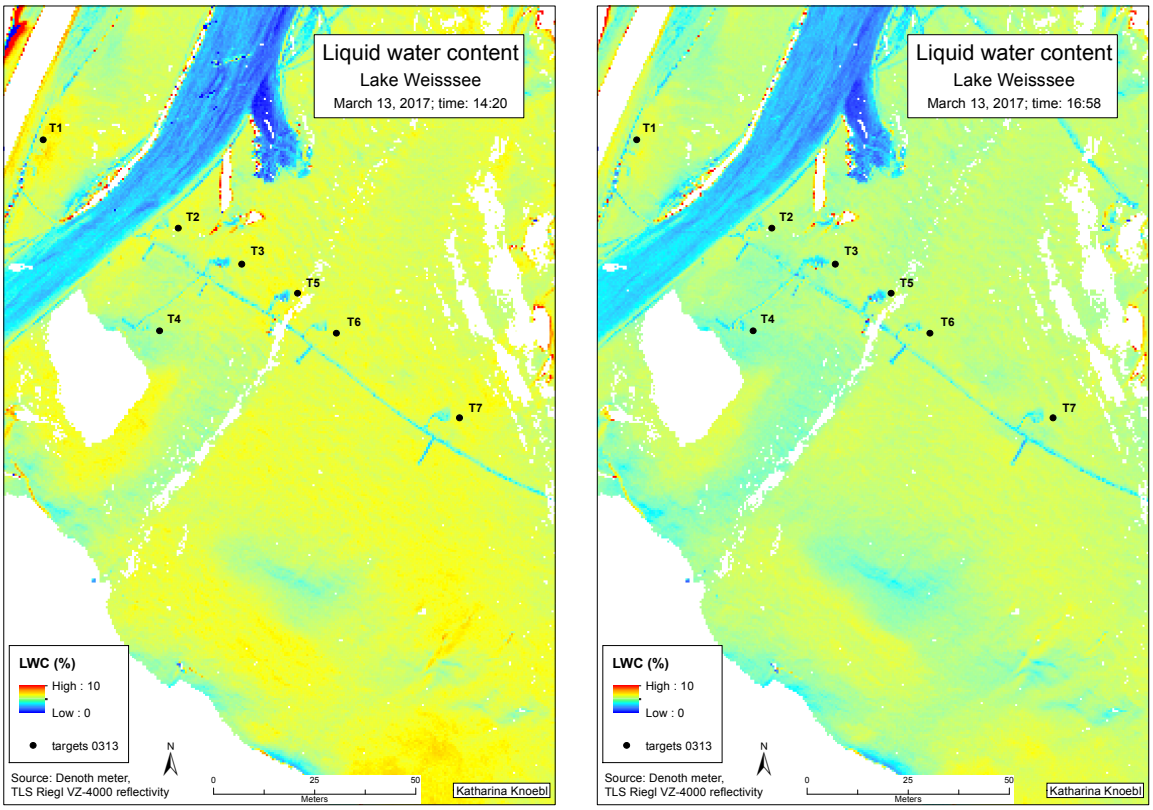

Fig. B. 1: Diurnal comparison of the liquid water content distribution at the snow surface at the research site Lake Weisssee on March 13, 2017. Data classified based on the linear regression of in situ LWC and TLS reflectivity and mapped with a stretched classification.

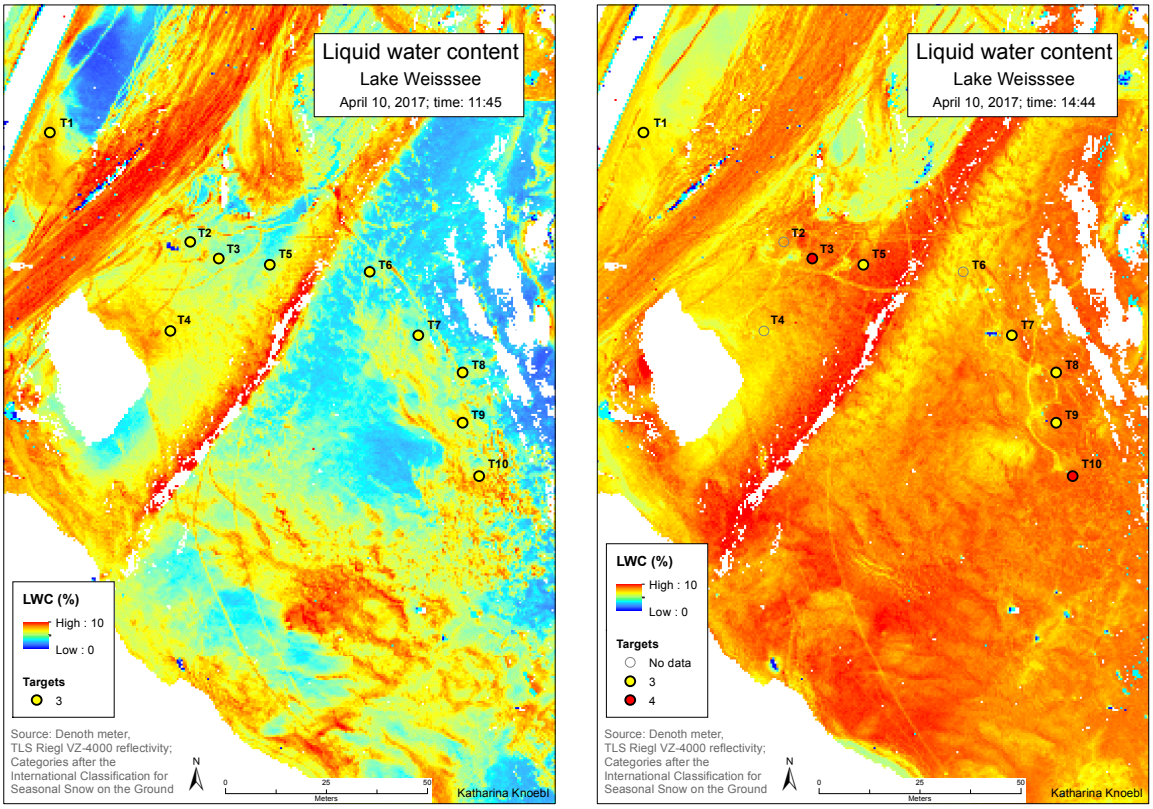

Fig. B. 2: Diurnal comparison of the liquid water content distribution at the snow surface at the research site Lake Weisssee on April 10, 2017. Data classified based on the linear regression of in situ LWC and TLS reflectivity and mapped with a stretched classification.

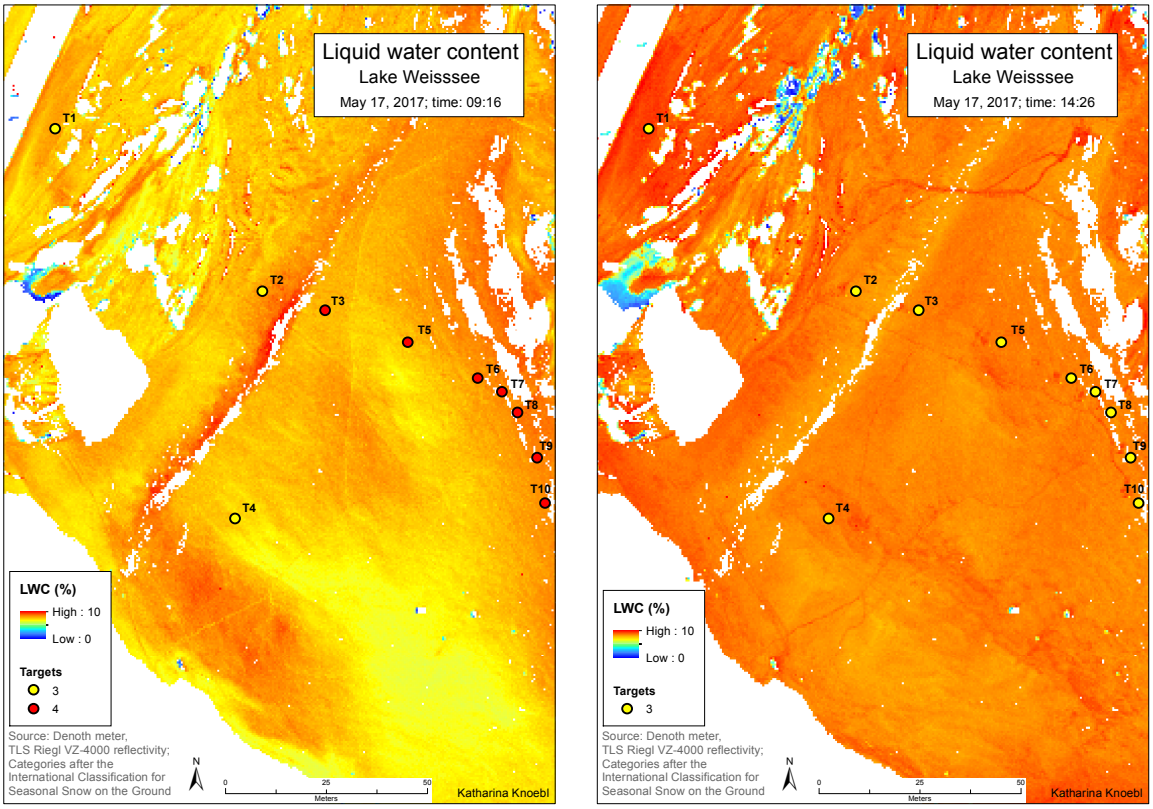

Fig. B. 3: Diurnal comparison of the liquid water content distribution at the snow surface at the research site Lake Weisssee on May 17, 2017. Data classified based on the linear regression of in situ LWC and TLS reflectivity and mapped with a stretched classification.

Fig. B. 4: Research area viewed from scan position 2 on March 13, 2017 (Personal photograph).